Mechanical Degradation of Membrane Electrode Assemblies in Proton Exchange Membrane Fuel Cells

by

Yinqi Shen

A thesis

presented to the University of Waterloo

in fulfillment of the

thesis requirement for the degree of

Doctor of Philosophy

in

Mechanical and Mechatronics Engineering

Waterloo, Ontario, Canada, 2017

Examining Committee Membership

The following served on the Examining Committee for this thesis. The decision of the Examining Committee is by majority vote.

External Examiner	NAME	Zhongsheng Liu
	Title	Principal Research officer
Supervisor(s)	NAME	Xianguo Li
	Title	Professor
Internal Member	NAME	Fue-Sang Lien
	Title	Professor
Internal Member	NAME	John Wen
	Title	Professor
Internal-external Member	NAME	Sheshakamal Jayaram
	Title	Professor

Author’s Declaration

I hereby declare that I am the sole author of this thesis. This is a true copy of the thesis, including any required final revisions, as accepted by my examiners.

I understand that my thesis may be made electronically available to the public.

Abstract

The Polymer Electrolyte Membrane (PEM) fuel cell is an ideal emerging alternative power source for transportation; however, before PEM fuel cells' widespread use, a number of technical challenges need to be overcome, including durability which is mainly associated with three factors: mechanical, electrochemical, and thermal degradation. Among them, mechanical degradation is of paramount importance because it causes a gradual reduction of mechanical strength, toughness and, ultimately, cell performance decay. Yet, studies focusing on the mechanical degradation of MEAs and its impact on cell performance decay are relatively scarce. This thesis focuses on the early and late stages of mechanical degradation of an MEA in a PEM fuel cell. In the experimental phase, scanning electron microscope (SEM) tests detailed the initial microstructures and their changes in an MEA before and after accelerated durability testing. The possibility that large stresses, including clamping forces and hygro-thermal stresses, were the reason behind these structural changes, necessitated further studies of stress conditions in the MEA using a structure model. Techniques used to characterize the mechanical properties of gas diffusion layers (GDLs) and of catalyst layers included a microcompression tester and the nanoindentation technique. These mechanical properties guided the selection of constitutive relations in the modelling. In the modelling phase, a structure model clarified the stress and deformation of MEAs during common and cyclic operating conditions. A variety of constitutive models enabled the simulation of different materials in cells. A deformed MEA determined from the structure model enabled a more realistic method to study the cell performance under early and late stages of mechanical degradation. Results revealed that MEA's early mechanical degradation, which is related with operating conditions, assembly methods and channel designs, had a complex effect on transport phenomenon. In addition, since an MEA's early degradation is associated with durability, the selection of operating conditions, assembly methods and channel designs should balance both cell performance and durability. Under 2000 cyclic changes in operating conditions, the cell performance decreases about 8% merely with the mechanical degradation. Therefore, in order to increase the life span of a PEM fuel cell, it is important to find an effective approach to relief the mechanical degradation.

Acknowledgements

I would like to thank my supervisor, Dr Xianguo Li, for his guidance in the production of this thesis. I would also like to thank Dr Zhongsheng Liu, Dr Sheshakamal Jayaram, Dr John Wen and Dr Fu-sang Lien and for taking the time to scrutinize my thesis. Their comments are highly appreciated. I would like to thank Amy Green, the best writing advisor in the world, for her invaluable guidance, steady encouragement, inspiration and support.

I would also like to thank some group members of Fuel Cell and Green energy Lab. I am particularly grateful for the assistance given by Ibrahim Alaefour, Yafei Chang, Samane Shahgaldi, and Jian Zhao.

My special thanks are extended to the most awesome office mates and friends, Shi Cheng, Sogol Roohparvarzadhe, Garrett Gauthier, Huangyan Jun and Jinyi Wang, not only for their tremendous help with this work, but also for their friendship.

Dedication

To my parents and brother, this humble work is a sign of my love to you!

Table of Contents

List of Figures

List of Tables

List of Abbreviations

AFC	Alkaline fuel cell
AMG	Algebraic multigrid
CCM	Catalyst-coated membrane
CFD	Computational fluid dynamics
DAQ	Data acquisition
DC	Direct current
DI	Deionized
DMFC	Direct methanol fuel cell
EOD	Electro-osmotic drag
FCATS	Fuel cell automated test station
FEM	Finite element method
FE-SEM	Field emission scanning electron microscope
GDL	Gas diffusion layer
HOR	Hydrogen oxidation reaction
MCFC	Molten carbonate fuel cell
IL-SEM	Identical location scanning electron microscope
MEA	Membrane electrode assembly
MPL	Micro-porous layer
ORR	Oxygen reduction reactions
PAFC	Phosphoric acid fuel cell
PEM	Proton exchange membrane
PEMFC	Proton exchange membrane fuel cell
PTFE	Polytetrafluoroethylene
SEM	Scanning electron microscope
SOFC	Solid oxide fuel cell
STA	Silicotungstic Acid
TEFLON	Tetrafluoroethylene

TEM	Transmission electron microscope
UDF	User defined function
VOF	Volume-of-fluid

List of Symbols

a	Water activity
A	Cell geometric area (m^2)
c	Concentration (kg m^{-3} or kmol m^{-3})
C_p	Specific heat capacity (J kg^{-1} K^{-1})
d	Diameter (m)
D	Mass diffusion coefficient (m^2s^{-1})
E	Young's modulus (MPa)
EW	Equivalent weight of membrane (kg $kmol^{-1}$)
F	Faraday's constant (96487 C mol^{-1})
F	Force (N)
f	Interfacial drag coefficient
G	Shear modulus
h	Latent heat (J kg^{-1}), heat transfer coefficient (W $m^{-2}K^{-1}$)
I	Current density (A cm^{-2})
J	Reaction rate (A m^{-3})
J	Total volumetric ratio
k	Thermal conductivity (W $m^{-1}K^{-1}$)
K	Permeability (m^2)
K	Body force component
m	Strain rate hardening parameter
$\dot{m}$	Mass flow rate (kg s^{-1})
M	Molecular weight (kg $kmol^{-1}$)
n_d	Electro-osmotic drag coefficient (H_2O per H^+)
P	Pressure (Pa)
$\dot{Q}$	Heat transfer rate (W)
r	Pore radius (m)
R	Universal gas constant (8.314 J $mol^{-1}K^{-1}$)

R	Resistance (Ω)
RH	Relative humidity
S	Volume fraction
S	Source terms, entropy (J $kmol^{-1}K^{-1}$)
s	Deviatoric stress
T	Temperature (K)
u	Displacement (m)
V	Electrical potential (V)
w	Plastic work (J)
W	Strain energy
Y	Mass fraction

Greek letters

α	Transfer coefficient
α	Thermal expansion coefficient
γ	Phase change rate (s^{-1})
γ	Strain component
ϵ	Porosity
ε	Error
ε	Strain component
δ	Thickness (m)
ζ	Water phase change rate (s^{-1})
ŋ	Overpotential (V)
θ	Contact angle
K	Electrical conductivity (S m^{-1})
λ	Water content in ionomer
λ	Scalar multiplier
λ	Stretch invariant
μ	Dynamic viscosity (kg m^{-1} s^{-1})
μ	Shear modulus

ξ	Stoichionmetry ratio
ρ	Density (kg m^{-3})
σ	Surface tension coefficient (N m^{-1})
σ	Stress component
ϕ	Electrical potential (V)
φ	Electrical potential (V)
$\emptyset$	Local volume fraction
ω	Volume fraction of ionomer in catalyst layer
τ	Stress component
ϑ	Poisson's ratio
β	Swelling expansion coefficient

Superscripts/subscripts

a	Anode
Act	Activation
b	Bottom
c	Capillary
c	Cathode
Eff	Effective
el	Elastic
Ele	Electronic
Eq	Equilibrium
EOD	Electro-osmotic drag
fl	Fluid phase
g	Gas phase
GDL	Gas diffusion layer
H_2	Hydrogen
i	The i^{th} components
j	The j^{th} components
ion	Ionic, ionomer

l	Liquid water
m	Mass
mem	Membrane
O_2	Oxygen
ohm	Ohmic
open	Open circuit
pl	Plastic
ref	Reference state
rev	Reversible
T	Thermal
S	Swelling
sat	Saturation/saturated
sl	Solid phase including the membrane electrolyte
sld	Solid phase excluding the membrane electrolyte
vp	Water vapour

Chapter 1

Introduction

1.1. Background

Transportation is a paramount component of economic developments. This factor is even more noticeable in society when economic opportunities have been increasingly correlated with the mobility of people, goods and information. Over the past decades, the growing global economy and the significant population growth have escalated the demand for motorized transportation. Statistics report that from years 2008 to 2015, vehicle sales in China underwent a significant escalation, from 9.39 to 24.6 million [1]. However, this phenomenon also brings some issues surrounding the use of crude oil to power automobiles, including, environmental impacts, energy securities, and risks of demand outstripping supply [2]. The elevated levels of carbon dioxide and other greenhouse gases in the atmosphere, along with the increased energy demands in various sectors, compel nations to find alternative solutions.

Various kinds of fuel cells have worked commercially as alternatives to the internal combustion engines, which dramatically relieves the dependence on crude oil [3]. General Motors produced the first fuel cell road vehicle, the Chevrolet Electrovan, in

1966. Equipped with a proton exchange membrane (PEM) fuel cell system, this two-seat road vehicle is very cost-prohibitive and only has a range of 120 miles and a maximum speed of 70 mph [4]. Only after several decades of development, PEM fuel cell powered vehicles established its commercial viability. Many automobile companies, such as General Motors, Toyota, Honda, Nissan and Ford, have invested significant amounts of money on fuel cell research and publicly committed to selling a fuel cell vehicle. Currently, fuel cell powered vehicles have obtained wide applications around the world. They have accumulated over 970,000 km of driving and 30%-141% higher fuel economy than diesel and natural gas vehicles [5].

Fuel cells, generally using hydrogen gas as a fuel, are environmentally friendly energy conversion devices, which bear similarities both to batteries, with which they share the electrochemical nature of the power generation process, and to engines, which can work continuously if supplied with a fuel of some sort [6,7]. The categorization of fuel cells depends on electrolytes, operating temperatures, and fuel types [8]. According to the kinds of electrolytes, fuel cells can be classified into various types, including Proton Exchange Membrane (also named Polymer Electrolyte Membrane, PEM) Fuel Cells, Direct Methanol Fuel Cells (DMFCs), Alkaline Fuel Cells (AFCs), Phosphoric Acid Fuel Cells (PAFCs), Molten Carbonate Fuel Cells (MCFCs) and Solid Oxide Fuel Cells (SOFCs) [9]. In addition, based on their optimal operating temperatures and fuel types, these fuel cells are suitable for various applications. For example, PAFCs, MCFCs, and SOFCs win wide applications for stationary power generation, while PEM fuel cells, DMFCs, and AFCs are suitable for vehicular or portable applications.

The PEM fuel cell is an ideal emerging alternative power source for transportation because of its low operating temperatures, solid electrolyte, zero/low emissions, and high power densities. PEM fuel cells operate at a low temperature (around $75^{o}C$ -$80^{o}C$), which enables a quick start-up time [10,11,12]. Since a cell converts chemical energy directly to electrical, it is not only more efficient and reliable than a traditional combustion engine, but also produces less noise. PEM fuel cells use a solid polymer membrane as the electrolyte, which is permeable to protons but insulated to electrons. This choice allows a simple, compact, and insensitive-to-orientation structure, which makes both the

manufacturing and the cell operation of a PEM fuel cell much easier than a fuel cell with a liquid electrolyte. In addition, a solid electrolyte brings benefits, such as less corrosion, low internal resistance, and high tolerance against large pressure differentials. Moreover, compared with internal combustion engines, research indicates that the use of PEM fuel cells in vehicles results in lower levels of emissions and energy consumption [13,14].

The past several decades have witnessed compelling improvements in terms of cell performance, material utilizations, and fuel supplies; however, before PEM fuel cells' widespread use, a number of technical challenges need to be overcome, including durability [15,16]. Durability is of particular importance since it determines the ultimate use of PEM fuel cells. Depending on various applications, the requirements for cell life span vary significantly. For instance, the current target for automotive applications is around 5000 to 20,000 hours, whereas for stationary applications the target is about 40,000 hours [17,18]. Unfortunately, at present most PEM fuel cell stacks available on the market and research institutes can only achieve 80% of these goals. PEM fuel cell durability is mainly associated with three factors: mechanical, chemical/electrochemical, and thermal degradation [19,20,21]. Among them, mechanical degradation is of paramount importance because it causes a gradual reduction of mechanical strength and toughness of Membrane Electrode Assemblies (MEAs), in turn causing microstructural changes in MEAs, such as cracks, delamination, and thickness variations, which eventually lead to cell performance decay [22,23,24,25]. However, studies focusing on the mechanical degradation of MEAs and its impacts on cell performance reduction are relatively scarce.

1.2. Fundamental Principles of Fuel Cells

A typical single PEM fuel cell assembly is made up of several components, as shown in Figure 1-1, including endplates, current collector plates, flow channel distribution plates (bipolar plates), gas diffusion layers (GDLs), catalyst layers and a membrane (solid electrolyte). Industries usually connect single cell assemblies in series to produce higher voltages, as illustrated in Figure 1-2. Figure 1-3 illustrates a cross-sectional schematic of the primary components in a PEM fuel cell. On the anode side, H_2 gas flows into the channels grooved into the bipolar plate. It then diffuses through the anode GDL into the

anode catalyst layer where it splits into protons and electrons. This half-cell reaction is called a hydrogen oxidation reaction (HOR).

$$\text{HOR:} \quad H_2 \rightarrow 2H^+ + 2e^-$$

The solid polymer membrane is permeable to protons but insulated to electrons. Therefore, the protons pass through the membrane and travel into the cathode side, while the electrons are forced to travel through an external circuit to the cathode side. Similar to the anode side, atmospheric air or pure oxygen flows into the cell and diffuses into the cathode catalyst layer through the cathode GDL and the bipolar plate. It reacts with the protons and electrons from the membrane and the external circuit, respectively, generating water and heat. Because of the low operating temperature, oxygen is reduced into liquid water in this reaction; therefore, it is called an oxygen reduction reaction (ORR).

$$\text{ORR:} \quad \frac{1}{2}O_2 + 2H^+ + 2e^- \rightarrow H_2O$$

The irreversibilities in converting chemical energy into electrical energy produce waste heat. The overall reaction is, therefore,

$$H_2 + \frac{1}{2}O_2 \rightarrow H_2O + Waste\ Heat + Electrical\ Energy$$

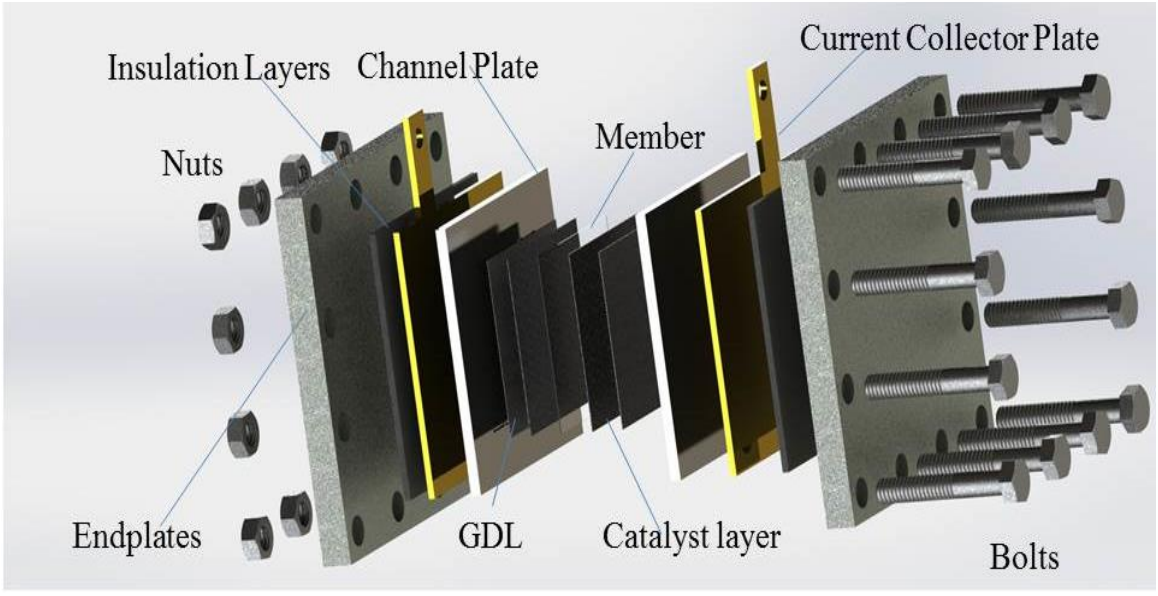

Figure 1-1 A schematic drawing of a single PEM fuel cell

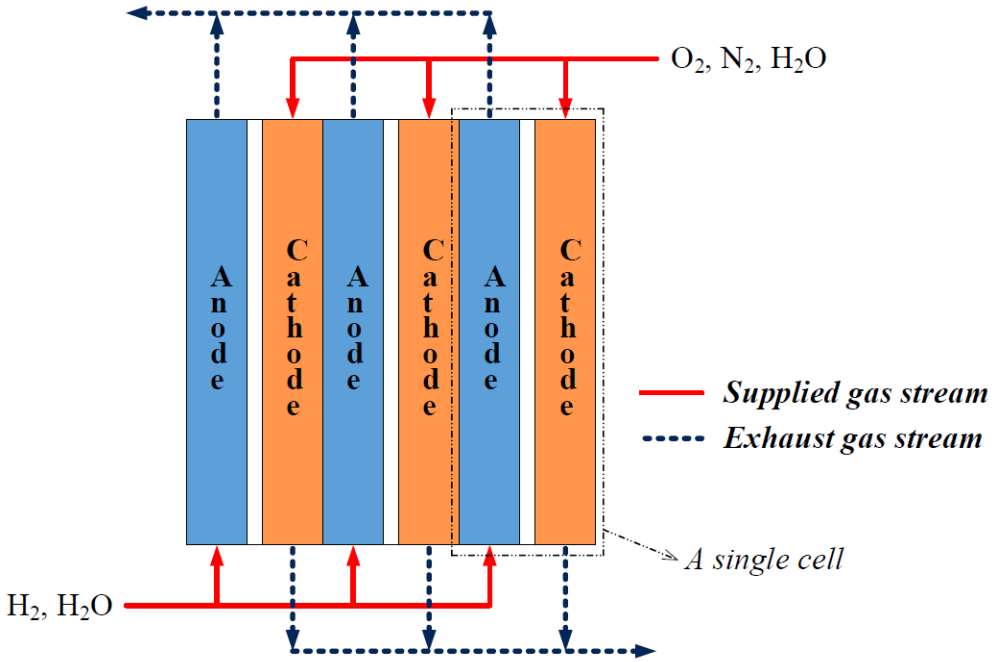

Figure 1-2 A schematic picture of a PEM fuel cell stack with three single cells [26]

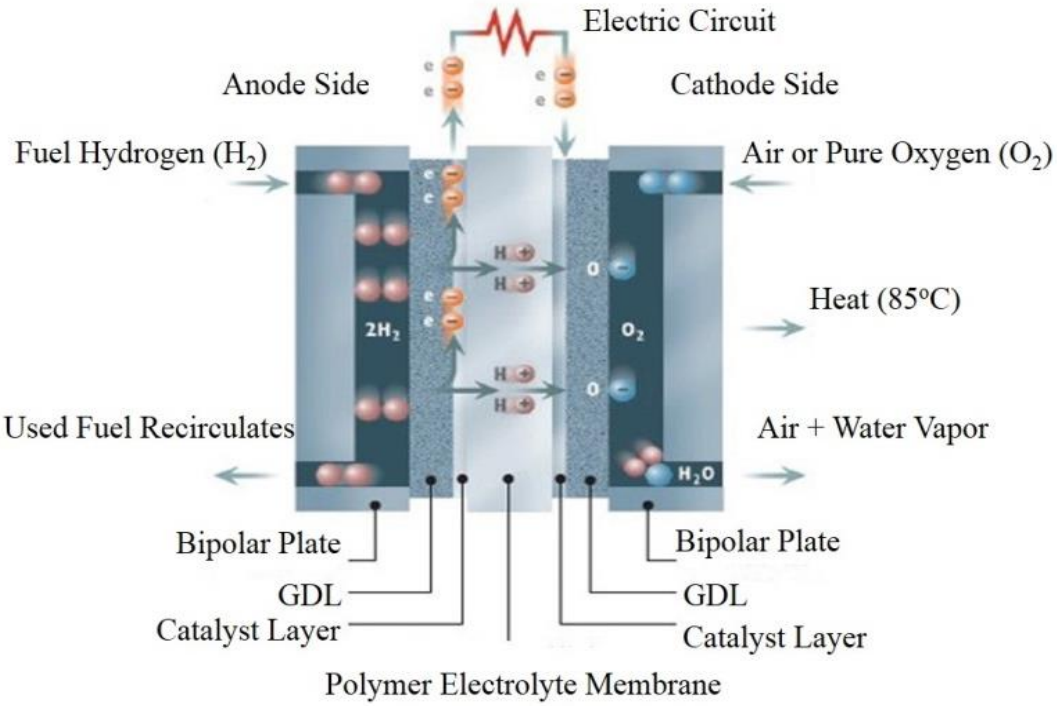

Figure 1-3 PEM fuel cell operating principle [27]

1.3. Main Components of PEM Fuel Cells

A PEM fuel cell obtains its signature name because of the electrolyte it uses. This electrolyte rests between the GDLs and catalyst layers from the anode and cathode sides. The whole piece is just a few hundred microns in thickness, which is called membrane electrode assemblies (MEAs). MEAs have to be sufficiently durable to withstand mechanical stresses during assembly processes and regular or randomly changing operating conditions [28,29]. During the cell operations, the MEA undertakes several functions, namely providing a place for the electrochemical reaction, offering an ionic conductive path, serving as an electronic insulator, and acting as a gas barrier to prevent the mixing of anode and cathode gases.

There are mainly two kinds of MEAs: GDL-based MEAs and CCM (catalyst-coated membrane)-based MEAs [30,31]. In a GDL-based MEA, a gas diffusion layer has catalysts coated on its surface, whereas the catalyst is directly applied onto the Nafion membrane in CCM-based MEAs. Compared to a GDL-based MEA, a CCM-based MEA provides a significantly higher performance in terms of lower contact resistances between the catalyst layers and the Nafion membrane, and lower catalyst loadings without sacrificing the performance; hence it is the choice of industries [32]. The material of different components of an MEA and their degradations during the cell operations affect the overall cell performance [33,34,35].

1.3.1. Membrane Electrolyte

In a typical PEM fuel cell, a membrane (the electrolyte) rests between two catalyst layers to block electrons and reactant gases (hydrogen and oxygen), while at the same time allowing ionic currents to pass with low resistance from the anode to cathode electrodes. Therefore, the requirements for a qualified membrane are good protonic conductivity, high flow reactant gas permeability, and strong mechanical and chemical stability.

Currently, the Nafion membrane produced by Dupont is the most widely used material for PEM fuel cells. It is a very thin material, ranging from 20 μm to 200 μm. Generally speaking, a thicker Nafion membrane offers better insulation and physical stability with higher proton transport resistance. On the other hand, a thinner membrane has low

insulation and stability but a higher proton transport ability [36,37]. The Nafion membrane is one kind of ionomer (synthetic polymers with ionic properties). It contains perfluorovinyl ethers terminated by sulfonic acids with hydrophobic tetrafluoroethylene (Teflon) backbones [38,39].

The proton conductivity of a Nafion membrane is directly associated with the membrane's hydration level because membranes rely on absorbed water to ionize their acid groups and to permit proton transport; thus, a suitable humidification of a Nafion membrane is essential [40,41,42]. For example, excess water content can lead to the flooding of the cathode side, whereas low water content dries out the membrane of the other side. Consequently, water management is crucial for PEM fuel cell operations.

1.3.2. Gas Diffusion Layer (GDL)

A GDL, a highly porous feature, promotes transitions due to its location between the bipolar plates and the catalyst layers. It offers a pathway for the mass transfer of reactants and products to and from the catalyst layers, ensures a structural stiffness in the MEA, promotes gas access to the catalysts under the landings between the flow fields, and serves as an electrically and thermally conductive pathway between the catalyst layer and the bipolar plate.

Some researchers believe that creating a through-plane porosity gradient is the main task of GDLs [43,44,45]. On one hand, the catalyst layers contain extremely small pores so that the number of reaction sites can be maximized. However, this structure indicates that the catalyst layers require enormous pressure gradients, making PEM fuel cells uneconomical to operate. On the other hand, the bipolar plates aid to distribute reacting gases efficiently over the electrode area with a minimal pressure drop to the catalyst layer. The GDLs neutralize this pressure difference [46,47,48].

There are two main types of GDLs: a raw GDL and a GDL with a hydrophobic binder (PTFE), as shown in Figure 1-4. All GDLs consist of graphitized carbon fibres. These carbon fibres held together in a random manner by a carbon binder, which resembles paper or cloth. A carbonized thermoset resin works as the binder. The GDL with PTFE coating typically has a dual-layer carbon-based porous structure, and includes a carbon

micro-porous layer (MPL) or a sub-layer consisting of carbon black particles and a hydrophobic agent. The sub-layer prevents the rough carbon fibre paper from puncturing the membrane. The application of the hydrophobic binder in the carbon fibre paper improves water management [49,50,51]. The GDLs' thickness (normally between 100 μm to 300 μm) and porosity vary significantly for different applications and operating conditions. For instance, a high-porosity GDL is suitable for PEM fuel cells operating at high current densities, since more water is produced [52]. This high porosity helps to transfer reactants and products to and from the catalyst layer. In contrast, a lower porosity is suitable for low current density fuel cells so that the membrane can keep a certain level of water content.

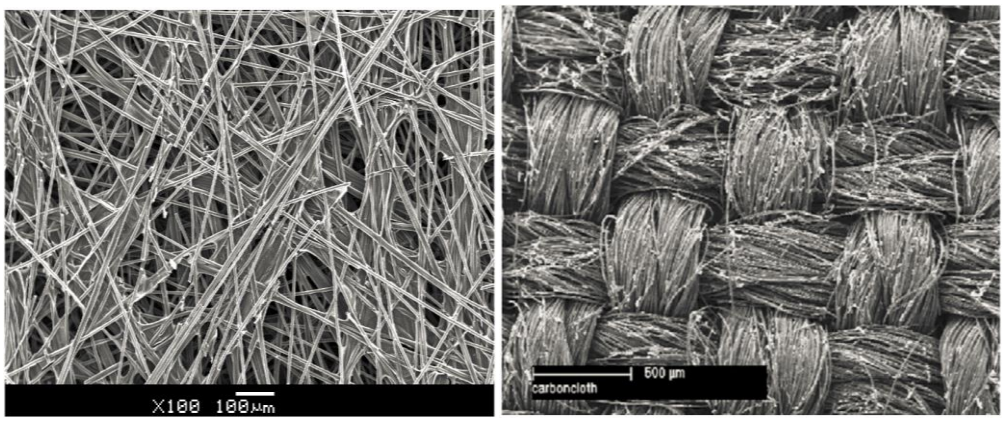

Figure 1-4 SEM images of various GDLs at 100* magnification [53]

1.3.3. Catalyst Layer

Catalyst layers aim to significantly facilitate electrochemical reactions because PEM fuel cells work at a low temperature. A catalyst layer is a porous material, and mainly consists of void regions, platinum, carbon particles and ionomers. Meanwhile, Pt-transition metal alloys, such as PtCo, Pt-Cr-Ni, and Pt-Ru-Ir-Sn, have also worked as catalysts in PEM fuel cells in order to reduce the cost [54,55]. The void regions provide spaces for the gaseous reactant. The carbon particles are electrically and thermally conductive, whereas the ionomer is proton conducting. In comparison to a Nafion membrane, which only starts to dissolve when in water at 210^{o}C and at a high pressure of 68 atm for more than two hours, the ionomer in the catalyst layer is in a more soluble state. It acts as a binder between the platinum/carbon particles, and offers a proton conductive path from the

membrane to the catalyst for a protonic current flow. The platinum loadings and carbon types have large implications for both cell performance and durability [56,57]. The carbon supported platinum powders must have a close contact with the ionomer of the membrane. The fact that the electrochemical reactions occur only at the three-phase contact interface necessitates a contact among reactant gases, catalysts, and ionomers, which also indicates that the catalyst microstructure and ionomer-catalyst interface significantly affect cell performance. Therefore, an optimized balance between these three phases enables an improvement in the electrochemical reaction rate [58,59,60,61].

1.4. Fuel Cell Performance

Figure 1-5 illustrates a typical graph of a PEM fuel cell performance, the so-called polarization curve, which shows the voltage outputs, *V*, versus the drawn current density, *i*. A current density, where the current is normalized by the area of the PEM fuel cells (a standard unit of current density, A cm^{-2}), is usually used in comparing the performance of PEM fuel cells with various stack sizes. The operating voltage of PEM fuel cells at different current densities can be determined through the following equation.

$$V_{cell} = V_{open} - \eta_{act} - \eta_{\mathrm{ohm}} - \eta_{conc}$$

In theory, if supplied with sufficient fuel, a PEM fuel cell can supply a certain amount of current, meanwhile maintaining a constant voltage determined by thermodynamics. However, the actual voltage output is always less than the thermodynamically determined value, due to some irreversible losses. Moreover, as shown in Figure 1-5, the greater the current, the lower the voltage output of the fuel cell, limiting the total power that can be delivered.

The polarization curve is made up of three parts--activation, ohmic and concentration polarizations--respectively resulting from the resistance to electrochemical reactions, the transport of electrons and ions in the cell components, and the limitations in the mass transfer [62].

The activation polarization represents the initial sharp drop of the cell voltage, which mainly results from the slowness of the reactions in the catalyst layers. It is primarily a

function of temperature, pressure, concentration and electrode properties, and dominates the low current density portion of the polarization curve. Transferring the electrons and protons to or from the electrode requires a certain proportion of voltage. However, electrons and protons have to accumulate to certain levels so that the reaction can take place continuously with sufficient gas supplies. Thus, a proportion of the voltage generated is inevitably lost, and is called the activation loss.

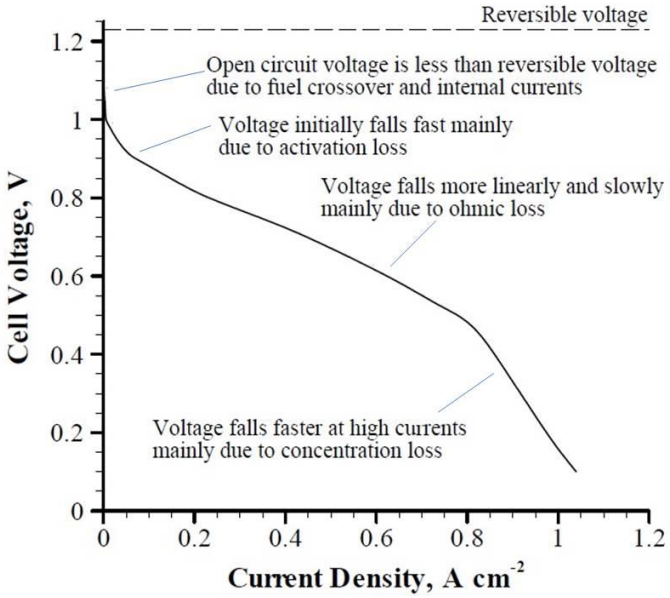

Figure 1-5 A typical polarization curve of a single PEM fuel cell

The ohmic polarization is expressed through Ohm's Law. It dominates the linear portion of the *I-V* curve. Improving the ionic and electronic conductivity of the cell enables the reduction of the resistance, *R*, in turn, reducing ohmic losses.

The concentration polarization, apparent at a very high current density, is associated with several factors, including the concentration changes and flow rate of the reactants in the catalyst layer along the flow channel from the inlet to the outlet, the cell temperature, and the structure of GDLs and catalyst layers. The concentration impacts voltage in terms of changes in the reactant's differential pressures, which is why this type of irreversibility is called concentration loss.

Another notable irreversible loss is the fuel crossover and internal current. Although a Nafion membrane acts as a barrier to electrons, small amounts of electrons and reactants

still pass through the Nafion membrane, which can reduce the open circuit voltage of PEM fuel cells. This type of loss becomes negligible when a meaningful amount of current is drawn from the cell.

1.5. Fuel Cell Degradation

1.5.1. Definition

The major technical challenge for fuel cells' commercialization as an alternative power source is the durability under various assembly methods, degradation of materials, operating conditions and impurities or contaminants. Although performance degradation is inevitable, the degradation rate could be minimized through a comprehensive understanding of degradation and failure mechanisms. The performance degradation has two aspects: the early stage degradation and the late stage degradation. The early stage degradation is associated with the assembly method and operating conditions. An appropriate assembly method ensures a reasonable interfacial conductivity between various cell components and prevents leaking. However, this assembly procedure also introduces deformation into the MEA. In addition, operating conditions result in expansions or shrinkages in catalyst layers and Nafion membranes, further intensifying MEAs' deformation. This deformation affects the effective transport properties, in turn, causing cell performance decay. On the other hand, the late stage degradation caused by the operating conditions of dynamic load cycling, start-up/shut-down procedure, and freeze/thaw make the cell performance reduction more appreciable.

1.5.2. Clarification

Fuel cell degradation is mainly associated with three categories: electrochemical degradation, thermal degradation and mechanical degradation. Previous studies paid significant attention to the electrochemical degradation. This degradation affects catalyst layers and Nafion membranes through gradual corrosions. Studies show that highly exothermal combustion between H_2 and O_2 can possibly cause pinholes in the membrane, bringing catastrophic issues [63,64]. In addition, peroxide (HO) and hydroperoxide (HOO) radicals, generated in the anode and cathode catalysts, can chemically attack the membrane and catalysts. This chemical attack is accelerated when the fuel cell is

operated under open circuit voltage and low humidity conditions. Moreover, foreign cationic ions significantly decrease cell performance in terms of adsorbing on the membrane and catalysts [65].

Some studies have addressed the issue of thermal degradation of membranes. PEM fuel cells normally operate at a temperature around 75^{o}C to enhance electrochemical kinetics, simplify water management and improve system CO tolerance. However, membrane protonic conductivity drops significantly with the decrease in water content when the cell is working at high temperatures [66]. Moreover, membranes are subject to critical breakdown at high temperatures due to the glass transition temperatures of polymers at around 80^{o}C [67]. Therefore, the thermal stability of membranes under rapid start-up, stable performance and easy operation in subfreezing temperatures are paramount important capabilities for fuel cell commercialization [68].

Mechanical degradation is of paramount importance because it causes a gradual reduction of mechanical strength and toughness of Membrane Electrode Assemblies (MEAs), in turn causing microstructural changes in MEAs, such as cracks, delamination, and thickness variations, which eventually lead to cell performance decay [22,23,24,25]. However, currently there is few studies focusing on this filed.

1.5.3. Practical Requirement

Depending on various applications, the requirements for cell life span vary significantly. For instance, the current target for automotive applications is lower than that for stationary applications, which is about 40,000 hours [17,18]. However, at present most PEM fuel cell stacks available on the market and research institutes can only achieve 80% of these goals. Practical degradation targets require less than 10% loss in the efficiency of the fuel cell system at the end of application, and a degradation rate of 2-10 μVh^{-1} is commonly accepted for most applications [20].

1.6. Objective and Scope of the Thesis

Mechanical degradation and thermal degradation are significant important in the study of PEM fuel cell durability. However, so far only limited research concentrates on this

region. Therefore, this thesis focused on the mechanical degradation of an MEA in a PEM fuel cell. The main objectives are the following:

- To develop constitutive relation (stress-strain model) for each component in an MEA
    - measure mechanical properties (stress-strain relation)
    - develop constitutive relation
    - validation experiments
- To develop a structure model for an entire fuel cell
- To incorporate the cell structure model with the cell performance model, and study the effect of mechanical degradation on performance

In order to achieve these objectives, in the experimental phase, a scanning electron microscope detailed and quantified the original microstructures of MEAs and their changes before and after cell degradation. Furthermore, various experimental tests provided a set of identified mechanical properties of MEAs and their changes with various cell operating conditions. These mechanical properties guided the selection of appropriate constitutive relations for different components in a PEM fuel cell structure model. In the modelling phase, this comprehensive structure model provided the stress and deformation conditions in MEAs, which involved all the major components of a PEM fuel cell, including GDLs, catalyst layers, Nafion membranes, and graphite flow channel plates. This model then quantified the deformations of a PEM fuel cell during regular and cyclic cell operations. Later, this deformed fuel cell structure supplied the physical problem for the cell performance modelling. This structure-performance coupled model, the last stage of modelling phase, enabled the study in the effects of early stage deformation and late stage deformation on cell performance.

This thesis has 9 chapters. Chapter 2 reviews the relevant literature regarding the mechanical degradation of a PEM fuel cell. Chapter 3 describes different experimental approaches used in the thesis. Chapter 4 explains the PEM fuel cell structure model and the cell performance model. Chapter 5 discusses the original and deformed microstructures of an MEA before and after cell degradation. Chapter 6 provides the mechanical characterization of various components in an MEA. Chapter 7 and 8 discuss

the numerical results for PEM fuel cells' mechanical and thermal degradation and cell performance. Chapter 9 summarizes the whole study and suggests some future work.

Chapter 2

Literature Review

Durability is of particular importance since it determines the ultimate use of PEM fuel cells. The past several decades have witnessed many numerical and experimental studies on PEM fuel cells' chemical performance decay and duration. The field has seen prominent achievements. However, studies focusing on the mechanical degradation of MEAs in PEM fuel cells and its impact on cell performance decay are relatively scarce. This scarcity is surprising because the knowledge of mechanical and degradation is one of the prerequisite steps of understanding cell performance reduction. Studies of cell mechanical degradation can be carried out from two perspectives: experiments and modelling. This chapter reviews and summarizes previous efforts and achievements in the study of mechanical degradation, generally classified according to each cell component of an MEA

2.1. Experimental Study

2.1.1. Visualization (Qualitative) Study

Recently, researchers have paid considerable attention to the relationship between microstructure changes and cell degradation. This research depended on an electron microscope, such as a scanning electron microscope (SEM) and a transmission electron microscope (TEM), to probe the original morphology and its changes in GDLs, catalyst layers and membranes. Regardless of the type of electron microscope tests, sample preparation remains a crucial step because inappropriate methods can ruin the original structures. Broka *et al*. used two different methods, the freeze-fracturing method and the glass-knife-cutting method, to prepare SEM samples [69]. They found that sample preparation methods can affect the Nafion structure's appearance. Compared with that of a sample prepared by the freeze-fracturing method, the impregnated Nafion layer was clearer in the sample prepared by the glass-knife cutting method. Currently, both methods win wide recognition in fuel cell SEM sample preparations; however, some researchers believe that the freeze-fracturing method has minimal impacts on the tested surface [13].

On the other hand, in order to obtain higher resolutions, the study of microstructural changes of MEAs after cell degradation also involves a TEM test. Similar to a SEM test, the sample preparation in a TEM test is critical because it manages to maintain the spatial relationship among the various macro- and micro-components. Because an MEA has a complex structure and a number of components, traditional preparation approaches are ill-suited for a TEM test. In order to resolve this issue, Blom *et al*. proposed a new samples preparation method [70]. First, they embedded a small piece from an MEA into an epoxy resin to support a porous material. Then a Reichert OMU3 Ultramicrotome helped to microtome the samples at room temperature. This method can successfully produce cross sections of an entire MEA.

MEA

Initially, research has mainly focused on the observations of structure defects on new MEAs and their associations with cell performance. Kundu *et al*. selected the freeze-fracturing method for sample preparations and observed six major defects under SEM

tests on new CCMs, including cracks, orientation, delamination, electrolyte clusters, platinum clusters and thickness variations [22]. Unlike Kundu, Barron *et al*. concentrated on the microstructures of cross sections [30]. They carried out a SEM observation on the cross section of a new CCM-based MEA. This cross section exhibited a uniform layer of catalysts, and a close connection between catalyst layers and an electrolyte membrane, which enables the reduction of mass and proton transfer resistance, and the increase in the catalyst utilization.

All the above studies involve only the original structure of MEAs. However, some researchers believe that the original microstructure changes during cell operations. These structural changes can, eventually, affect cell performance. Recently, other investigations have involved microstructural changes in MEAs after operations and their relationship with cell operating conditions and performance. In order to differentiate it from new MEAs, MEAs after operation are called used MEAs.

Silva *et al*. ran durability testing on an eight-cell stack. A SEM test detailed the morphological changes when the cell performance reduced to 66% [71]. They concluded that structural changes, such as porosity loss, platinum aggregation, delamination, cracking, and GDL debris, were the reasons behind performance reduction. The cathode side of all cells experienced a thinning process, which was more pronounced when the cells were located away from the hydrogen inlet in the stack. The highest level of reduction was about 47%.

Chemical additives, such as PTFE and Silicotungstic Acid (STA), in an MEA can affect its microstructure. In order to promote cell performance and relieve water flooding, additives receive wide applications in MEAs, which can affect the microstructures. Park *et al*. ran durability testing using an accelerated stress test (a wet/dry gas cycling method) [72]. The membrane was coated either with a treated PTFE or an untreated PTFE. A treated PTFE means that the PTFE layer was treated chemically to improve its hydrophilicity before incorporating it into the membrane. This chemical modification can enhance the compatibility and bonding between the Nafion resin and the PTFE matrix. The microstructure of a membrane cross section underwent investigations after cell failure using a SEM test. A highly porous structure with evenly distributed nodes and

pores existed on an untreated PTFE, whereas an uneven and roughened surface with an increased porosity and surface area prevailed in a treated PTFE. Around the break point after the tensile test, a PTFE coated membrane had a much denser thread-like structure. On the other hand, an untreated PTFE coated membrane had more micro-voids in the structure. Additionally, after 1800 wet/dry cycles, many pinholes occurred in the untreated PTFE coated membrane, which resulted from the separation between the Nafion polymer and the PTFE matrix.

Membrane

Tian *et al*. tested the feasibility of another additive, a Nafion/Silicotungstic Acid (STA) composite membrane [73]. From the SEM micrographs, the cast Nafion without a STA had no agglomerations; whereas a STA introduced agglomerations with a diameter around 0.1-0.2 microns into the membrane. These agglomerations were uniformly distributed within the cast Nafion. Also, many holes appeared when the composite Nafion/STA was immersed in boiling de-ionized water or in boiling 1M H_2SO_4, which can be attributed to the loss of STA particles.

The material of the channel plate can also impact the microstructure of MEAs. Schneider *et al* investigated the effect of a silicon channel plate on a Nafion membrane [74]. The results showed that the microstructure and chemical composition of the bulk Nafion were different from those of the Nafion in contact with the silicon. This phenomenon indicated that a micro-structural rearrangement of the Nafion took place along with the macro-structural deformation into the trenches. However, they didn't investigate its association with cell performance.

Catalyst Layer

Park *et al* studied fabrication temperatures on the initial microstructure of catalysts [75]. They used a field emission scanning electron microscope (FE-SEM) to characterize the distribution of pore size in catalyst layers after fabrication. At different fabrication temperatures, the physical structures of a catalyst layer changed, resulting in a variation in cell performance. Russell *et al* also investigated the associations between the original pore size and cell performance [76]. Apart from characterizing the pore size distribution,

they found that the best-performing sample had more small pores, which offered a better ability for oxygen diffusion; in contrast, the worst-performing sample had larger agglomerates, indicating larger electron, proton and diffusion resistance.

In probing more specifically into the microstructure changes of catalyst layers, Zhang *et al* conducted a quantitative analysis of catalyst layer degradations [77]. They proposed that the signature of an unused polymeric ionomer material was the island-like structures observed through a SEM test. However, in a used catalyst layer, more carbon particles resided on the membrane surface, which resulted from the dissolution or degradation of an ionomer at the surface during fuel cell operations. Hodnik *et al* studied platinum particle growth and platinum depletion after running the cell under severe simulated start-stop conditions (50000 cycles from 0.2V to 1.4V) [78]. A newly developed identical location SEM (IL-SEM) was used in this study. A non-uniform distribution of platinum existed across the used catalyst cross-section. Although carbon corrosion was missing in the sample, a large particle growth occurred on the top of the catalyst film.

TEM's higher resolutions make it possible to observe microstructural changes, such as Pt migration, particle coarsening, and catalyst agglomerations. More *et al*. used Blom's method to prepare TEM samples (cathode catalyst: 0.20 ± 0.01 Pt3Cr/cm^2; anode catalyst: 0.2 ± 0.01 Pt/cm^2) [79]. They found that, if cathode catalyst layers contain different amounts of Nafion ionomer, the microstructural change could be different, and that these microstructural differences were also associated with cell performance. In addition, a significant particle coarsening took place on both anode and cathode catalyst layers. The anode catalyst layer witnessed the migration of Pt to the anode-membrane interface.

Xian built upon Blom's research and detected that catalyst particles in a new catalyst layer were detached from the carbon surfaces, indicating that a weak bonding to the carbon-support surfaces resulted in a lower catalyst utilization [80]. Compared with that in a cathode catalyst, the pure Pt in the anode catalyst layer had a smaller average particle size and a better dispersion on carbon surface. After 1000 hours of operations, both the anode and cathode catalyst clusters appeared. However, a more extensive agglomeration prevailed on the cathode side. Cathode catalyst agglomerations mainly occurred in the first 500 hours, which was the main reason behind the initial performance degradation.

Cell impedance trends showed that a degradation of the recast ionomer may be the major cause of performance decay after 500 hours. Another interesting phenomenon that occurred in the aging through experiments was the Pt migration. They suggested that the amount of anode Pt migrating into the membrane was a function of cell operating times.

2.1.2. Quantitative Study (Mechanical Property Characterizations)

Gas Diffusion Layer

The stress-strain behaviour of GDLs provides perhaps the most significant prerequisite for a fuel cell degradation study. A GDL is a very thin layer (100~300 μm), composed of randomly oriented carbon fibres. Such a unique structure also makes it more vulnerable to compression, than other cell components. Under clamping and cyclic compressions, the GDL changes its physical structure as well as initial compressive behaviour, which deteriorates its functions and reduces cell performance [81,82]. In addition, most of the critical material parameters in terms of performance, such as electrical and thermal conductivities, gas permeability, and diffusivity, rely on the compressive behaviour of GDLs [83,84]. To date, some studies have concentrated on the mechanical degradation modeling of GDLs in PEM fuel cells. However, the reliability of the modeling largely depends on GDL's compressive property.

The compression experiment is the most convincing approach for GDL compressive behaviour measurements. Currently, numerical modeling and experimental measurements receive wide application in the determination of GDL's compressive behaviour [85,86,46]. However, the reliability of modeling suffers from some inevitable modeling assumptions. The discrepancy in results between modeling and experiments sometimes can reach 20%. Therefore, experimental measurement provides more meaningful assistance. Nevertheless, the compressive behaviour of GDLs under fuel cell operating conditions cannot be easily characterized experimentally due to its small thickness, and highly porous and random structure. In addition, such a characterization becomes even more challenging because common fuel cell operating temperatures, relative humidity and its cyclic changes are hard to mimic.

So far, some studies are available regarding GDL's thermal and electrical properties under different compressions. However, the compressive behaviour of the GDLs is often not a primary focus of these studies. Only few studies focus strictly on the compressive behaviour of GDLs. Based on these studies, a GDL shows a non-linear compressive behaviour, which is different from most assumptions in fuel cell modeling where a GDL has a linear compressive character. Yi *et al*. performed uniaxial tensile and compression tests in order to validate their numerical modeling [81]. Based on the observations from an optical microscope, they obtained thickness changes in GDLs as a function of compression loads, and found that stress-strain curves for both tension and compression tests were not linear.

Regardless of the type of GDLs being tested, stress-strain curves always exhibit non-linear correlations. Because of its micro-thickness, Radhakrishnan *et al*. stacked 10 paper-based and cloth-based GDL samples together for a better accuracy [83]. The stress-strain curve for a paper-based GDL had two distinct plateaus on the stress-strain curve. A similar phenomenon also existed in a cloth-based GDL. However, it was less rigid than a paper-based GDL. In addition, after its second plateau, the curve was non-linear which was different from that of the paper-based one. Sadeghi *et al*. draw a conclusion similar to Radhakrishnan's, that the paper-based GDL deformed non-linearly with compression forces [85]. Ismail *et al*. probed the GDL's mechanical properties using an INSTRON 5566 universal testing machine with a 10 kN load cell for a better accuracy. Three distinctive regions existed in compressive stress-strain curves [87]. In the first region (compression 0-0.01 MPa), the strain increased linearly and rapidly with the compressive stress. When the compression increased from 0.01 MPa to 1 MPa, the curve became non-linear and the slope decreased. After the compression levelled to more than 1 MPa, the stress-strain behaviour became linear again; however, its slope was much slower than that of the first region.

Upon obtaining the stress and strain curve, researchers tried to use mathematical correlations to describe the non-linear compressive behaviour of GDLs, including piecewise linear expressions and exponential correlations. Most of them observed that the GDL behaved differently within different compression ranges; therefore the piecewise

linear curve could best describe such a phenomenon. Mishra *et al*. measured the compressive modulus of different types of paper-based and cloth-based GDLs using an INSTRON universal electromechanical testing system [46]. For paper-based GDLs, the compressive curves had three piecewise linear regions based on the best-fit slope of the line from the corresponding three regions, whereas the curves for the cloth-based GDLs showed four linear regions. Meanwhile, an exponential correlation was also used. Safeghi *et al*. described the non-linear compression curve through an exponential correlation which assisted their analytical model to estimate the thermal conductivities of the GDLs [85]. Ismail *et al*, unlike all the others, indicated that a fourth order polynomial curve fitted their data better [86].

The compressive behaviour of GDLs with PTFE coatings is different from that of the raw GDLs. Escribano *et al*. mentioned that samples with PTFE coatings were less compressive than those without PTFE [43]. Sadeghifar *et al*. investigated the effect of PTFE contents on the compressive character of GDLs [88]. They measured the thickness changes of GDL samples with different PTFE contents as a function of compression pressures. Compared to the raw GDLs, samples with PTFE coatings had a similar non-linear trend, but with less strain reduction under the same compression force. Ismail *et al*. indicated that higher PTFE contents made the GDL stiffer and less compressible [87].

The common PEM fuel cell operation condition experiences inevitable condition changes in temperatures and relative humidity during start-up and shut-down processes, which leads to corresponding thermal-hygro stress changes. These changes in applied stresses can be treated as a cyclic compression. Escribano *et al* [43] found that a GDL presented a stable behaviour after the first compression, which was consistent with Mason's conclusions [89]. In order to probe the impact of cyclic loadings, Safeghi *et al*. exerted loading and unloading compressions on GDL samples [85]. After five cycles, there were no significant hysteresis effects in the loading and unloading curves. Moreover, the strain reduction was more significant in the first cycle. Mathias *et al*. carried out a 10-repeated cyclic experiment on paper-based GDLs and acquired similar results [90]. Radhakarishnan *et al*. simulated repeated opening and closing of fuel cell hardware by subjecting Toray paper GDL samples to five cycles of compressions [83]. Based on the

results, the cyclic compression caused irreversible changes to the structures and properties of GDLs. Their results also indicated that the thickness reduction of samples increased after each compression cycle, which was different from what was found by others.

Membrane

In order to setup a structure model for a PEM fuel cell, the mechanical properties of Nafion membranes need to be characterized first. Kai *et al* investigated the mechanical properties of Nafion membranes under different environmental conditions [91]. The results indicated that the mechanical properties of Nafion membranes were associated with temperatures and relative humidity. Building upon Kai's research, Patil *et al* explored the mechanical properties of Nafion membranes [92]. They found that its mechanical properties were associated with open circuit voltage conditions. Tang *et al*. studied the mechanical properties of a perfluorosulfonic acid (PFSA) membrane at different humidity and temperatures [93]. Tensile tests provided the Young's modulus, yield strength, break stress and strain. The results showed that the Young's modulus and yield strength decreased with humidity and temperatures. His research provided very meaningful data for the following modelling studies.

2.2. Modelling Study

2.2.1. Deformation Model

Recently, some mechanical degradation studies show that MEAs must be sufficiently durable to withstand mechanical stresses so that the cell can sustain its performance under various operating conditions and their cyclic changes [80,94,95,96,97]. Studying the stress and deformation distributions in an MEA during a cell assembly process and regular cell operations is therefore essential for understanding the mechanical degradation. In the past several years, due to the limitations in experimental techniques, many studies relied on the finite element method (FEM) to setup a structure model and probe the stress and deformation conditions.

Membrane

A reliable and comprehensive structure model requires an appropriate stress-strain model for different cell components in an MEA. Previous studies mainly focused on the stress-strain model for Nafion membrane because it has both elastic and plastic behaviour. Moreover, the hygro-stress is an essential factor in cell stress analysis because membranes tend to swell in a constrained space during cell operations.

Maher *et al*. built a full three-dimensional, multi-phase computational fluid dynamics model of a PEM fuel cell with straight flow channels, in order to investigate the displacement, deformation and stress inside the whole cell [98]. The model considered the effects of hygro- and thermal stresses. All the materials were assumed to be in the elastic region. Unlike other results, the membrane humidity swelling expansion in their simulation was constant. The results indicated that the temperature gradient and moisture change in the fuel cell when being operated induced a non-uniform distribution of stresses. This non-uniformity eventually resulted in bending stresses. These bending stresses might be the reasons behind the delamination between a membrane and catalyst layers.

In addition, cyclic loading is another significant factor in membranes' deformation because fuel cells experience inevitable start-up and shut-down processes. Kusoglu *et al*. developed a two-dimensional fuel cell assembly to reveal the stress evolutions of a PEM fuel cell subjected to a single hygro-thermal duty cycle [99]. They used two traditional methods (a constant displacement or a constant pressure) to simulate clamping forces. In order to study plastic deformations of the membrane during cycles, the membrane was assumed to be a linear-elastic, perfectly plastic material, whose material properties changed with temperatures and relative humidity. They found that hygro-thermal loading led to plastic deformations, and consequently the tensile residual stresses after the unloading. The in-plane stress was the largest stress component during the loading sequence, indicating that it controlled yielding behaviour. From their perspective, the residual in-plane stress in the membrane was the main reason for the occurrence of cracks and pinholes.

Some people have used material anisotropy in order to improve the reliability of membrane modelling. Kusoglu *et al*. improved their own model through two aspects

[100]. First, they did not assume that the membrane was a perfectly plastic material; instead, they considered that yield strength changes with plastic strains. Second, the impact of swelling anisotropy was investigated. They found that membranes with low in-plane swelling strains might have better performance during hydration-dehydration cycles.

Gas Diffusion Layer

A GDL has a highly porous structure, which makes its compressive behaviour very unique. In the experiments, people found that it have a non-linear stress-strain relationship. However, previous studies generally assumed that it has a linear stress-strain relationship. Serincan *et al*. developed a two-dimensional hydration modeling framework to investigate transport phenomena, electrochemistry and mechanical stresses in a PEM fuel cell [101]. They studied the mechanical stresses in a GDL due to thermal expansions and cell assemblies. A GDL was assumed to be elastic materials whose Young's modulus changes with a normal strain; hence, this model can predict only the elastic region of the stress-strain curve. Moreover, anisotropy in the mechanical properties of GDLs was accounted for in stress calculations.

MEA

Initially, many studies focused on the impact of assembly procedures and common operating conditions on MEAs. Firat *et al*. analyzed a fuel cell stack with an active area of 50 cm^2 from a mechanical point of view, using COMSOL Multiphysics [102]. Without considering the impact of humidity, they studied stress and strain conditions on the whole MEA. Despite relatively small temperature profiles for PEM fuel cells, high thermal expansion coefficient values of some components, such as the Nafion 112 membrane, caused noticeable changes in MEAs' deformation. Bograchev *et al*. developed a linear elastic-plastic two-dimensional model of a fuel cell, in order to investigate the mechanical stresses in MEAs during cell assembly procedures [103]. Contrary to the traditional way where relative displacement or a simple given pressure modeled the clamping force, this study used bolt torques. They analyzed both the stress distributions on the local and global scales. The corresponding experimental data were in an agreement

with numerical predictions. For the local scale analysis, the stress distribution in the membrane was non-uniform, reflecting a periodic character. When the torque reached 15.8 Nm, the MEA underwent plastic deformations.

2.2.2. Mechanical Degradation on Cell Performance

Very recently, some researchers began to employ the combination of a FEM method and a computational fluid dynamic (CFD) method [104,98] to study the cell performance with mechanical degradation. This coupled modelling method is superior because on one hand, it considers the effects of a degraded cell structure and its associated transport parameters on cell performance. On the other hand, it also takes into account the transport phenomena related to fuel cell operations, for example, non-uniform temperature distributions in a cell, providing a more detailed insight into the deformation conditions in a MEA. Consequently, structure-performance coupled model provides a more realistic approach to probe the mechanical imparts on cell performance. However, related research is very scarce.

2.3. Summary

Some studies have highlighted the mechanical degradation of PEM fuel cells; yet, the understanding of mechanical degradation in MEAs and their impacts on cell performance requires more significant efforts. For example, although SEM and TEM tests detailed structure changes, the mechanism behind degradation in MEAs still needs further clarification. In addition, since the mechanical properties of GDLs and catalyst layers were not the main focus in previous research, these properties are very scarce. This scarcity impairs the reliability of a structure model. Moreover, in the structure model, some assumptions might not be appropriate. For example, the GDL was assumed to have a linear stress-strain relation, which is not consistent with the experimental data. Additionally, the catalyst layer was ignored. In this case, previous structure model left a lot for improvement. Furthermore, some research started to couple the structure and performance model together to study the early stage of mechanical deformation on cell performance. However, related research is very scarce. In addition, to the best knowledge

of the author, currently there are few studies focusing on the late stage of mechanical degradation.

Therefore, this research, focusing on the mechanical degradation on cell performance, relies on four levels of processes to clarify this mechanism. First, experimental methods provided the characterization of the microstructures and their changes in MEAs after degradation. Then, various experimental tests provided a set of identified mechanical properties of MEAs and their degradations with various cell operating conditions, which guided the selection of appropriate material models. Next, a structure model and then a structure-performance coupled model enabled the study of the early and late stage of mechanical degradation on cell performance.

Chapter 3

Experimental Development

Experimental studies of mechanical degradation in PEM fuel cells mainly concentrated on four fields: I) morphological defects in new and degraded MEAs, II) Mechanical property characterizations of different components in PEM fuel cells, III) mechanical deformation and stress distributions of PEM fuel cells during operations, and IV) fuel cell performance characterizations. Among these four projects, Projects III and IV were validation experiments for their corresponding numerical modelling. This chapter describes the experimental design for these four studies.

3.1. Original Microstructures in MEAs and Their Changes

3.1.1. Fuel Cell Test Setup and Conditions

A commercial Nafion 117 based CCM with an active area of 42 cm^2 and two 230 μm-thick GDLs (coated with 30% PTFE by weight) sat in a single fuel cell assembly equipped with a parallel three-pass serpentine flow channel plate, as illustrated in Figure 3-1 and Figure 3-2. Table 3-1 shows all the cell properties. This fuel cell assembly rested in an environmental chamber and ran through an accelerated durability test. All the

experiments used the Fuel Cell Automated Test Station (FCATS-G20) manufactured by the Green-light Innovation Corp. This work station controlled all the cell operating conditions, including inlet temperatures, pressures, relative humidity, and stoichiometry of the reactant gases on both sides of a fuel cell. Table 3-2 presents the measurement accuracy. An onboard computer-based control and data acquisition system controlled and monitored the entire test process, as shown in Figure 3-3. Table 3-3 describes the operating conditions. These selections followed Xian's work [80], which shows that operating conditions with a high temperature of 90^{o}C, a high relative humidity of 100%, and a high stoichiometric air of 3.6 can intensify the degradation of MEAs. The cell current density had a constant value of 100 mA/cm^{2}; whereas the cell voltage was recorded every ten seconds. Figure 3-4 shows a typical test result. The cell voltage degraded from 0.7943 to 0.6788 V during the accelerated durability test within 250 hours.

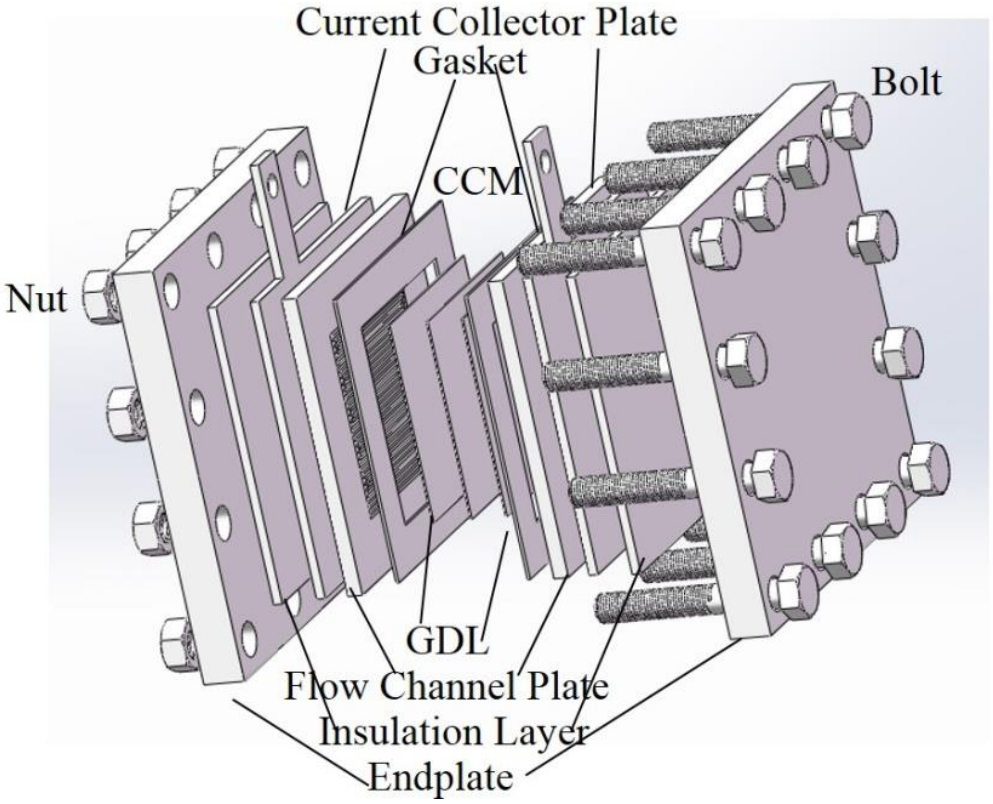

Figure 3-1 A schematic drawing of a single fuel cell assembly used in the durability testing

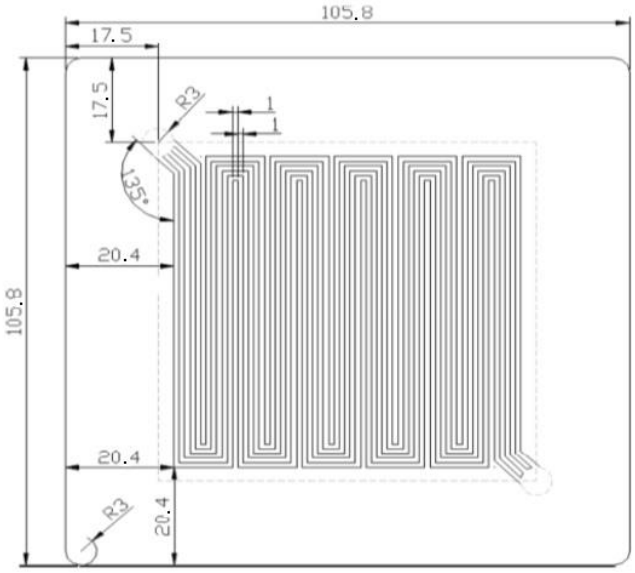

Figure 3-2 Flow distribution plate (all lengths are in the unit mm)

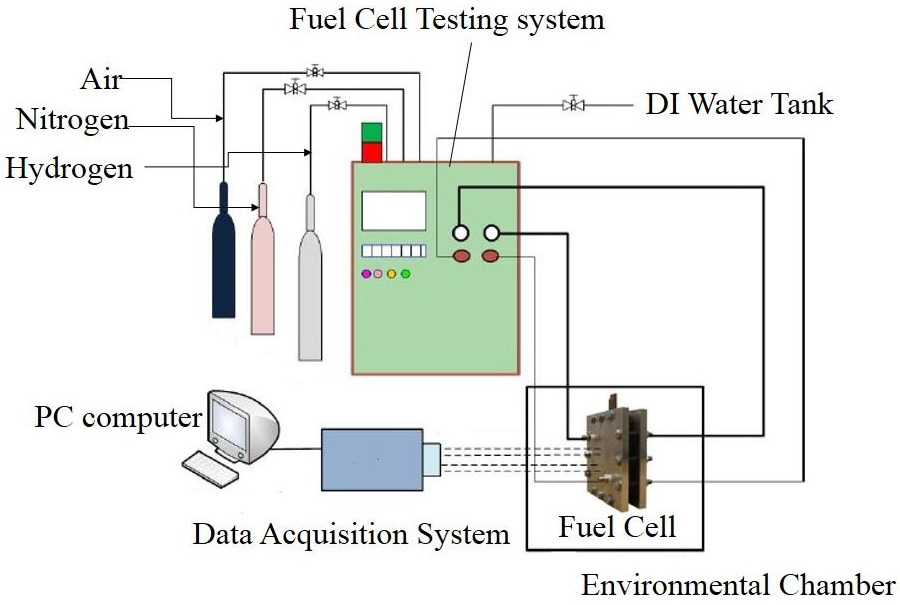

Figure 3-3 A schematic picture of the accelerated durability test setup

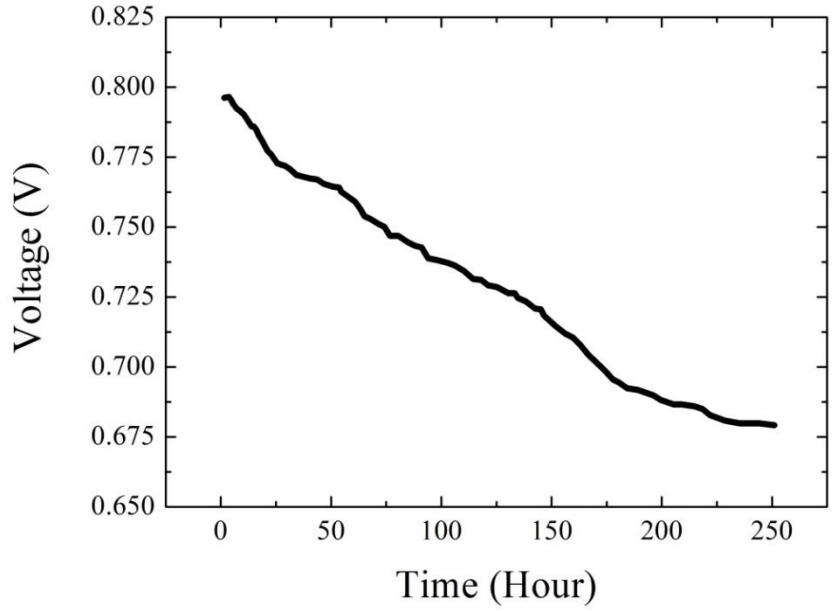

Figure 3-4 Voltage-time curve during the accelerated durability test subjected to a fixed current density (100 mA/cm^2)

Table 3-1 Fuel cell properties

Cell components	Properties	Value
CCM	Membrane type	Nafion 117
GDL (uncompressed, anode & cathode)	Thickness	230 μm
	Porosity	0.75
	PTFE loading by weight	30%
Gasket	Material	Silicon rubber
	Thickness	254 μm
Flow channel layout	Type	Parallel serpentine
	Number of flow channels in parallel	3
	Channel width	1 mm
	Channel depth	1 mm
	Channel width	1 mm
Cathode flow field plate	Material	Graphite
	Thickness	4 mm
	In-plane area	110.25 cm^2
End plates	Material	Aluminum
	Thickness	13 mm
	In-plane area	210.25 cm^2

Table 3-2 Measurement accuracy

Measurement	Accuracy
Temperature (supplied gases and deionized water)	±1°C
Volume flow rate (supplied gases)	±0.4 mL min^{-1}
Gauge pressure (at inlet and outlet of flow channel layout)	±1 kPa
Load box-constant current	±0.25%
Load box-constant voltage	±0.25%
Relative humidity	±5%

Table 3-3 Operating conditions

Operating temperature	90 °C
Gas flow rates	Anode: 1.2 stoichiometric ratio Cathode: 3.6 stoichiometric ratio
Humidified gases	100% 90°C H_2 100% 90°C Air
Anode & cathode pressure	50 kPa

3.1.2. General Fuel Cell Assembly and Experimental Procedures

A proper cell assembly procedure is significant for cell performance as well as for avoiding the morphological defects that might be unduly introduced during assembly processes. Therefore, this study followed an established standardized cell assembly procedure. A room temperature of 25°C with a relative humidity of 30% provided a typical assembly working condition. Figure 3-1 illustrates the assembly procedures.

In order to obtain precise dimensions, a shape template and a sharp knife provided correct cutting sizes to a GDL and a silicon gasket. A GDL's real area should be slightly larger than its designed active area, so that it can fully cover the flow channels. An endplate sat on a horizontal and stable desk. Then a current collector plate lay on top of it, with an insulation layer in between the endplate and the collector plate. A sheet of raw GDL without PTFE coating rested between the current collector plate and the flow distribution plate, to ensure an ideal electrical conductivity. A PTFE-coated GDL lay directly on top of the flow field plate. Normally, only one side of a GDL had PTFE coating. The uncoated side faced towards the flow channels. A silicon gasket sat around the GDL edges. A CCM rested on top of the GDL. The application of four stainless steel pins

ensured an acceptable alignment between different fuel cell components. The assembly of the second half of a cell followed a similar method. A GDL, followed by a silicon gasket, a flow distribution plate, a current collector plate and, finally, an endplate, was stacked on a CCM. All the components needed to be aligned with each other to prevent leaking.

Bolts and nuts finally tightened the single fuel cell. Normally, an even force applied on each bolt is realized using a torque wrench; however, this technique suffers from inconsistent or uncalibrated friction between the fastener and its mating hole. The combination of a shim stock and a torque wrench provided a solution to this issue. The shim stock rested around the edge of the flow channel plate, with a thickness of 0.63 mm ±10%. The fuel cell assembly underwent a leakage test. Nitrogen was used to test for leaking from the fuel cell at both the anode and cathode sides.

This experiment also followed a standardized experimental procedure. The fuel cell assembly first rested inside the environment chamber and was properly connected to the fuel cell test station, as shown in Figure 3-3. Then, the activation of the fuel cell test station and the environmental chamber started, bringing the initial condition to the pre-set operating condition. The entire test system took about 90 minutes to reach a steady state. After the entire test system reached a steady state, the data acquisition process started.

3.1.3. Measurement of Contact Pressures

For contact pressure measurement, fuel cells were not in live operations. The experiments were carried out at a fixed room temperature of 25^{o}C and a relative humidity of 30% to study the effect of clamping force on the stress distribution. The measurement of the contact pressure in the fuel cell stack relies on the Fuji pressure indicating film. This film is specially designed for measuring a clamping force (spatial resolution 5-15 microns; accuracy ±2%). First, a pressure indicating film underwent a cutting process to be the same size as the MEA. For different measurements, it sat either between the flow distribution plate and the GDL, or between the GDL and the CCM. The assembly force contributed to the red patch developing on the pressure indicating film. The density of this red colour changes depending on the amount of force applied. For example, the area with a deep red colour indicates a large applied force; conversely the area with a light red

colour represents a low applied force. This technique is a widely recognized approach of measuring the stress field in the fuel cell stack. In addition, image processing and analysis of the pressure indicting film provided the stress mapping.

3.1.4. SEM Sample Preparation

During SEM sample preparation, the freeze-fracturing method ensured the preservation of the spatial relationships among the cross section in an MEA. This method has minimal impacts on original structures [13]. The CCM was first submerged in liquid nitrogen for five minutes. Then it was broken in half when still submerged. After that, the sample rested on an SEM viewing stub using a carbon-coated tape. This SEM test relied on a JEOL JSM6464 scanning electron microscope with an Oxford INCA Energy EDS system (magnification 5-300,000; resolution 3.00 nm; accelerating voltage 0-30 KV).

3.2. Experimental Characterizations of Mechanical Properties of GDLs

3.2.1. Compression Measurement Apparatus

This compression testing relied on two different compression measurement apparatuses: an INSTRON 5548 micro-tensile/compressive tester and a fully automated self-made compression testing station. An INSTRON 5548 tester, an ultra-high precision measurement apparatus, receives wide recognition for small assemblies or miniature specimens. In this experiment, the compressive testing of GDLs at room conditions used an INSTRON 5548 (Preload: rate 0.4 mm/min; load 5 N; Testing: rate 0.2 mm/min; maximum load 500 N). However this INSTRON tester is not applicable for cyclic testing, high temperature or humidified conditions. The need to study the effects of temperatures and relative humidity on GDLs necessitated the usage of a self-made testing apparatus equipped with an environmental chamber. As illustrated in Figure 3-5**,** this apparatus consisted of two calibrated electrolytic iron rods, a Velmex stepper motor, and a Honeywell Sensotec load. The sample (GDLs) was compressed between the two calibrated rods (Load measurement accuracy: ± 0.5 % of reading; Position control

resolution: 20 nm; Position measurement accuracy: ±0.5 μm). The lower rod was fixed whereas the upper rod, attached to a vertical slide, was movable and controlled by a Velmex stepper motor. This machine provided a series of prescribed clamping forces. The load cell measured the compression force and the stepper motor provided compressions up to 100 lbs.

The movements of the upper rod determined the thickness reduction. First, the stepper motor compressed the lower rods to a set of desired compression forces and recorded the positions at each compression force. Then, a sample rested on the lower rod surfaces and was compressed to the first compression force in the set. Once the compression force reached the desired value (±2%) in the set, the data acquisition system automatically recorded the compression force and the stepper motor position. Finally, subtracting the position of the stepper motor from the previously recorded position without the sample in place determined the sample thickness. After the procedure, the stepper motor compressed the sample to the next desired force and repeated the measurement procedure.

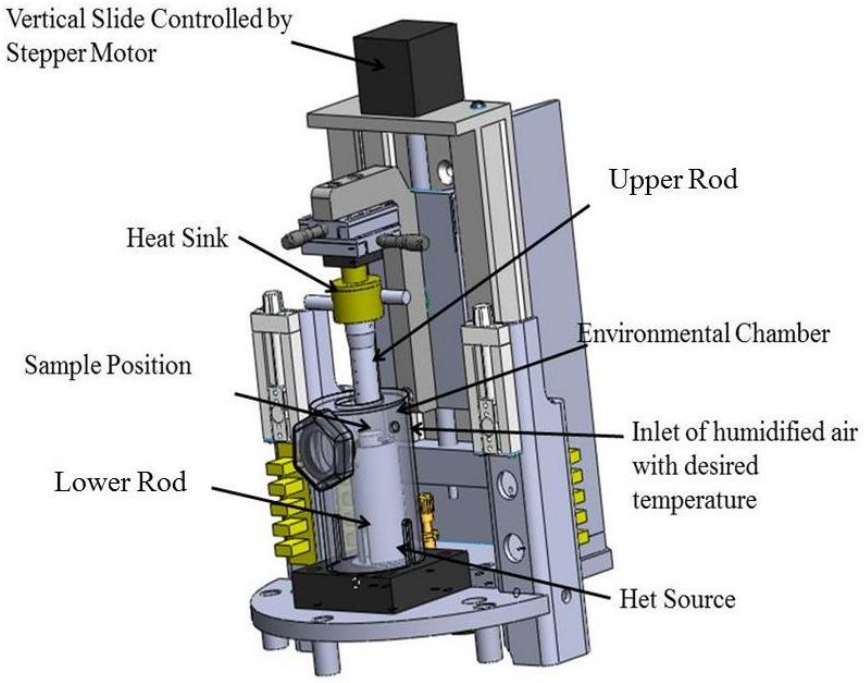

Figure 3-5 A schematic picture of the fully automated compression testing station

The lower rod obtained heat by an electric heater, while the upper rod was heated by circulating warm water from a constant thermal bath (manufactured by thermo scientific). These two rods heated the sample to the testing temperature. Further, an additional environmental chamber, as shown in Figure 3-5, was connected with a fuel cell automated test station, manufactured by Green Energy, which provided humidified air at desired temperatures. The environmental chamber wrapped with heating films which aimed to prevent excessive condensations at a high relative humidity. Pyrogel XT-E, a hydrophobic flexible thermal insulator, wrapped the outside of the heating films, ensuring a better insulation. A DC power generator offered power to the heating film. To keep a stable temperature across the sample during the test, the thermal bath, the electric heater for the lower rod, and the electric heating film for the chamber had the same temperature for each measurement.

3.2.2. Standard Porosimetry Measurement

A Porotech standard porosimeter 3.1 provided the porosity measurement of new and compressed GDLs. The porosity refers to the volume ratio of pores to the total volume of a material, as shown in Equation 3-1. It is a non-destructive testing method, which allows testing of the same sample before and after compressions. It relies on the law of capillary equilibrium, that is, if two or more porous bodies are filled with a wetting liquid and are at capillary equilibrium, then the capillary potentials for each of these porous bodies are equal [105]. The testing involved three porous samples: two calibrated standard porous samples with known porosity, and one testing sample. During the testing, these three samples were sandwiched. The two standard samples were on the top or bottom, while the testing sample rested in the middle. Once the standard samples and test sample were in contact, the capillary equilibrium formed by the flow of liquid and vapour, which was due to the capillary potential gradient. Volfkovich [105] provided more details for this approach. This principle provided the basis for the relationship determination between the liquid content in the test sample and that in the standards using the mass variation of the wet porous samples. Finally, the given pore size distribution curves of the standard sample, provided by Porotech Ltd, contributed to the porosity measurement of the testing sample,

$$\varepsilon = \frac{V_p}{V_t} = \frac{V_p}{\frac{1}{4}\pi d^2 \delta} = \frac{(m_{sat-bs} - m_b) - (m_{dry-bs} - m_b)}{\frac{1}{4}\pi d^2 \delta \rho}$$

Equation 3-1

where, ε is the porosity of the material; V_p is the bulk volume of the pores; d is the diameter of the test sample; δ is the thickness of the test sample; m_{sat-bs} is the total mass of the saturated sample and clean bottle; m_{dry-bs} is the total mass of the dry sample and clean bottle; m_b is the mass of the clean bottle; and ρ is the density.

3.2.3. Scanning Electron Microscope and Optical Microscopy

A scanning electron microscope (SEM, JEOL JSM6464) and an optical microscope (AXIO Zoom, V16 Zeiss) detailed the microstructure of both fresh (before compression test) and compressed GDLs. Using the freezing fraction method helped to preserve the spatial relationships among the cross section of GDLs for the sample preparation.

3.2.4. Measurement Conditions and Procedures

The experimental conditions in this testing included temperatures and relative humidity. In order to simulate the real fuel cell operating conditions and study their effects, the temperature range was set from 25^{o}C to 85^{o}C, while the relative humidity range was set from 30% to 85%. To perform the testing in a stable condition (a stable temperature and relative humidity), the thermal bath, the electric heater, and the electric heating film reached the same temperature for each test two hours before the test. The humidified air started to fill out the environmental chamber after the chamber temperature became stable. The GDL samples had a disc shape. Before the experiments, it had SEM and OM testing, to record the initial microstructures. Then, the GDL samples rested in the environmental chamber for at least one hour, so that the testing sample can be fully heated and humidified. After the compression testing, the sample underwent the SEM and the OM testing again.

3.2.5. Uncertainty Analysis

3.2.5.1. Compressive Behaviour Measurement

Since the bias of the parameter measurement and the error of random variations are completely independent of each other, the errors in stresses and strains are composed of errors from two sources: the measurement parameter bias and the measurement process random (repeatability) error, as shown below in Equation 3-2.

$$u = \sqrt{\varepsilon_b^2 + \varepsilon_r^2}$$

Equation 3-2

where ε_b^2 is the error due to the parameter bias, ε_r^2 is the random error, and u is the uncertainty. The standard deviations of both stresses and strains, calculated from repeated measurements, are equal to the random errors. However, the parameter biases for stresses and strains are a weighted sum of the constituent errors because their measurements are involved more than one variable, as shown in Equation 3-3 and Equation 3-4.

$$\varepsilon_{b,stress} = \sqrt{\left(\frac{1}{\frac{1}{4}\pi d^2}\varepsilon_{b,f}\right)^2 + \left(\frac{F}{\frac{1}{8}\pi d^3}\varepsilon_{b,d}\right)^2}$$

Equation 3-3

$$\varepsilon_{b,strain} = \sqrt{\left(\frac{l}{l_0^2}\varepsilon_{b,ol}\right)^2 + \left(\frac{1}{l_0}\varepsilon_{b,dis}\right)^2}$$

Equation 3-4

where d is the diameter of the sample; F is the force applied on the sample; l_0 is the original thickness of the sample, measured by an electric disk micrometer; l is the displacement of the sample thickness; $\varepsilon_{b,f}$ is the parameter bias for the force measurement; $\varepsilon_{b,d}$ is the parameter bias for the sample diameter measurement; $\varepsilon_{b,ol}$ is the parameter bias for the original thickness measurement; and $\varepsilon_{b,dis}$ is the parameter bias for the displacement measurement.

3.2.5.2. Porosimetry measurement

The uncertainty of the pore volume $(\Delta\theta_{rss})_v$ is ±0.075%, calculated by Equation 3-5. The uncertainty of the porosity $(\Delta\theta_{rss})_\varepsilon$ is ±0.6%, calculated by Equation 3-6, as shown below.

$$(\Delta\theta_{rss})_v = [\left(\frac{\partial V_{po}}{\partial m_{saturate}}\Delta u_m\right)^2 + \left(\frac{\partial V_{po}}{\partial m_{dry}}\Delta u_m\right)^2 + \left(\frac{\partial V_{po}}{\partial \rho_{octane}}\Delta u_\rho\right)^2]^{\frac{1}{2}}$$

Equation 3-5

$$(\Delta\theta_{rss})_\varepsilon = [\left(\frac{\partial \varepsilon}{\partial V_{po}}\Delta u_{V_{po}}\right)^2 + \left(\frac{\partial \varepsilon}{\partial d}\Delta u_d\right)^2 + \left(\frac{\partial \varepsilon}{\partial \delta}\Delta u_\delta\right)^2]^{\frac{1}{2}}$$

Equation 3-6

3.3. Experimental Characterization of Mechanical Properties of Catalyst Layers

The mechanical property measurement of catalyst layers relied on a robust technique, the nanoindentation technique, which helps to determine thin film properties for which conventional testing are not feasible. The nanoindentation involves small loads and an indenter with a known geometry which is called Berkovich tip, as presented in Figure 3-6. This tip ensures the determination of the indent area. During the course of the instrumented indentation process, the Berkovich tip gradually penetrates the tested sample. Meanwhile, a record of the depth of penetration is made. These data are plotted on a graph to create a load-displacement curve, which enables the determination of the mechanical properties in the tested sample.

As shown in Figure 3-7, the slope of the curve, *dP/dh*, upon unloading is indicative of the stiffness, *S*, of the contact, as presented in Equation 3-7. h_{max} is the maximum displacement at the maximum load P_{max}. Then, the determination of the reduced Modulus, E_r, depends on the stiffness of the contact, as presented in Equation 3-8 and Equation 3-9. A_P is the projected area on the specimen by the indenter. h_c is the contact depth. Eventually, the determination of the specimen's Young's modulus relied on Equation 3-10. Diamond indenter modulus, E_i, and Poisson's ratio, υ_i, were taken as

1140 GPa and 0.07, respectively. E_s and υ_s are the Young's modulus and Poisson's ratio of the tested material. υ_s was 0.25 in the test.

$$S = \left(\frac{dP}{dh}\right)_{h=h_{max}}$$

Equation 3-7

$$E_r = \frac{\sqrt{\pi}}{2}\frac{S}{\sqrt{A_p(h_c)}}$$

Equation 3-8

$$A_P = 24.5(h_c)^2$$

Equation 3-9

$$\frac{1}{E_r} = \frac{1-\upsilon_s^2}{E_s} + \frac{1-\upsilon_i^2}{E_i}$$

Equation 3-10

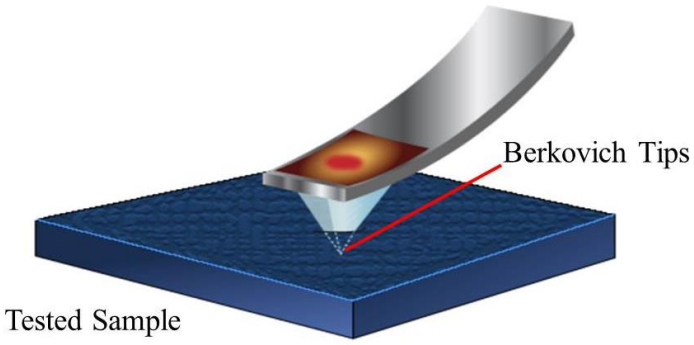

Figure 3-6 A schematic drawing of a nanoindentation test

3.4. Validation Experiments for the Cell Structure Model

3.4.1. Experimental Setup

The experimental apparatus, as presented in Figure 3-8, contributed to the investigation of the mechanical deformation behaviour in an MEA during regular cell operations. This test relied on a standard Ballard fuel cell stack with an active area of 45 cm^2. The MEA consists of a Nafion membrane, two catalyst layers, and two GDLs. The standard Ballard

fuel cell included a pressurized bladder that provides uniform compression over the reaction sites. The bladder, connected to a source of compressed air, kept a constant pressure of 0.4 MPa.

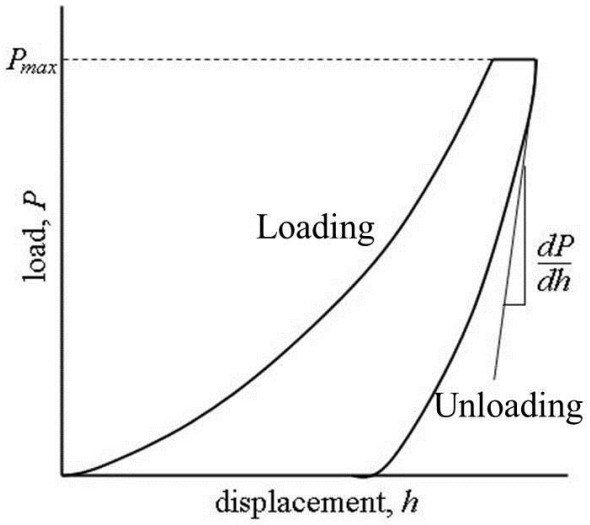

Figure 3-7 A load-displacement curve for an instrumented nanoindentation test

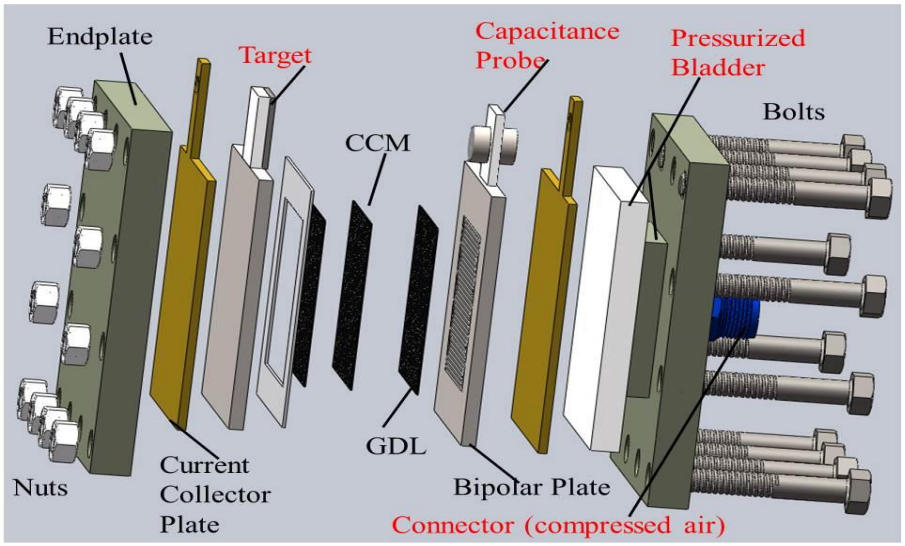

Figure 3-8 Experimental setup for MEA validation testing

An accumeasure system 9000 equipped with capacitance probes offered the measurement for the thicknesses changes of an MEA in a Ballard fuel cell stack. The probe and target

sat firmly on the top of the bipolar plates of the anode and cathode sides, respectively. The probe and target holders ensured an excellent mechanical stability and a high electrical resistance, which also kept the probe facing parallel to the target. The electrical capacitance formed between the accumeasure probe and the target surface varies as a function of the distance between the two bipolar plates. The variations of this distance, resulting from the thermal expansion, swelling and shrinkages of the MEA, are directly proportional to the displacement of the MEA.

3.4.2. Experimental Procedure

Commission processes including leakage and crossover tests were carried out prior to the displacement measurement. A heating-bath, manufactured by Thermo-Fisher scientific company, controlled the temperature of the fuel cell stack. The heated DI-water from the heating-bath flowed into the cooling plates of the fuel cell stack and circulated between the heating-bath and the cooling plates, making a stable temperature. The Greenlight-G40 fuel cell testing station supplied the heated nitrogen gas with a desired humidity into the anode and cathode inlets of the cell stack. The Accumeasure system 9000 recorded each displacement measurement of the MEA at a frequency of 1 Hz; meanwhile data acquisition system (NI-DAQ) and thermocouple (T-type) monitored the stack temperature. This experimental procedure ensured that the measurement of the MEA deformation was accurate. Table 3-4 shows the measurement accuracy.

Table 3-4 Measurement accuracy

Measurement	Accuracy
Temperature (supplied gases and deionized water)	±1 ^{o}C
Volume flow rate (supplied gases)	±0.4 mL min^{-1}
Relative humidity	±5%

3.5. Validation Experiments for the Cell Performance Model

The polarization performance measurement relied on a Ballard standard fuel cell stack with an active area of 45 cm^2. A G20 fuel cell testing station controlled the operating conditions, including the gas flow pressure, temperatures and relative humidity. The cell

performance test was carried at a cell temperature of 75 ˚C, a relative humidity of 100% and an inlet gauge pressure of 35 kPa. The activation procedure lasted for 16 hours. Three-time repeated polarization tests confirmed the measurement repeatability.

3.6. Summary

This chapter describes the experimental design for studying the microstructures of original and deformed MEAs, and for measuring the mechanical property of different cell components. It also explains the corresponding experimental procedures and uncertainty analysis. In addition, it clarifies the experimental designs for validating the structure and the cell performance models.

Chapter 4

Model Development

Studies of mechanical degradation in PEM fuel cells focused on numerical modelling for two issues. The fuel cell structure model characterized the stress and strain conditions of an MEA during common and cyclic operating conditions, whereas the cell performance model described the real-time activity of a PEM fuel cell with a deformed MEA, quantified through the structure model. This chapter provides the essential information about these two models, including physical models, assumptions, model formulations, boundary conditions and corresponding validation results.

4.1. PEM Fuel Cell Structure Model

4.1.1. Physical Model

A comprehensive PEM fuel cell structure model involves force equilibrium equations, compatibility equations, constitutive equations for different cell components and appropriate boundary conditions. A typical single PEM fuel cell stack normally consists of two steel endplates, two current collectors, two graphite flow channel plates, two GDLs, two catalyst layers and one Nafion membrane. Figure 1-1 illustrates the schematic

drawing of a typical single fuel cell stack. However, because of the limitation in computational power, the structure model usually involves simplifications. Figure 4-1 shows a simplified single channel PEM fuel cell model, which was made up of two graphite channel plates, two GDLs, two catalyst layers and one membrane.

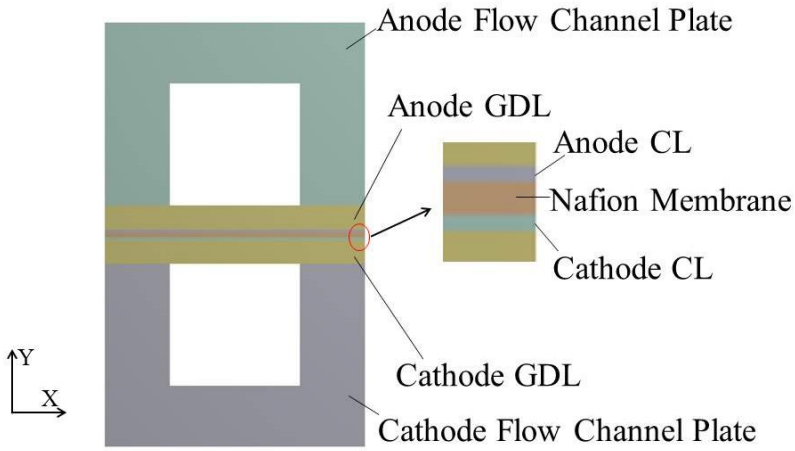

Figure 4-1 A schematic drawing of a single PEM fuel cell channel

4.1.2. Assumptions

- A perfect assembling of different components was assumed. The sliding was considered to be negligible. The stresses transmitted completely on the interfaces
- Simplified temperature and humidity distributions were assumed. Humidity gradient and temperature gradient from the cathode to the anode were ignored. The temperature and humidity distributions were uncoupled.
- All material properties were assumed to be isotropic, including isotropic swelling and thermal expansions.

4.1.3. Governing Equations

4.1.3.1. Force Equilibrium and Compatibility Equations.

In continuum mechanics, a solid body is assumed to be composed of a set of infinitesimal cells. Each cell is connected to its neighbour cell without any gaps or overlaps. Based on this theory, Force equilibrium equations are proposed. They are the most essential equations in solid mechanics modelling, which defines that the externally applied loads

equal to the total internal element forces at all joints or node points of cells in a structure. Solving a solid mechanics issue requires that the differential equations of equilibrium for all infinitesimal cells within the solid must be satisfied.

Equation 4-1 illustrates the three-dimensional force equilibrium equations of an infinitesimal element. The body force component, K_i , is per unit of volume in the *i*-direction. Because $\tau_{xy=}\tau_{yx}$, the infinitesimal element is automatically in rotational equilibrium.

$$\frac{\partial \sigma_x}{\partial x}+\frac{\partial \tau_{xy}}{\partial y}+\frac{\partial \tau_{xz}}{\partial z}+K_x=0$$

$$\frac{\partial \sigma_y}{\partial y}+\frac{\partial \tau_{yx}}{\partial x}+\frac{\partial \tau_{yz}}{\partial z}+K_y=0$$

$$\frac{\partial \sigma_z}{\partial z}+\frac{\partial \tau_{zx}}{\partial x}+\frac{\partial \tau_{zy}}{\partial y}+K_z=0$$

Equation 4-1

In continuum mechanics, strains are defined as displacements of the structure per unit length. Compatibility equations mean that when all material particles in a component deform, translate and rotate, they need to meet up again very much like the pieces of a jigsaw puzzle must fit together. If the small displacement fields, u_x, u_y and u_z are specified, the consistent strains can be calculated using the following Equation 4-2. Then, the compatibility equation can be written as Equation 4-3, which can be symbolically as $R_{ijkl}=0$. Since *i, j, k* and *l* have values ranging from 1 to 3, Equation 4-3 has a total of 81 equations. However, because $R_{ijkl}=R_{klij}$ and $R_{ijkl}=-R_{jikl}=-R_{ijlk}$, 81 equations can be reduced into 6 equations. Equation 4-4 shows the three-dimensional compatibility equations of an infinitesimal element.

$$\varepsilon_x=\frac{\partial u_x}{\partial x}$$

$$\varepsilon_y=\frac{\partial u_y}{\partial y}$$

$$\varepsilon_z = \frac{\partial u_z}{\partial z}$$

$$\gamma_{xy} = \frac{\partial u_x}{\partial y} + \frac{\partial u_y}{\partial x}$$

$$\gamma_{xz} = \frac{\partial u_x}{\partial z} + \frac{\partial u_z}{\partial x}$$

$$\gamma_{yz} = \frac{\partial u_y}{\partial z} + \frac{\partial u_z}{\partial y}$$

Equation 4-2

$$\frac{\partial^2 \varepsilon_{ik}}{\partial x_j \partial x_l} + \frac{\partial^2 \varepsilon_{jl}}{\partial x_i \partial x_k} - \frac{\partial^2 \varepsilon_{jk}}{\partial x_i \partial x_l} - \frac{\partial^2 \varepsilon_{il}}{\partial x_j \partial x_k} = 0$$

Equation 4-3

$$2\frac{\partial^2 \varepsilon_x}{\partial y \partial z} = \frac{\partial}{\partial x}\left(-\frac{\partial \gamma_{yz}}{\partial x} + \frac{\partial \gamma_{xz}}{\partial y} + \frac{\partial \gamma_{xy}}{\partial z}\right)$$

$$2\frac{\partial^2 \varepsilon_y}{\partial x \partial z} = \frac{\partial}{\partial y}\left(\frac{\partial \gamma_{yz}}{\partial x} - \frac{\partial \gamma_{xz}}{\partial y} + \frac{\partial \gamma_{xy}}{\partial z}\right)$$

$$2\frac{\partial^2 \varepsilon_z}{\partial y \partial x} = \frac{\partial}{\partial z}\left(\frac{\partial \gamma_{yz}}{\partial x} + \frac{\partial \gamma_{xz}}{\partial y} - \frac{\partial \gamma_{xy}}{\partial z}\right)$$

$$\frac{\partial^2 \varepsilon_x}{\partial y^2} + \frac{\partial^2 \varepsilon_y}{\partial x^2} = 2\frac{\partial^2 \gamma_{xy}}{\partial x \partial y}$$

$$\frac{\partial^2 \varepsilon_y}{\partial z^2} + \frac{\partial^2 \varepsilon_z}{\partial y^2} = 2\frac{\partial^2 \gamma_{yz}}{\partial y \partial z}$$

$$\frac{\partial^2 \varepsilon_z}{\partial x^2} + \frac{\partial^2 \varepsilon_x}{\partial z^2} = 2\frac{\partial^2 \gamma_{xz}}{\partial x \partial z}$$

Equation 4-4

4.1.3.2. Stress-Strain Relationship (Constitutive Relations)

Gas Diffusion Layer

Unlike other components in a PEM fuel cell, which can be simply classified as an elastic material or a plastic material, the gas diffusion layer is very unique. Previously, researchers treated it as an elastic material [100,99,23]; however, compression testing shows that a GDL actually does not have a linear stress-strain relation. In addition, its porous structure and micro-thickness make it very challenging to go through tensile testing. To date, we have already characterized GDLs' mechanical properties using compression testing. Here, we want to use this experimental data to model GDL's mechanical behaviour.

The hyperelasticity material model, called Blatz-Ko model, was the selection for GDLs' mechanical behaviour modelling, including its non-linear compressive behaviour and corresponding cyclic changes, because the compression data at hand can provide the required parameters for this model. The constitutive behaviour of hyperelastic materials is usually derived from the strain energy potentials. The stretch ratio, λ, and the stretch invariant, *I*, are used to describe material deformations, which are defined in Equation 4-5 and Equation 4-6. *J* is the total volumetric ratio. The strain energy potential, *W*, can be a function of the stretch ratios or the strain invariants, as shown in Equation 4-7. Equation 4-8 determines the stress and strain relationship. Due to the material incompressibility, the strain energy potential can be split into the deviatoric term, W_d, and the volumetric term, W_V, as shown in Equation 4-9. As shown in Equation 4-10 and Equation 4-11, $\overline{I_t}$ is the deviatoric invariants. $\overline{\lambda_x}$ is the deviatoric principal stretches. The Blatz-Ko model has the following form, as presented in Equation 4-12. μ is the shear modulus. This model assumed the effective Poisson's ratio as 0.25.

$$\lambda_x = \varepsilon_x + 1$$

$$\lambda_y = \varepsilon_y + 1$$

$$\lambda_z = \varepsilon_z + 1$$

Equation 4-5

$$I_1 = \lambda_x^2 + \lambda_y^2 + \lambda_z^2$$

$$I_2 = \lambda_x^2\lambda_y^2 + \lambda_y^2\lambda_z^2 + \lambda_x^2\lambda_z^2$$

$$I_3 = \lambda_x^2 \lambda_y^2 \lambda_z^2 = 1 + \left(\frac{\Delta V}{V}\right)^2 = J^2$$

Equation 4-6

$$W = W(I_1, I_2, I_3,) \text{ or } W = W(\lambda_1, \lambda_2, \lambda_3,)$$

Equation 4-7

$$\sigma = \frac{\partial W}{\partial \varepsilon}$$

Equation 4-8

$$W = W_d(\overline{I_1}, \overline{I_2}) + W_V(J)$$

$$W = W_d\left(\overline{\lambda_x}, \overline{\lambda_y}, \overline{\lambda_z}\right) + W_V(J)$$

Equation 4-9

$$\overline{\lambda_i} = J^{\frac{-1}{3}} \lambda_i$$

Equation 4-10

$$\overline{I_i} = J^{\frac{-2}{3}} I_i$$

Equation 4-11

$$W = \frac{\mu}{2}\left(\frac{I_2}{I_3} + 2\sqrt{I_3} - 5\right)$$

Equation 4-12

Nafion Membrane

An elasto-plastic model with isotropic hardening simulated the mechanical behaviour of a Nafion membrane. An elasto-plastic model means that a material has both elastic and plastic material behaviours. The characteristic feature of elastic material behaviour is that the elastic strain returns to zero at complete unloading, whereas plastic strain remains after complete unloading. An additive composition of the strains by their elastic and plastic parts is shown in Equation 4-13.

$$\varepsilon = \varepsilon^{el} + \varepsilon^{pl} + \varepsilon^{T} + \varepsilon^{S}$$

Equation 4-13

The traditional Hooke's law determines the elastic strains ε^{el}. As soon as the initial yield stress is reached, plastic strains ε^{pl} occur. ε^{T} is the thermal strain, whereas ε^{S} is the swelling strain, induced by the relative humidity. Defining the correlation between stress and strain for a plastic material is difficult because the plastic strain state is also dependent on the loading history. In order to determine the correlation of plastic strains, the constitutive description of plastic material behaviour includes a yield condition, a flow rule and a hardening law.

Yield Condition

The yield condition determines if the relevant material suffers plastic strains at a certain stress state. It can be split into a pure stress fraction, $f(\sigma)$, called the yield criterion (i.e. the equivalent stress), and an experimental material parameter, $k(\varphi)$, called the flow stress (i.e. yield stress). Hence, Equation 4-14 presents its form. If $F(\sigma, \varphi) < 0$, the material only shows elastic material behaviour. If $F(\sigma, \varphi) = 0$, the material experiences plastic deformations.

$$F(\sigma, \varphi) = f(\sigma) - k(\varphi)$$

Equation 4-14

There are many different yield criterions. Here, the Von Mises yield criterion, also called as J_2-flow theory, was selected for Nafion membrane, which had the assumption that yielding begins when the elastic energy of distortion reaches a critical value. The VON Mises stress is shown in the Equation 4-15.

$$f(\sigma) = \sqrt{\frac{\left(\sigma_x - \sigma_y\right)^2 + \left(\sigma_y - \sigma_z\right)^2 + (\sigma_z - \sigma_x)^2}{2}} = \sqrt{\frac{3}{2} S_{ij} S_{ij}}$$

Equation 4-15

S_{ij} is the component of the deviatoric stress. $S_{ij} = \sigma_{ij} - \frac{1}{3}(\sigma_x + \sigma_y + \sigma_z)\delta_{ij}$. Therefore, the yield condition using the Von Mises yield criterion can be written as Equation 4-16.

$$F(\sigma, \varphi) = \sqrt{\frac{3}{2} S_{ij} S_{ij}} - k(\varphi) = 0$$

Equation 4-16

Flow Rule and Hardening Rule

The flow rule describes the evolution of the infinitesimal increments of the plastic strain, $\delta\varepsilon^{pl}$ in the course of the load history of the body. The hardening rule describes the change in yield condition with the progression of plastic deformation. According to the hardening rule, the yield condition is determined by the plastic work, δw^{pl}, during each incremental plastic strain, $\delta\varepsilon_{ij}^{pl}$. As a result, the increment of plastic work for each incremental plastic strain is shown in the following Equation 4-17:

$$\delta w^{pl} = \sigma_{ij} \delta\varepsilon_{ij}^{pl} \ ,$$

Equation 4-17

where σ_{ij} is the stress components, satisfying the yield condition and producing the corresponding plastic strain increment, $\delta\varepsilon_{ij}^{pl}$. According to the flow rule, the incremental plastic strain is normal to the yield surface, which is described in the following form, Equation 4-18:

$$\delta\varepsilon_{ij}^{pl} = \delta\lambda \left(\frac{\partial f}{\partial \sigma_{ij}}\right)_{f-Y=0},$$

Equation 4-18

where $\delta\lambda$ is a scalar multiplier. In addition, the correlation between the equivalent incremental plastic strain and incremental plastic strain component can be described in Equation 4-19. Based on Euler's theorem, it can be rewritten as Equation 4-20. Finally, we can obtain, $\delta\varepsilon^{pl} = \delta\lambda$, meaning that the equivalent plastic strain increment is equal to the scalar multiplier, which provides the generalized length of the plastic strain increment.

$$\delta\varepsilon^{pl} \cdot k = \delta w^{pl} = \sigma_{ij}\delta\varepsilon_{ij}^{pl} = \sigma_{ij}\delta\lambda\left(\frac{\partial f}{\partial\sigma_{ij}}\right)_{f-Y=0}$$

Equation 4-19

$$\delta\varepsilon^{pl} \cdot k = \sigma_{ij}\delta\varepsilon_{ij}^{pl} = \delta\lambda f = \delta\lambda \cdot k$$

Equation 4-20

The quantity of strain increment can be determined using Equation 4-21. Since the scalar multiplies is equal to the equivalent plastic strain, it can be rewritten as in Equation 4-22. Additionally, because $f = \sqrt{\frac{3}{2}S_{ij}S_{ij}}$ and $S_{ij} = \sigma_{ij} - \frac{1}{3}(\sigma_x + \sigma_y + \sigma_z)\delta_{ij}$, the equivalent incremental plastic strain is described as Equation 4-23. Therefore, the equivalent plastic strain is shown in Equation 4-24. Consequently, the yield condition using the Von Mises yield criterion with isotropic hardening can be rewritten as Equation 4-25. In addition, because of Equation 4-18, the flow rule can be simplified as Equation 4-26. Here, σ_0 is the initial yield stress.

$$\|\delta\varepsilon\| = \left(\delta\varepsilon_{ij}^{pl}\delta\varepsilon_{ij}^{pl}\right)^{\frac{1}{2}} = \delta\lambda\left(\frac{\partial f}{\partial\sigma_{ij}}\frac{\partial f}{\partial\sigma_{ij}}\right)^{\frac{1}{2}}$$

Equation 4-21

$$\delta\lambda = \delta\varepsilon^{pl} = \frac{\left(\delta\varepsilon_{ij}^{pl}\delta\varepsilon_{ij}^{pl}\right)^{\frac{1}{2}}}{\frac{\partial f}{\partial\sigma_{ij}}\frac{\partial f}{\partial\sigma_{ij}}^{\frac{1}{2}}}$$

Equation 4-22

$$\delta\varepsilon^{pl} = \sqrt{\frac{2}{3}\delta\varepsilon_{ij}^{pl}\delta\varepsilon_{ij}^{pl}}$$

Equation 4-23

$$\varepsilon^{pl} = \int \sqrt{\frac{2}{3}\delta\varepsilon_{ij}^{pl}\delta\varepsilon_{ij}^{pl}}$$

Equation 4-24

$$F(\sigma, \varepsilon^{pl}) = \sqrt{\frac{3}{2}S_{ij}S_{ij}} - k(\varepsilon^{pl}) = 0$$

Equation 4-25

$$\delta\varepsilon_{ij}^{pl} = \delta\varepsilon^{pl}\left(\frac{\partial f}{\partial\sigma_{ij}}\right) = \delta\varepsilon^{pl}\frac{3}{2}\frac{S_{ij}}{\sigma_0}$$

Equation 4-26

Rate-Dependent Isotropic Plasticity Model

Under real fuel cell operating conditions, different frequencies of the start-up and shut-down processes can significantly affect the mechanical response of Nafion material. We discussed the rate-independent plasticity model with isotropic hardening above; however, this model does not include the impact of the strain rate. Therefore, the rate-independent plasticity model needs to be modified into a rate-dependent plasticity model, using Peirce's rate-dependent plasticity model, as shown in Equation 4-27. Here, *m* is the strain rate hardening parameter. γ is the material viscosity parameter and σ_{P0} is the static yield stress. This model, compared with other rate-dependent plasticity model, shows better convergence ability. As a result, the yield condition with the Von Mises yield criterion can be rewritten as Equation 4-28.

$$\sigma_P = \left[1 + \frac{\varepsilon^{pl}}{\gamma}\right]^m \sigma_0$$

Equation 4-27

$$F(\sigma, \varepsilon^{pl}) = \sqrt{\frac{3}{2}S_{ij}S_{ij}} - \left[1 + \frac{\varepsilon^{pl}}{\gamma}\right]^m \sigma_0 = 0$$

Equation 4-28

Flow Channel Plate

The stress-strain relationship contains the material property information, which needs to be evaluated by experiments. According to the experimental data, a graphite flow channel plate has a linear stress-strain relationship, meaning that the amount of stress is proportional to the amount of strain. Hence, it is an elastic material. The mechanical material properties for most common elastic material are defined in terms of three numbers: Young's modulus (modulus of elasticity) E, Poisson's ratio υ, and coefficient of thermal expansion α.

In order to determine the stress-strain relations in the finite element approach, it is helpful to look at the general strain-stress relations. The most general form of the three-dimensional strain-stress relations for elastic materials can be written in the following symbolic matrix form, as shown in Equation 4-29, which is subjected to both mechanical stresses and temperature changes. **C** matrix is named as the compliance matrix, which is related to the material properties. ΔT is the temperature difference in reference to the reference temperature. $\boldsymbol{\alpha}$ is the strains caused by a unit temperature increase. Because the finite element approach requires that the stresses be expressed in terms of the strains and temperature change, it can be rewritten as Equation 4-30.

$$\mathbf{d} = \mathbf{Cf} + \Delta T\boldsymbol{\alpha}$$

Equation 4-29

$$\mathbf{f} = \mathbf{Ed} - \Delta T\mathbf{Ea}$$

Equation 4-30

In addition, a graphite flow channel plate was assumed to be an isotropic material, meaning that it had equal properties in all directions. Because of this characteristic, its stress-strain relation had the following form, as shown in Equation 4-31. G is the shear modulus, $G = \frac{E}{2(1+\vartheta)}$. Equation 4-31 has another form, as presented in Equation 4-32.

$$\begin{bmatrix}\varepsilon_x\\ \varepsilon_y\\ \varepsilon_z\\ \gamma_{yx}\\ \gamma_{zx}\\ \gamma_{yz}\end{bmatrix}=\begin{bmatrix}\frac{1}{E} & -\frac{\vartheta}{E} & -\frac{\vartheta}{E} & 0 & 0 & 0\\ -\frac{\vartheta}{E} & \frac{1}{E} & -\frac{\vartheta}{E} & 0 & 0 & 0\\ -\frac{\vartheta}{E} & -\frac{\vartheta}{E} & \frac{1}{E} & 0 & 0 & 0\\ 0 & 0 & 0 & \frac{2}{G} & 0 & 0\\ 0 & 0 & 0 & 0 & \frac{2}{G} & 0\\ 0 & 0 & 0 & 0 & 0 & \frac{2}{G}\end{bmatrix}\begin{bmatrix}\sigma_x\\ \sigma_x\\ \sigma_x\\ \tau_{yx}\\ \tau_{zx}\\ \tau_{yz}\end{bmatrix}+\alpha\Delta T\begin{bmatrix}1\\1\\1\\0\\0\\0\end{bmatrix}$$

Equation 4-31

$$\begin{bmatrix}\sigma_x\\ \sigma_y\\ \sigma_z\\ \tau_{xy}\\ \tau_{xz}\\ \tau_{yz}\end{bmatrix}=\frac{E}{(1+\vartheta)(1-2\vartheta)}\begin{bmatrix}1-\vartheta & \vartheta & \vartheta & 0 & 0 & 0\\ \vartheta & 1-\vartheta & \vartheta & 0 & 0 & 0\\ \vartheta & \vartheta & 1-\vartheta & 0 & 0 & 0\\ 0 & 0 & 0 & 1-2\vartheta & 0 & 0\\ 0 & 0 & 0 & 0 & 1-2\vartheta & 0\\ 0 & 0 & 0 & 0 & 0 & 1-2\vartheta\end{bmatrix}\begin{bmatrix}\varepsilon_x\\ \varepsilon_y\\ \varepsilon_z\\ \gamma_{xy}\\ \gamma_{xz}\\ \gamma_{yz}\end{bmatrix}$$
$$-\alpha\Delta T\frac{E}{(1+\vartheta)(1-2\vartheta)}\begin{bmatrix}1\\1\\1\\0\\0\\0\end{bmatrix}$$

Equation 4-32

Catalyst Layer

According to the results of the Nano-indentation test, a catalyst layer, composed of Pt/C agglomerates and ionomer, can be described as a linear elastic material. In addition, because ionomer swelling induces strains, catalyst layer's stress-strain relation can be rewritten as Equation 4-33. ΔRH is the relative humidity difference in reference to the reference relative humidity. β is the strains caused by a unit relative humidity increase. Moreover, this stress-strain model also considered the thermal expansion.

$$\begin{bmatrix}\sigma_x\\ \sigma_y\\ \sigma_z\\ \tau_{xy}\\ \tau_{xz}\\ \tau_{yz}\end{bmatrix} = \frac{E}{(1+\vartheta)(1-2\vartheta)}\begin{bmatrix}1-\vartheta & \vartheta & \vartheta & 0 & 0 & 0\\ \vartheta & 1-\vartheta & \vartheta & 0 & 0 & 0\\ \vartheta & \vartheta & 1-\vartheta & 0 & 0 & 0\\ 0 & 0 & 0 & 1-2\vartheta & 0 & 0\\ 0 & 0 & 0 & 0 & 1-2\vartheta & 0\\ 0 & 0 & 0 & 0 & 0 & 1-2\vartheta\end{bmatrix}\begin{bmatrix}\varepsilon_x\\ \varepsilon_y\\ \varepsilon_z\\ \gamma_{xy}\\ \gamma_{xz}\\ \gamma_{yz}\end{bmatrix}$$
$$- \alpha\Delta T\frac{E}{(1+\vartheta)(1-2\vartheta)}\begin{bmatrix}1\\1\\1\\0\\0\\0\end{bmatrix} - \beta\Delta RH\frac{E}{(1+\vartheta)(1-2\vartheta)}\begin{bmatrix}1\\1\\1\\0\\0\\0\end{bmatrix}$$

Equation 4-33

4.1.3.3. Stress-Strain Relationship in an MEA (Contact Condition)

The stress-strain relationships for each cell components of an MEA are discussed in the above section. However, an MEA has a five-layer structure. It is very important to choose an appropriate contact conditions between these layers. Here, the bonded contact condition is selected for the interfacial conditions for these layers because they are tightly connected or glued with each other in the real operation. The bonded condition means that stresses transmit completely on the interfaces. There is no sliding or separation between faces. This type of contact allows for a linear solution since the contact area will not change during the application of the load.

Two layers are in bonded contact means that they do not interpenetrate, and that they can transmit compressive normal forces. Contact compatibility prevents the interpenetration between two contacting bodies. Equation 4-34 shows the contact formulations used to enforce compatibility at the contact interface. F_{normal} is a finite contact force, k_{normal} is a concept of contact stiffness and $x_{penetration}$ is the penetration.

$$F_{normal} = k_{normal}x_{penetration}$$

Equation 4-34

4.1.3.4. Boundary Conditions

The boundary values were given by:

$$u_i = 0$$

on the bottom of the cathode flow channel plate

The symmetric boundary condition was applied on the edge of the channel, as shown in Figure 4-2. Clamping forces were applied on the top of the anode flow channel plate.

$$u_x = 0$$

$$\theta = \frac{1}{2}\left[\frac{\partial u_x}{\partial y} - \frac{\partial u_y}{\partial x}\right] = 0$$

4.1.4. Material Properties of Different Cell Components

4.1.4.1. Graphite Flow Channel Plates and Catalyst Layers

All the components in PEM fuel cells have different material properties, which are listed in Table 4-1. Based on the experimental data, a flow channel plate was treated as a linear elastic material with thermal expansions. According to the nanoindentation testing, a catalyst layer had the same selection. However, it also had both thermal and swelling expansions.

Table 4-1 Material properties of catalyst layers and graphite flow channel plates

Component	β (RH^{-1})	v	E (MPa)	α (K^{-1})
Graphite Flow Channel Plate	---	0.25	10,000	$5*10^{-6}$
Catalyst Layers	Figure 4–3	0.25	450	$123*10^{-6}$

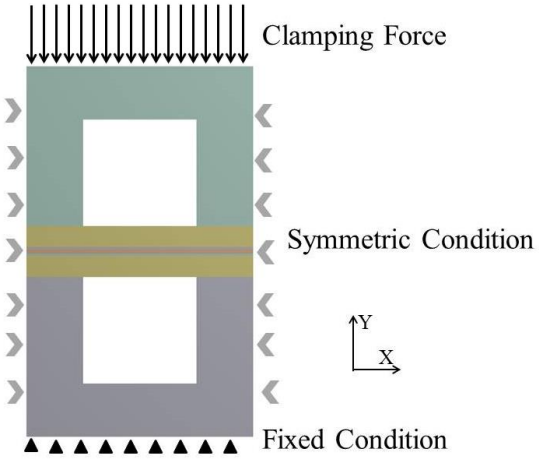

Figure 4-2 Boundary conditions for the structure model

4.1.4.2. Nafion Membrane

The Nafion membrane was treated as a rate-dependent plastic material with isotropic hardening. Its material properties depended on temperatures and humidity, as illustrated in the Table 4-2, Table 4-3 and Table 4-4. These material properties were defined for four different temperatures and relative humidity based on tensile testing. The swelling strains of the Nafion membrane can be obtained from experiments, as shown in Figure 4–3. So far, the rate-dependent parameters for the Nafion membrane cannot be found in the literature. However, because PTFE is the backbone of Nafion membrane, it is reasonable to assume that the viscoplasticity of Nafion membrane is similar to that of the PTFE, whose rate-dependent parameters can be easily obtained from many experiments. In this modelling, the hardening parameter, m, is 0.230, while the viscosity parameter, γ, is 0.0770 [106].

Table 4-2 Material properties of Nafion membrane

Component	β (RH^{-1})	v	E (MPa)	α (K^{-1})
Nafion Membrane	Figure 4–3	0.25	Table 4-3	$123*10^{-6}$

Table 4-3 Young's modulus at various temperatures and humidity for Nafion membrane [93]

Young's Modulus (MPa)	Relative Humidity (%)			
	30	50	70	90
25 ^{o}C	197	192	132	121
45 ^{o}C	161	137	103	70
65 ^{o}C	148	117	92	63
85 ^{o}C	121	85	59	46

Table 4-4 Yield strength at various temperatures and humidity for Nafion membrane [93]

Yield Strength (MPa)	Relative humidity (%) 30	50	70	90
$\boldsymbol{\varepsilon^{pl} = 0}$				
T=25°C	6.76	6.51	5.66	4.20
T=45°C	5.67	5.21	5.01	3.32
T=65°C	5.14	4.58	4.16	2.98
T=85°C	3.61	3.44	3.08	2.20
$\boldsymbol{\varepsilon^{pl} = 0.025}$				
T=25°C	7.16	6.61	6.22	5.11
T=45°C	5.70	5.72	5.43	3.69
T=65°C	5.30	4.77	4.36	3.33
T=85°C	4.16	3.62	3.16	2.26
$\boldsymbol{\varepsilon^{pl} = 0.05}$				
T=25°C	9.71	9.26	8.65	8.88
T=45°C	7.31	7.34	7.48	6.18
T=65°C	6.55	5.92	5.73	5.78
T=85°C	5.04	4.28	4.22	4.31

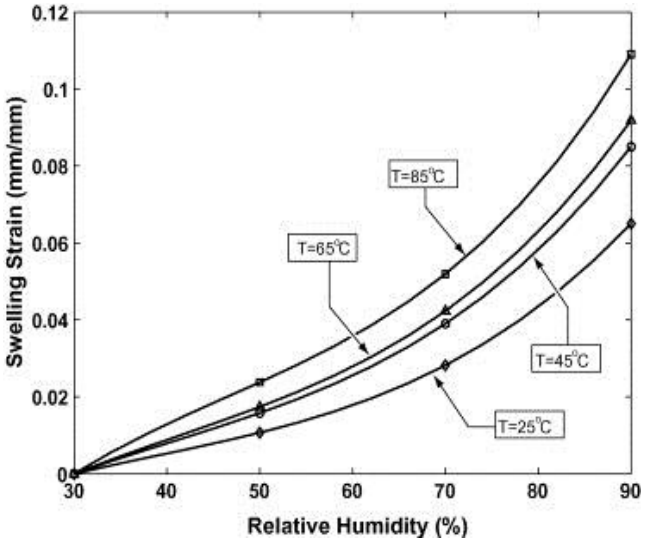

Figure 4-3 Experimental data for dimensional change due to the swelling expansion [93]

4.1.4.3. Gas Diffusion Layers

The compressible hyperelastic Blatz-Ko model was used to describe GDLs' mechanical behaviours in the modelling. This model involves only one coefficient, μ, the initial shear modulus, which needs to be determined. The uniaxial testing provided the stress-strain relationship of GDLs under various compressions. In addition, a GDL was assumed to

have a Poisson ratio as 0.25 [100]. Then, hyperelastic curve fitting, using the experimental data at hand, determined the initial shear modulus.

Since the material is compressible and the GDLs' Poisson ratio is known, the stretch ratio can be rewritten as Equation 4-35. Consequently, the invariants have the following properties, as illustrated in Equation 4-36. In order to derive the relationship between strain energy and the experimental data from uniaxial compression testing, a multiplication with $\frac{\partial \lambda_i}{\partial I_i}$ is used, as shown in Equation 4-37. Consequently, we can obtain a relation between stress and strain, $\sigma_i = f(\lambda_x, \lambda_y)$. For a uniaxial compression testing, Equation 4-38 is valid. Eventually, a correlation between uniaxial stress and strain can be established, $\sigma = f(\lambda)$ with a constant property, μ, needed to be determined. To obtain the initial shear modulus, a curve fit of the expression against the experimental data was required. Normalized error norm, shown in Equation 4-39, was used since it gave equal weight to all of the data points. S is the relative error, whereas σ_E is the experimental stress value.

$$\lambda_z^2 = \frac{1 + \left(\frac{\Delta V}{V}\right)^2}{\lambda_x^2 \lambda_y^2} = \frac{\left(1 + \frac{\Delta L}{L}\right)^{1-2\vartheta}}{\lambda_x^2 \lambda_y^2} = \frac{{\lambda_x}^{1-2\vartheta}}{\lambda_x^2 \lambda_y^2} = \frac{1}{\lambda_x^{1+2\vartheta} \lambda_y^2}$$

Equation 4-35

$$I_2 = \lambda_x^2 \lambda_y^2 + \frac{1}{\lambda_x^{1+2\vartheta}} + \frac{1}{\lambda_x^{2\vartheta-1} \lambda_y^2}$$

$$I_3 = {\lambda_x}^{1-2\vartheta}$$

Equation 4-36

$$\sigma_x = \frac{\partial W}{\partial \lambda_x} = \frac{\partial W}{\partial I_2}\frac{\partial I_2}{\partial \lambda_x} + \frac{\partial W}{\partial I_3}\frac{\partial I_3}{\partial \lambda_x}$$

$$\sigma_y = \frac{\partial W}{\partial \lambda_y} = \frac{\partial W}{\partial I_2}\frac{\partial I_2}{\partial \lambda_y} + \frac{\partial W}{\partial I_3}\frac{\partial I_3}{\partial \lambda_y}$$

Equation 4-37

$$\lambda_x = \lambda, \lambda_y = \lambda^{-\frac{1}{2}-2\vartheta}$$

Equation 4-38

$$S = \sum_{i=1}^{all\ points} \left(1 - \frac{\sigma_A}{\sigma_E}\right)^2$$

Equation 4-39

4.1.5. Numerical Implementation

The PEM fuel cell structure model relied on the commercial software, *ANSYS Multiphysics*, to discretize and solve its equations. The programming language APDL supplied the corresponding coding for swelling expansion model, Blatz-Ko model and Peirce's rate-dependent plasticity model. The Newton-Raphson method was used to solve these equations. All variables followed a strict convergence criterion with a residual of 10^{-8}.

4.1.6. Numerical Procedure

Load-Force Transformation

The internal forces of a structure can be determined directly from the equations of force equilibrium, as shown in Equation 4-40, which yields one matrix equation. **R** is an external load. **A** is a load-force transformation matrix and **f** is an internal force. Load-force transformation is a function of the geometry of the structure only. It describes the relationship between forces in the global and local coordinate system.

$$\mathbf{R} = \mathbf{Af}$$

Equation 4-40

Displacement Transformation Matrix

The calculation of joint displacement involves the following matrix equation, as presented in Equation 4-41. **d** is deformation and **u** is the joint displacement. **B** is the element deformation-displacement transformation matrix, which is a function of the geometry structure. It describes between displacements in the global and local coordinate system.

$$\mathbf{d} = \mathbf{Bu}$$

Equation 4-41

Constitutive Relations

The forces in the elements can be expressed in terms of the deformations in the elements by the following matrix equation, as shown in Equation 4-42. **k** is the element stiffness and **f** is an internal force.

$$\mathbf{f} = \mathbf{ku}$$

Equation 4-42

In structural analysis, the starting point is the joint equilibrium, Equation 4-40. If we substitute element force-deformation equation (constitutive relations), Equation 4-42, the joint equilibrium equation can be written as $\mathbf{R} = \mathbf{Aku}$. Then we substitute Equation 4-41, the general joint equilibrium can be written as $\mathbf{R} = \mathbf{Kd}$, where **K** is the global stiffness matrix.

4.1.7. Grid Independency

In theory, infinitely small grid size results in an exact solution. Hence, increasing the number of mesh seems to be a better approach of improving the accuracy. However, the limitation of computational resources restrains such an idea. For this structure model, grid independency test enabled the study of the mesh size effect on the solution, indicating that the number of grid points along the y-direction, namely the thickness direction, significantly affected the solution.

A large mesh deformation caused the solution difficult to converge when the number of grid points along the y-direction for each layer was smaller than four. Here, solutions with 20 grid points along the y-direction in each layer were assumed to be the standard solutions. Compared with these standard solutions, solutions with 10 grid points along the y-direction in each layer had an error of about 0.26%. Further increasing the number of the grid points significantly increased the computational time; therefore, in this model each layer had 10 grid points in the y-direction. The total number of grid points of the computational domain was 76317.

4.1.8. Comparison with Experimental Data

In order to examine the accuracy of this PEM fuel cell structure model, the GDL's hyperelastic Blatz-Ko model, the Nafion membrane's elastic-plastic model, and the combined structure model for the MEA need to be validated using experimental data. As illustrated in Figure 4-4, Figure 4-5, and Figure 4-6, the experimental compressive behaviours of GDLs, Nafion membranes, and MEAs were generally consistent with the corresponding modelling predictions, which validated the reliability of these three constitutive relations.

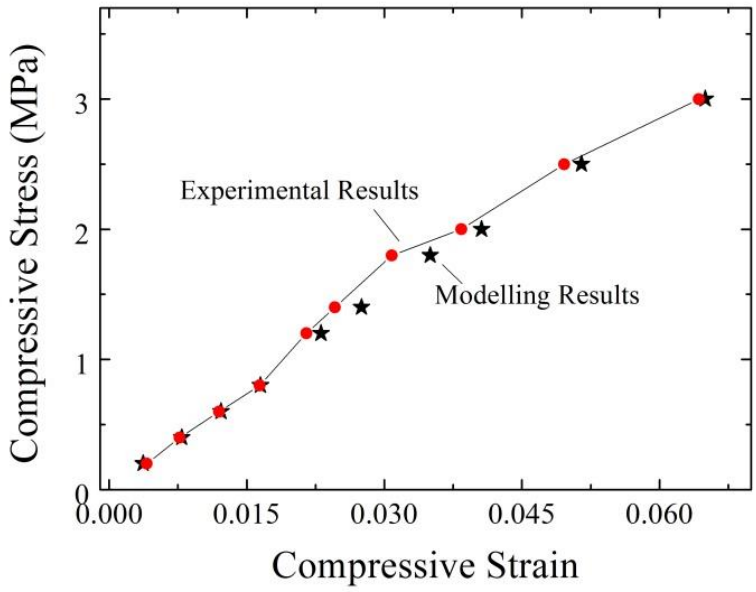

Figure 4-4 Comparison between the Nafion membrane compressive testing and its corresponding modelling results (Temperature: 25^{o}C, Relative Humidity: 30%)

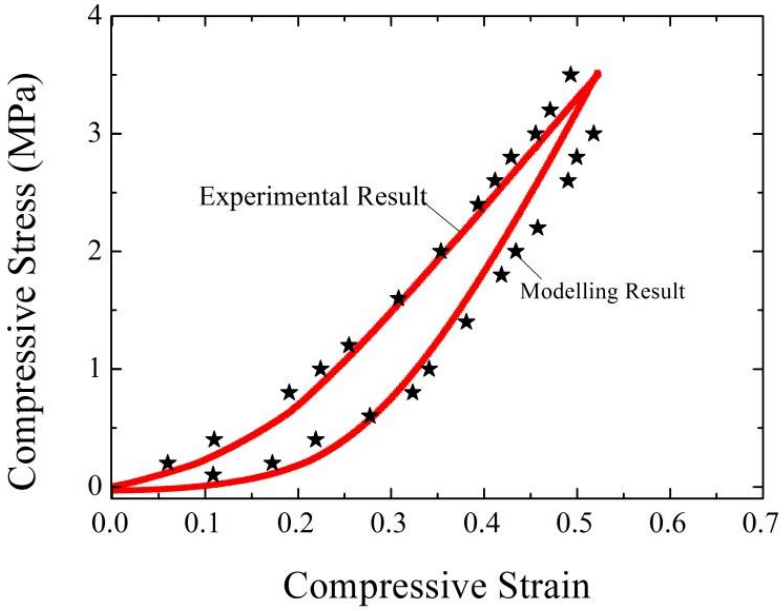

Figure 4-5 Comparison between the GDL compressive testing and its corresponding modelling results (Temperature: 25°C, Relative Humidity: 30%, loading initial shear modulus μ=1.1348*10^{6}Pa, unloading initial shear modulus =9.447*10^{5}Pa)

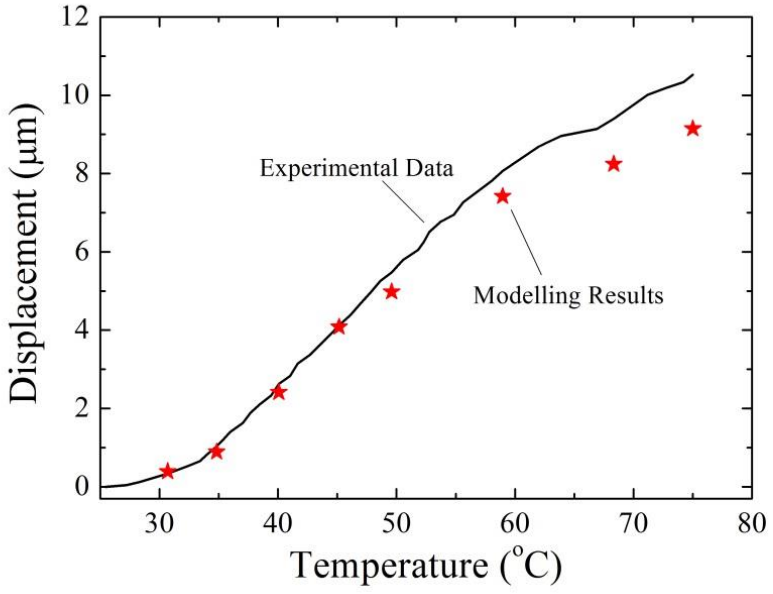

Figure 4-6 Comparison between MEA compressive testing and corresponding modelling results (Relative Humidity: 100%)

4.2. PEM Fuel Cell Performance Model

This comprehensive PEM fuel cell performance model involved electrochemical reaction kinetics, heat generation and transfer, transport of multi-component gas species, multi-water phases, and electrons and protons, and water phase change processes. A PEM fuel cell stack composes different components, including porous and solid materials. Hence, these transport phenomena take place in void volumes, porous and solid materials. Due to the limited computational power, a continuum macroscopic approach, which assumes a homogeneous material of GDLs, catalyst layers and membranes, was used, in order to model transport phenomena in major cell components simultaneously. In a continuum macroscopic approach, a set of conservation equations modeled each transport phenomena. This cell performance model is based on Wu's model [107].

4.2.1. Physical Problem

The computational domain contained a typical single PEM fuel cell channel, as illustrated in Figure 4-1. It included all the essential components, such as two bipolar plates, two single straight flow channels, two GDLs, two catalyst layers, and one Nafion membrane. Humidified hydrogen and oxygen flowed into the anode and cathode channel respectively.

4.2.2. Assumptions

This modelling included the following assumptions:

- The gravity effect was negligible.
- All the reactant gases were ideal gases.
- The flow condition was laminar flow.
- No contaminating gases were considered.
- The membrane was impermeable to all the gases.
- Since the liquid water can be easily removed from straight flow channels, no liquid water existed in the flow channels

4.2.3. Model Formulation

4.2.3.1. Conservation Equations

Several conservation equations, such as mass, momentum, electronic charge, ionic charge, gas species, and liquid water, were formulated for various components of the PEM fuel cell. They are listed below with the various source terms in these equations provided in Table 4-5.

Mass of gas mixture (flow channel, GDL and catalyst layer)

$$\nabla \cdot \left(\epsilon \rho_g \overrightarrow{u_g}\right) = S_m$$

Equation 4-43

Momentum of gas mixture (flow channel, GDL and catalyst layer)

$$\nabla \cdot \left(\epsilon \rho \overrightarrow{u_g}\, \overrightarrow{u_g}\right) = -\epsilon \nabla p_g + \nabla\left(\epsilon \mu \nabla\, \overrightarrow{u_g}\right) + S_u$$

Equation 4-44

Gas species (flow channel, GDL and catalyst layer)

$$\nabla \cdot \left(\rho_g \overrightarrow{u_g} Y_i\right) = \nabla \cdot \left(\rho_g D_i^{eff} \nabla Y_i\right) + S_i$$

Equation 4-45

Liquid water (flow channel, GDL and catalyst layer)

$$\nabla \cdot \left(f \rho_l \overrightarrow{u_g}\right) = \nabla \cdot \left(\rho_l D_l \nabla \emptyset_l\right) + S_l$$

Equation 4-46

Dissolved water (membrane and catalyst layer)

$$0 = \frac{\rho_{mem}}{EW} \nabla \cdot \left(D_d^{eff} \nabla \lambda_d\right) + S_d$$

Equation 4-47

Ionic charge (membrane and catalyst layer)

$$0 = \nabla \cdot \left(k_{ion}^{eff} \nabla \varphi_{ion}\right) + S_{ion}$$

Equation 4-48

Electronic charge (bipolar plate, GDL, catalyst layer)

$$0 = \nabla \cdot \left(k_e^{eff} \nabla \varphi_e\right) + S_e$$

Equation 4-49

Energy (entire cell components)

$$\nabla \cdot \left(\left(\rho C_p\right)_{fl}^{eff} \vec{u} T\right) = \nabla \cdot \left(k_{fl,sl}^{eff} \nabla T\right) + S_T$$

Equation 4-50

Because catalyst layers and GDLs are porous materials, the gas mixture mass, momentum, and species conservation equations listed above are standard conservation equations with porous formulations [108]. In addition, the calculation of the effective porosity of the gas mixture involved the volume fractions of the solid materials, such as GDLs and catalyst layers, and the liquid water. Liquid water was assumed to exist in GDLs and catalyst layers. Its conservation equation was derived based on the capillary pressure in porous media [109]. Dissolved water was considered only for the Nafion-related materials, such as Nafion membranes and catalyst layers. Traditionally, its conservation equation should consist three terms, including diffusion, source and convection terms. However, the convection term was ignored since the convective mass transfer is negligible. The electronic and ionic charge conservation equations consisted of diffusion and source term. The transient term was ignored because the electrochemical double layer charging and discharging was very fast. The energy conservation equation considered all the transport properties in solids, liquids and gases. Table 4-6 shows the source terms for the gas mixtures.

Table 4-5 Source terms in the governing conservation equations

	S_m kg m^{-3}	S_u kg m^{-2}	S_l kg m^{-3}	S_d kmol m^{-3}	S_e A m^{-3}	S_{ion} A m^{-3}	S_T W m^{-3}	S_{pc} W m^{-3}
BP	0	0	0	0	0	0	$\left\|\nabla \varphi_e\right\|^2 k_e^{eff}$	0
Channel	S_v	0	0	0	0	0	0	0
GDL	S_v	$-\frac{\mu_g}{K_g}\overrightarrow{u_g}$	S_{v-l}	0	0	0	$\left\|\nabla \varphi_e\right\|^2 k_e^{eff} + S_{pc}$	$h_{cond} S_{v-l}$
Anode CL	$S_{H_2} + S_v$	$-\frac{\mu_g}{K_g}\overrightarrow{u_g}$	S_{v-l}	$-S_{d-v} + \nabla S_{EOD}$	$-J_a$	J_a	$j_a \lvert \eta_{act} \rvert + \left\|\nabla \varphi_e\right\|^2 k_e^{eff} + \left\|\nabla \varphi_{ion}\right\|^2 k_{ion}^{eff} + S_{pc}$	$h_{cond}\left(S_{v-l} - S_{d-v} M_{H_2O}\right)$

Cathode CL	$S_{O_2} + S_v$	$-\frac{\mu_g}{K_g}\overrightarrow{u_g}$	S_{v-l}	$\frac{j_c}{2F} - S_{d-v} + \nabla S_{EOD}$	J_c	$-J_c$	$-\frac{j_c T \Delta S}{2F} + j_c\lvert\eta_{act}\rvert + \lVert\nabla\varphi_e\rVert^2 k_e^{eff} + \lVert\nabla\varphi_{ion}\rVert^2 k_{ion}^{eff} + S_{pc}$	$h_{cond}(S_{v-l} - S_{d-v}M_{H_2O})$
Membrane	0	0	0	0	0	0	$\lVert\nabla\varphi_{ion}\rVert^2 k_{ion}^{eff} + S_{pc}$	0

Table 4-6 Source terms for the gas mixtures

	S_i	S_v
BP	0	0
Channel	0	$-S_{v-l}$
GDL	0	$-S_{v-l}$
Anode CL	$S_{H_2} = -\frac{j_a}{2F}M_{H_2}$	$-S_{v-l} + S_{d-v}M_{H_2O}$
Cathode CL	$S_{O_2} = -\frac{j_a}{4F}M_{O_2}$	$-S_{v-l} + S_{d-v}M_{H_2O}$
Membrane	0	0

4.2.3.2. Gas Transport Equations

All the gases involved in the model were assumed to be ideal gases. Therefore, the gas mixture density was calculated based on the ideal gas law, as shown in Equation 4-51. p_g is the gas phase pressure. *R* is the universal gas constant. Y_i and M_i are the mass fraction and molecular weight of species *i*, respectively.

$$\rho_g = p_g \left(RT \sum_i \frac{Y_i}{M_i} \right)^{-1}$$

Equation 4-51

Based on the kinetic theory, the dynamic viscosity of the ideal gas mixture can be determined using Equation 4-52 and Equation 4-53. X_i is the mole fraction of species, *i*, while *i* and *j* represent different species. Because parameters change with different temperatures and pressures, their effects need to be considered. Table 4-7 provides some experimental correlations of dynamic viscosity and mass diffusivity under various temperatures and pressures in different species [110,111].

$$\mu_g = \sum_i \frac{X_i \mu_i}{\sum_j X_i \psi_{ij}}$$

Equation 4-52

$$\psi_{ij} = \frac{\left[1 + \left(\frac{\mu_i}{\mu_j}\right)^{0.5} \left(\frac{M_i}{M_j}\right)^{0.25}\right]^{0.5}}{\left[8\left(1 + \frac{M_i}{M_j}\right)\right]^{0.5}}$$

Equation 4-53

Table 4-7 Transport properties [112]

Parameter	Correlation (T in K, P in Pa)	
Hydrogen dynamic viscosity (kg m^{-1}s^{-1})	$\mu_{H_2} = 3.205 \times 10^{-3}(T/293.85)^{1.5}(T+72)^{-1.0}$	
Oxygen dynamic viscosity (kg m^{-1}s^{-1})	$\mu_{O_2} = 8.46 \times 10^{-3}(T/292.25)^{1.5}(T+127)^{-1.0}$	
Water vapour dynamic viscosity (kg m^{-1}s^{-1})	$\mu_v = 7.512 \times 10^{-3}(T/291.15)^{1.5}(T+120)^{-1.0}$	
Liquid water dynamic viscosity (kg m^{-1}s^{-1})	$\mu_l = 2.414 \times 10^{-5} \times 10^{247.8/(T-140)}$	
Hydrogen diffusivities (m^{2}s^{-1})	$D_{H_2} = 1.055 \times 10^{-4}(T/333.15)^{1.5}(101325/p)$	
Oxygen diffusivities (m^{2}s^{-1})	$D_{O_2} = 2.652 \times 10^{-5}(T/333.15)^{1.5}(101325/p)$	
Water vapour diffusivities in anode (m^{2}s^{-1})	$D_v^a = 1.055 \times 10^{-4}(T/333.15)^{1.5}(101325/p)$	
Water vapour diffusivities in cathode (m^{2}s^{-1})	$D_v^c = 2.982 \times 10^{-5}(T/333.15)^{1.5}(101325/p)$	
Specific heat capacities of H_2, O_2, vapour waters and liquid water (J kg^{-1} K^{-1})	$(C_p)_{H_2} = 14283$	$(C_p)_{O_2} = 919.31$
	$(C_p)_{vp} = 2014$	$(C_p)_{lq} = 4182$
Thermal conductivities of H_2, O_2, vapour waters and liquid water (W m^{-1} K^{-1})	$k_{H_2} = 0.1672$	$k_{O_2} = 0.0264$
	$k_{vp} = 0.0261$	$k_{lq} = 0.6$
Entropy change of reaction (J kmol^{-1} K^{-1})	$\Delta S = -163110$	
Latent heat of condensation (J kg^{-1})	$h_{cond} = -2438.5T + 3170700$	

Gas transports are highly associated with the porous condition of the transport media and the liquid water which can block the transport media. Their effects were considered through modifying the gas permeability. Equation 4-54 and Equation 4-55 determined the gas phase and liquid phase permeability, respectively, which depended on the intrinsic permeability of the porous materials and the local volume fraction of the liquid water. Both of them indicated that if the liquid water blocks the pores of GDLs and catalyst layers, the permeability will become zero.

$$K_g = K_0(1 - \emptyset_l)^{4.0}$$

Equation 4-54

$$K_l = K_0\emptyset_l^{4.0}$$

Equation 4-55

The effective mass diffusion coefficient needed to be modified due to the porosity and tortuosity of GDLs and catalyst layers, which was done through the Bruggemann correlation, as shown in Equation 4-56. In this equation, the impact of liquid water on the effective diffusion coefficients was treated the same as the porosity with an exponent of 1.5. D_i^{eff} is the effective mass diffusion coefficient for species, i. When the pore volumes of GDLs and catalyst layers are full of liquid water, the diffusion coefficient will become zero, indicating the water flooding.

$$D_i^{eff} = D_i\epsilon^{1.5}(1 - \emptyset_l)^{1.5}$$

Equation 4-56

4.2.3.3. Water Transport Equations

In this modelling, the liquid water was assumed to have a constant density under different temperatures because the changes of its density within the fuel cell operating temperatures were negligible. The interfacial drag coefficient was calculated using Equation 4-57 [110]. The liquid water dynamics viscosity was associated with the temperature changes.

$$f = \frac{K_l\mu_g}{K_g\mu_l}$$

Equation 4-57

The capillary diffusion coefficients of liquid water in GDLs and catalyst layers were defined by Equation 4-58, where the effect of capillary pressure was considered [113]. The capillary pressure was determined using the Leverett function, as shown in Equation 4-59, where it was a function of the liquid water volume fraction [114,115]. θ is the static contact angle, which relies on the wettability of GDL and CL surface. σ is the surface

tension coefficient between liquid water and gas mixture, whose experimental correlation is temperature dependent, as shown in the following, Equation 4-60 [116].

$$D_l = -\frac{K_l}{\mu_l}\frac{dp_c}{d\phi_l}$$

Equation 4-58

$$p_c = \begin{cases} \sigma\cos\theta\left(\frac{\epsilon}{K_0}\right)^{0.5}[1.417(1-\phi_l) - 2.12(1-\phi_l)^2 + 1.26(1-\phi_l)^3], & \theta_c < 90^o \\ \sigma\cos\theta\left(\frac{\epsilon}{K_0}\right)^{0.5}\left[1.417\phi_l - 2.12{\phi_l}^2 + 1.26{\phi_l}^3\right], & \theta_c > 90^o \end{cases}$$

Equation 4-59

$$\sigma = -0.0001676T + 0.1218 \quad 273.15\text{K} \le T \le 373.15\text{K}$$

Equation 4-60

The liquid phase pressure was calculated based on the capillary pressure and gas phase pressure, as illustrated in Equation 4-61. The liquid phase velocity was calculated based on the liquid phase pressure as shown in Equation 4-62 [117]. Table 4-8 shows the water phase change functions.

$$p_l = p_g - p_c$$

Equation 4-61

$$\overrightarrow{u_l} = -\frac{K_l}{\mu_l}\nabla p_l$$

Equation 4-62

Table 4-8 Correlations related to water phase change

Vapour and liquid water	$S_{v-l} = \begin{cases} \gamma_{cond}\varepsilon(1-\phi_l)\frac{(p_v - p_{sat})}{RT} & p_v > p_{sat} \\ \gamma_{evap}\varepsilon\phi_l\frac{(p_v - p_{sat})}{RT} & p_v < p_{sat} \end{cases}$
Dissolved water and vapour	$S_{d-v} = \zeta_{d-v}\frac{\rho}{EW}(\lambda_d - \lambda_{equil})(1-\phi_l)$
Saturation pressure [118]	$\log_{10} p_{sat} = -2.1794 + 0.02953(T-273.15) - 9.1837 \times 10^{-5}(T-273.15)^2 + 1.4454 \times 10^{-7}(T-273.15)^3$

During a normal PEM fuel cell operation, an electrochemistry reaction produces dissolved water. Then, vapour water, liquid water and dissolved water co-exist on the catalyst layer surface [113]. Therefore, the dissolved water content needs to be considered, which was calculated using Equation 4-63. *EW* is the equivalent weight of membrane. ρ_{mem} is the density of the dry membrane.

$$\lambda_d = \frac{EW}{\rho_{mem}} C_{H_2O}$$

Equation 4-63

The different distribution of water content in the membrane resulted in the membrane water diffusion. Then, the diffusivity of dissolved water could be determined using Equation 4-64. In addition, the equilibrium dissolved water content was calculated using Equation 4-65. As shown in Equation 4-66, *a* is the water activity.

$$D_d = \begin{cases} 3.1 \times 10^{-7} \lambda_d [\exp(0.28\lambda_d) - 1] \exp\left(\frac{-2346}{T}\right), & 0 < \lambda_d < 3 \\ 4.17 \times 10^{-8} \lambda_d [161\exp(-\lambda_d) + 1] \exp\left(\frac{-2346}{T}\right), & 3 < \lambda_d < 17 \end{cases}$$

Equation 4-64

$$\lambda_{equil} = \begin{cases} 0.043 + 17.81a - 39.85a^2 + 36.0a^3, & 0 \le a \le 1 \\ 14.0 + 14(a-1), & 1 \le a \le 3 \end{cases}$$

Equation 4-65

$$a = \frac{X_u p_g}{p_{sat}} + 2\phi_l$$

Equation 4-66

In order to study the impact of the electro-osmic drag on the water transport, source term, S_{EOD} was introduced into the membrane water conservation equation, as shown in Equation 4-67. The EOD coefficient is the number of water molecules dragged per hydrogen ion moved through the ionomer, as calculated in Equation 4-68 [118].

$$S_{EOD} = \nabla \cdot \left(\frac{n_d}{F} k_{ion}^{eff} \nabla \varphi_{ion} \right)$$

Equation 4-67

$$n_d = \frac{2.5 \lambda_d}{22}$$

Equation 4-68

4.2.3.4. Electron and Ion Transport Equation

The proton conductivity of the Nafion membrane was calculated using Equation 4-69 [118]. Since GDLs and catalyst layers are porous materials, its proton and electron conductivity calculations involved some modifications with the original Bruggemann correlation. As shown in Equation 4-70 and Equation 4-71, the porosities of the catalyst layers and GDLs, and the ionomer volume fraction in the catalyst layers were considered in the correlation. An exponent of 1.5 was used in this correlation. This coupled model considered the effect of pressure on the interfacial electron conductivity between GDLs and flow channel plates, as illustrated in Figure 4-7. In addition, the interfacial conductivity between GDLs and catalyst layers was ignored because the catalyst layer was a very thin layer.

$$k_{ion} = (0.5139 \lambda_d - 0.326) \exp\left[1268 \left(\frac{1}{303.15} - \frac{1}{T} \right)\right]$$

Equation 4-69

$$k_e^{eff} = (1 - \epsilon - \omega)^{1.5} k_e$$

Equation 4-70

$$k_{ion}^{eff} = \omega^{1.5} k_{ion}$$

Equation 4-71

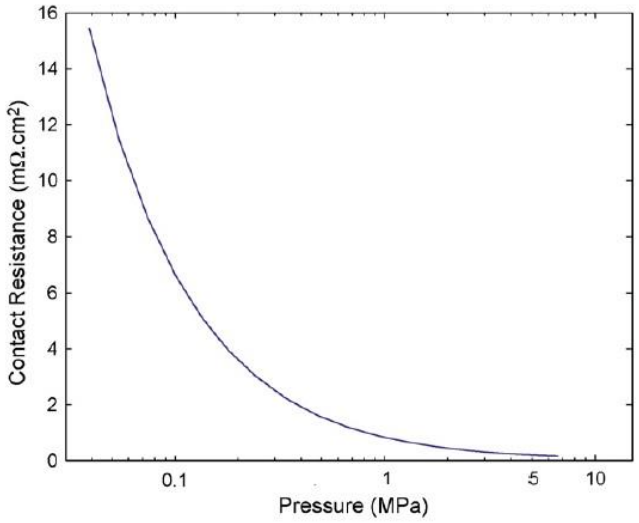

Figure 4-7 The effect of pressure on the contact resistance [119]

The reaction rates in the anode and cathode catalyst layers were calculated using the classical Butler-Volmer equations, as illustrated in Equation 4-72 and Equation 4-73. *F* is the Faraday's constant and *C* is the concentration. Table 4-9 shows the correlations and values of the parameters related to the electrochemical reactions.

$$j_a = (1-\phi_l) j_{0,a}^{ref} \left(\frac{C_{H_2}}{C_{H_2}^{ref}}\right)^{0.5} \left[\exp\left(\frac{2F\alpha_a}{RT}\eta_{act}\right) - \exp\left(-\frac{2F\alpha_c}{RT}\eta_{act}\right)\right]$$

Equation 4-72

$$j_c = (1-\phi_l) j_{0,c}^{ref} \left(\frac{C_{O_2}}{C_{O_2}^{ref}}\right)^{0.5} \left[-\exp\left(\frac{4F\alpha_a}{RT}\eta_{act}\right) - \exp\left(-\frac{4F\alpha_c}{RT}\eta_{act}\right)\right]$$

Equation 4-73

Table 4-9 Parameters related to electrochemical reactions [112]

Parameter	Correlation
Overpotential (V)	$\eta_{act} = \phi_{ele} - \phi_{ion}$
Transfer coefficient	$\alpha_a = \alpha_c = 0.5$
Volumetric reference exchange current density in anode (A m^{-3})	$j_{0,a}^{ref} = j_{0,a}^{ref}\big\|_{353.15K} \exp\left[-1400\left(\frac{1}{T} - \frac{1}{353.15}\right)\right]$
Volumetric reference exchange current density in cathode (A m^{-3})	$j_{0,c}^{ref} = j_{0,c}^{ref}\big\|_{353.15K} \exp\left[-7900\left(\frac{1}{T} - \frac{1}{353.15}\right)\right]$

4.2.3.5. Energy Transport Equation

The effective volumetric heat capacities in the energy conservation equation were calculated using Equation 4-74 and Equation 4-75. $(C_p)_g$ is the specific heat capacity of the gas mixture, which was calculated using Equation 4-76. $(C_p)_{sld}$ is the specific heats of the electron conducting materials in catalyst layers and all solid materials in GDLs and bipolar plates. The effective thermal conductivity in the energy conservation equation was calculated as a volume averaged value, as shown in Equation 4-77, Equation 4-78 and Equation 4-79. Since the effect of temperatures on the specific heat capacity and thermal conductivity is insignificant under the range from 0-100^{o}C, both of them were considered as constant in the modelling [111].

$$(\rho C_p)_{fl,sl}^{eff} = \epsilon\left[\emptyset_l\rho_l(C_p)_l + (1-\emptyset_l)\rho_g(C_p)_g\right] + (1-\epsilon-\omega)\rho_{sld}(C_p)_{sld} + \omega\rho_{mem}(C_p)_{mem}$$

Equation 4-74

$$(\rho C_p)_{fl}^{eff} = \epsilon\left[\emptyset_l\rho_l(C_p)_l\frac{K_l\mu_g}{K_g\mu_l} + (1-\emptyset_l)\rho_g(C_p)_g\right]$$

Equation 4-75

$$(C_p)_g = \sum_i Y_i(C_p)_i$$

Equation 4-76

$$k_{fl,sl}^{eff} = \epsilon[\emptyset_l k_l + (1-\emptyset_l)k_g] + (1-\epsilon-\omega)k_{sld} + \omega k_{mem}$$

Equation 4-77

$$k_g = \sum_i \frac{X_i k_i}{\sum_j X_i\psi_{ij}}$$

Equation 4-78

$$\psi_{ij} = \frac{\left[1 + \left(\frac{k_i}{k_j}\right)^{0.5} \left(\frac{M_i}{M_j}\right)^{0.25}\right]^{0.5}}{\left[8\left(1 + \frac{M_i}{M_j}\right)\right]^{0.5}}$$

Equation 4-79

4.2.3.6. Boundary and Initial Conditions

The boundary conditions in this modeling included the inlet reactant flow conditions, operating temperatures, operating pressures and electric loads. The inlet mass flow rates were defined using Equation 4-80, while the species concentrations at the inlets were shown in Equation 4-81. ξ_a and ξ_c are the stoichiometry ratios for the anode and cathode respectively. A is the cell active area. ρ_g^a and ρ_g^c are the anode and cathode inlet gas density, respectively. I_{ref} is the reference current density. A constant pressure was specified at the outlets of the flow channel. A constant temperature was defined at the anode, cathode flow channel inlets and the surrounding walls. The liquid water volume fraction was set at zero for the flow channels because the liquid water was assumed to be removed out of the channel quickly.

$$\dot{m}_a = \frac{\rho_g^a \xi_a I_{ref} A}{2F c_{H_2}} \qquad \dot{m}_c = \frac{\rho_g^c \xi_c I_{ref} A}{4F c_{O_2}}$$

Equation 4-80

$$c_{H_2} = \frac{\left(p_g^a - RH_a p_{sat}\right)}{RT_{in}^a} \qquad c_{O_2} = \frac{0.21\left(p_g^c - RH_c p_{sat}\right)}{RT_{in}^c}$$

Equation 4-81

4.2.3.7. Cell Voltage Correlations.

Cell voltages and current densities were characterized using Equation 4-82. The electronic potential at the bottom surfaces of the cathode bipolar plate was set as zero, while the electronic potential at the top surface of the anode bipolar plate was the difference between the reversible and operating cell voltages. The reversible cell voltage was determined using Equation 4-83.

$$\begin{cases} \phi_e^{a,end} = V_{rev} - V_{cell} = \eta_{total} \\ \phi_e^{c,end} = 0 \end{cases}$$

Equation 4-82

$$V_{rev} = 1.229 - 0.9 \times 10^{-3}(T_0 - 298) + \frac{RT_0}{2F}\left(\ln P_{H_2}^{\text{in}} + \frac{1}{2}\ln P_{O_2}^{\text{in}}\right)$$

Equation 4-83

4.2.4. Numerical Procedures

The PEM fuel cell performance model relied on commercial software, *FLUENT 6.3*, to discretize and solve its conservation equations. The programming language C imported these equation models into *FLUENT* according to the user defined functions (UDFs) because this commercial software merely provided the gas mass, momentum and species and energy conservation equations. UDFs also supplied the corresponding coding for various source terms, model parameters, material property correlations, boundary conditions and relaxation stabilization schemes. The pressure-based segregated solver offered the sequential solutions for the individual variables of the conservation equations. Here, each conservation equation was segregated from the other equations. A pressure correction equation helped to achieve the constraint of the gas mass conservation on the gas velocity field. The SIMPLE algorithm was used to solve these equations. An algebraic multi-grid (AMG) method with a Gauss-Seidel type smoother increased the efficiency of the convergence. All variables followed a strict convergence criterion with a residual of 10^{-8}. The following loops described the main procedure for each iteration:

1. Define the initial condition for the first iteration
2. Update the temperature- and pressure- based properties according to the current solution
3. Solve the momentum equations separately
4. Solve the pressure correction equation using the values obtained from step 3
5. Solve the rest of the conservation equations
6. Check for the convergence of the equations. If not meet the convergence criterion, start again from step 2

4.2.5. Grid Independency

The selection of the grid point number involved the consideration of computational time and the convergence process. Ideally, a large number of grid points helps to achieve a more accurate result. However, they also consume more computational resources. Hence, the goal of this grid independency study aimed to find an optimal grid size. In this three dimensional cell performance model, the length of the flow channel and the number of parallel flow channel determined the number of grid points along the X-, Z- direction, respectively. Different MEA components had the same number of grid points along the thickness direction.

A grid independency study probed the grid size on three directions, which indicated that the number of grid points along the y-direction significantly affected the solutions. In order to study the effect of grid number along the thickness direction, the number of grid points along the X- and Z- directions was fixed at 100 and 20 in a typical single PEM fuel cell channel with a channel length of 90 mm and channel width of 1 mm. A cell current density is one of the essential parameters of cell performance, which changes with the number of grids. Therefore, the following grid independence study clarified its relation with various grid sizes.

The results showed that less than six grids along the thickness direction made the solution difficult to converge, whereas more than twenty grids had a similar problem, which might result from a high aspect ratio of the computational cells. The result with twenty grids on the Y-direction was assumed to be the standard solution. Ten grid points in each component of an MEA contributed to an error of about 1%. Therefore, ten grid points were the selection of this modelling since further increasing the grid number not only elongated the computational time, but also impaired the convergence.

4.3. Cell Structure-Performance Coupled Model

4.3.1. Physical model

The cell structure-performance coupled model considers the effect of MEA's deformation on cell performance. The structure model quantifies the deformations of an MEA, as shown in Figure 4-8.

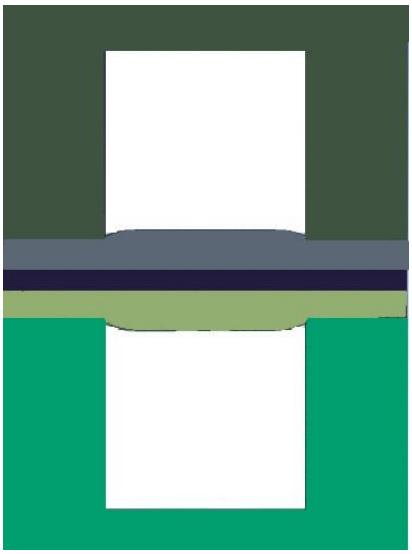

Figure 4-8 A schematic drawing of a single PEM fuel cell channel with deformation

4.3.2. Model Coupling (Effective Transport Property)

The assembly procedure, operation conditions and material degradation resulted in cell component deformations which changed the porosity, and more importantly, the effective transport properties in GDLs and catalyst layers, as discussed in the cell performance modelling. Equation 4-84 described the porosity change of GDLs with deformations [112]. Equation 4-85 shows the relation between the intrinsic permeability of porous materials and its porosity [120]. This model considered the overall changes in porosity, instead of the changes at discrete locations in a GDL.

$$\epsilon = 1 - (1 - \epsilon_0)\frac{\delta_0}{\delta_d}$$

Equation 4-84

$$K_0 = \frac{\epsilon(\epsilon - 0.037)^{2.661} d_f^2}{8(\ln \epsilon)^2 0.975(1.661\epsilon - 0.0037)^2}$$

Equation 4-85

4.3.3. Numerical Implementation

Cell structure-performance coupled analyses provide more realistic results of cell performance with a deformed cell structure under various operating conditions, although such analyses are more computationally intensive. This modelling depended on ANSYS Workbench which has a wide application in multiphysics coupling. The system coupling participants were a static structure and a steady fluid flow. The solution to two-way structure-performance interaction required co-simulation between computational fluid dynamics and structural mechanics, which consisted of three main procedures.

1) The cell performance model, based on an intact single PEM fuel cell structure, determined the distributions of temperatures, relative humidity and pressures under a designed cell operating condition.
2) The mapping technique assigned the temperature, relative humidity and pressure distributions, obtained from the first step, to the corresponding nodes of the structure model. This structure model used these distributions as loading conditions and ran the model, which then characterized the deformation of the MEA and the flow channel plate. In addition, MEAs' deformation is associated with the transport parameters of GDLs and catalyst layers. It enabled the determination of the corresponding changes in porosity, permeability, diffusivity and conductivity of GDLs and catalyst layers.
3) The cell performance model then used the deformed cell structure to calculate the cell performance with a designed operating condition. In addition, the porosity, permeability, diffusivity, intrinsic and interfacial conductivity were updated with the operating condition.

4.3.4. Comparison with Experimental Data

The comparison of experimental measurements and the model predictions validated the reliability of the cell performance-structure coupled model. The model parameters were

adjusted according to the experimental conditions to obtain agreement with the experimental data. As presented in Figure 4-9, the model predictions agree with the experimental data.

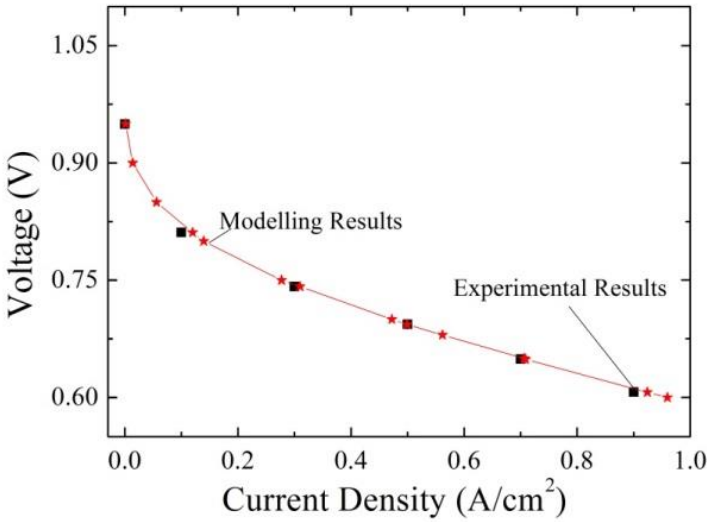

Figure 4-9 Comparison between cell performance model predictions and experimental data (Inlet Temperature: 75°C, Relative Humidity: 100%, Clamping Force: 0.4MPa)

4.4. Summary

This chapter explains the fuel cell structure model, the performance model and the structure-performance coupled model. Corresponding experiments validated the reliability of these two models. In addition, this chapter clarifies the required steps to couple the structure and performance models.

In the structure model, a variety of constitutive models enabled the simulation of different materials in cells. In particular, a rate-dependent isotropic plasticity model with temperature- and humidity-dependent material properties modeled the viscoplasticity of the Nafion membrane. In addition, a hyperelasticity material model simulated GDLs' different loading and unloading compressive behaviours. Further, a traditional elastic model determined the linear mechanical behaviour of catalyst layers and graphite flow channel plates. The experimental compressive behaviours of GDLs, Nafion membranes,

and MEAs were generally consistent with the corresponding modelling predictions, which validated the reliability of these three constitutive relations.

The cell performance involved electrochemical reaction kinetics, heat generation and transfer, transport of multi-component gas species, multi-water phases, and electrons and protons, and water phase change processes. It considered the effects of porosity, permeability, diffusivity, thermal and electron conductivity on cell performance, which enabled its coupling with the structure model.

The structure-performance coupled model, on one hand, accounted for the effects of deformation on the cell performance. On the other hand, it also studied the impact of working conditions, which are associated with cell performance, on the MEA's deformation. Therefore, it provided a more realistic method to study the mechanical impact on cell performance. In addition, the experimental results were consistent with the corresponding modelling predictions.

Chapter 5

Microstructures in MEAs and Their Changes

The durability of a PEM fuel cell is associated with the microstructures and their changes in MEAs. In this chapter, a scanning electron microscope detailed the original microstructures of different components in MEAs as well as their changes after an accelerated durability test. The comparison of the microstructures in original and used MEAs shed light on the mechanism behind these structural changes.

5.1. Stress Distributions in the Fuel Cell Assembly

Stress distributions are crucial for studying the morphological defects in MEAs, since inappropriate stresses could possibly result in the microstructural changes. The pressure-indicating film provided the stress distribution measurement in the fuel cell assembly, as shown in Figure 5-1. The film measured the normal stress distribution on the GDL and the catalyst layer, so that it rested either between the flow distribution plate and the GDL or between the GDL and the catalyst layer.

The measured stress distribution had variations corresponding to the periodicity of the flow channels, as presented in Figure 5-1. The stress at the edge of the MEA was larger than that at the center of the MEA. The maximum normal stress at the edge was about 1.5 MPa, while it was about 1.0 MPa at the center on the GDL surface. This difference is understandable because the bolts and nuts located around the edge of the active area. Another contributing factor is size difference between the endplate (210.25 cm^2) and the graphite flow channel plate (110.25 cm^2). When the assembly force was applied through each bolt, the endplate tended to bulge, leading to a non-uniform stress distribution. This non-uniform distribution can cause the reactants, water, heat and electron to transfer in a non-uniform way, in turn resulting in the non-uniform distributions of temperature and water content in the cell. As illustrated in Figure 5-2, the stress distribution on the catalyst layer surface was more uniform than that on the GDL surface, since GDLs worked as a cushion on the catalyst layer.

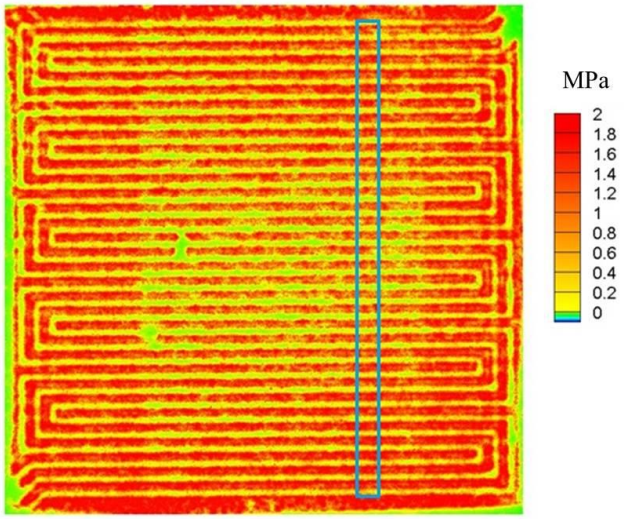

Figure 5-1 Longitudinal normal stress distributions on the GDL surface

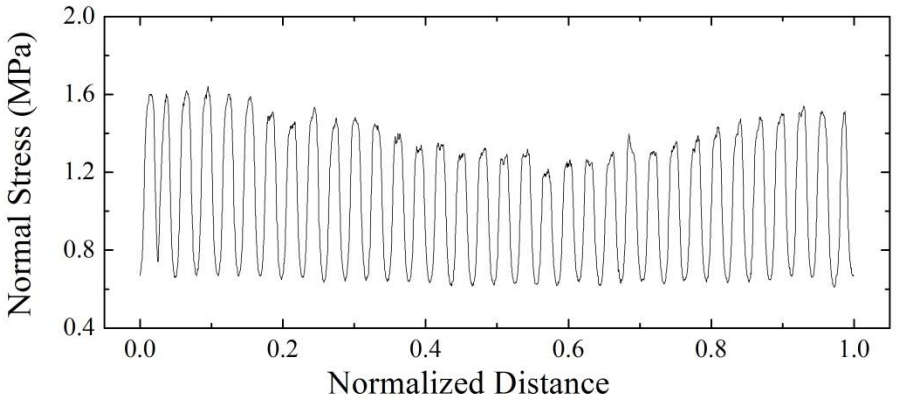

Figure 5-2 Longitudinal normal stress distributions on the catalyst layer surface

5.2. Microstructures of New CCMs and GDLs

Figure 5-3 and Figure 5-4 illustrate the surface and cross sectional view of a new Nafion117-based CCM. Due to the differences in electron densities, various elements show distinct intensities of colour in SEM images. Based on the colour intensity, the catalyst layer had a highly porous structure characterized by fairly evenly distributed pores, represented as the dark spots, on a roughened surface. However, the dimensions of the pores were not the same. Micro-cracks existed in the catalyst layer, as shown in the circles. They could deteriorate cell performance because excess water can stay in the cracks and block the reaction site. At present, the sizes of these cracks were small; however, they could develop into large ones under large assembly forces and thermal-hygro stresses during operations. This possible development could further reduce cell performance.

The cross sectional images shown in Figure 5-4 and Figure 5-5 indicates that the two thin catalyst layers were in a close contact with the membrane. The thicknesses of the catalyst layers and the membrane were quite uniform. The catalyst layer was about 10μm thick, while the membrane was about 138 μm thick. Compared to the porous structure of the catalyst layers, the membrane was denser and its surface was smoother. Figure 5-6 provides a higher magnified image about the catalyst layer morphology. The catalyst layer was a collection of agglomerates with varying sizes. The aggregation of these

agglomerates formed the networks of pores. Reactant gases flow into the reaction site through this network.

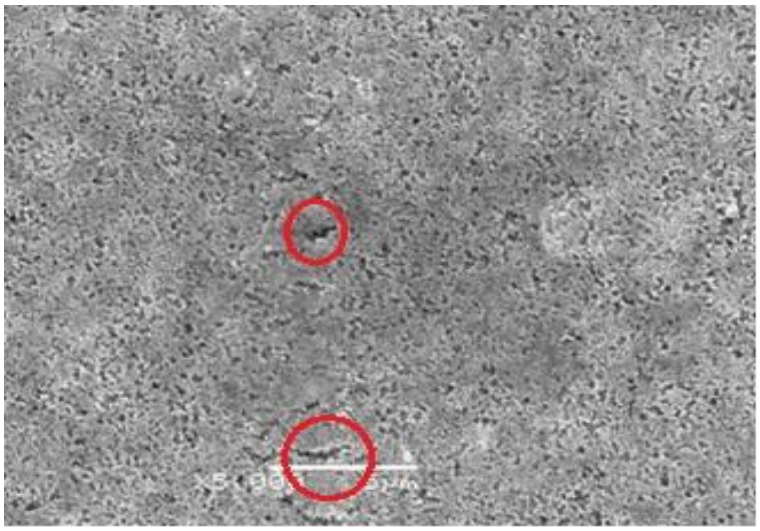

Figure 5-3 A face view of a catalyst layer at 5000* magnification

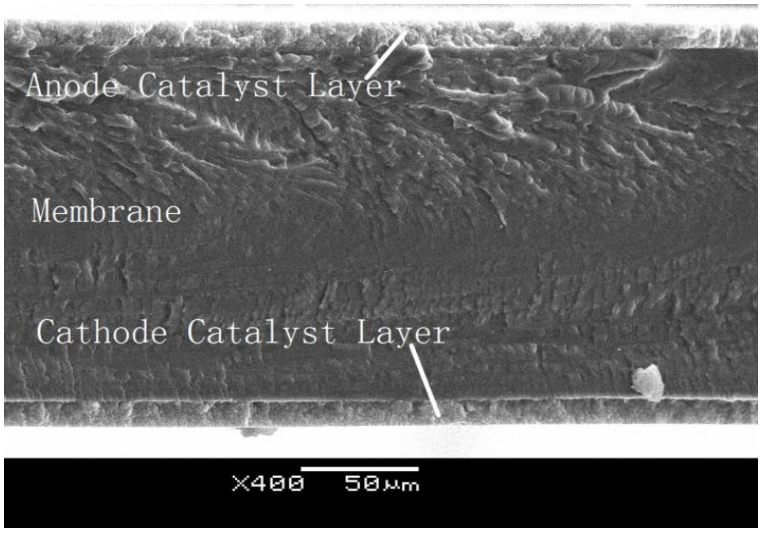

Figure 5-4 A cross sectional view of a CCM at 400* magnification

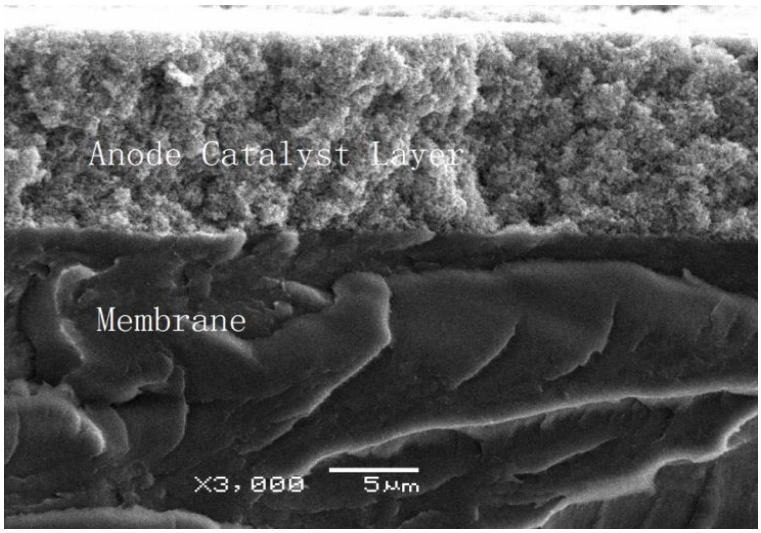

Figure 5-5 A cross sectional view of a CCM at 3000* magnification

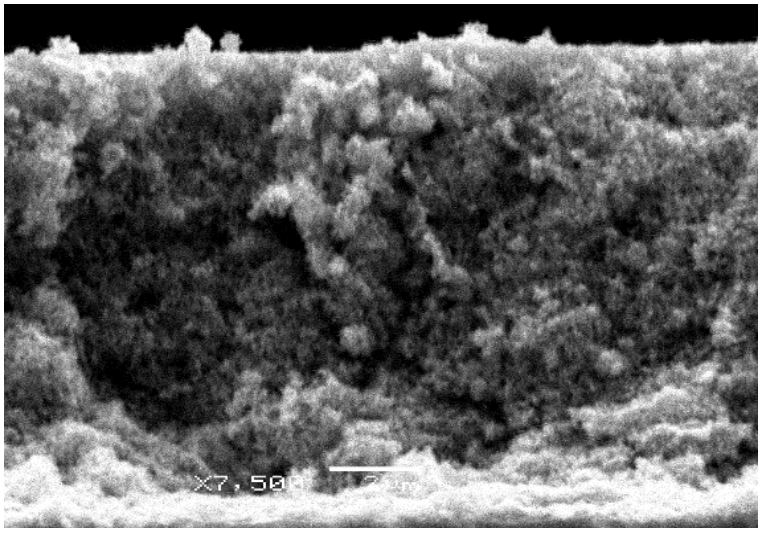

Figure 5-6 A cross sectional view of a catalyst layer at 7500* magnification

In most tested samples, catalyst layers and Nafion membranes were connected closely. However, some new CCM samples witnessed the delamination between the catalyst layer and the Nafion membrane, as shown in Figure 5-7. The separation of catalyst layers and membranes is one of the most common defects in MEAs, which can cause a series of issues, including water flooding, hot spot and catalyst loss. Therefore, it is important to discuss in detail this structural change.

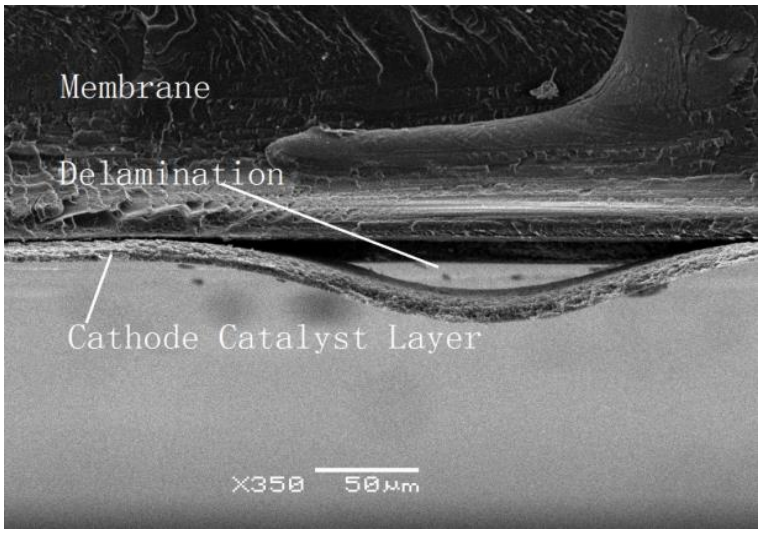

Figure 5-7 Delamination in a new CCM at 350* magnification

At the edge of the layer in Figure 5-7, the catalyst layer was still connected with the polymer membrane; however, the connection between them was poor as indicated by some fissures around the connection. At approximately 400 μm away from the delamination starting point, the catalyst layer was totally separated from the Nafion membrane. The separation was about 25 μm. Unlike the catalyst layer, the polymer membrane can still keep its original shape while the catalyst layer deformed into a bow shape. This deformation can result in many issues. For example, excess water can stay in the void space formed by the membrane and deformed catalyst layer, which blocks the proton transport path for reaction sites and thereby reduces the proton conductivity and cell performance. Consequently, the temperature at this region was higher than other locations, leading to a heat spot.

In addition, a catalyst layer, coated on the Nafion membrane, is very fragile due to its porous structure. During cell operations or cell assembly processes, the catalyst layers around this delamination can easily flake off. A high resolution image, shown in Figure 5-8, indicates that the delamination did not change the texture of the catalyst layer. Pores and agglomerations still existed. The observed delamination in new CCMs was most likely caused by the fabrication process, where inappropriate working temperatures, relative humidity, spray approaches, and the unnecessary bending of membranes can contribute to this defect.

Furthermore, the catalyst layer and the Nafion membrane underwent an energy-dispersive spectroscopy (EDS) test, an analytical technique used for elemental analysis of a sample. Its fundamental principle is that each element has a unique atomic structure, allowing a unique set of peaks on its X-ray spectrum. Based on this unique peak, the type of an element can be determined. The test was carried out at three different locations, as shown in Figure 5-9.

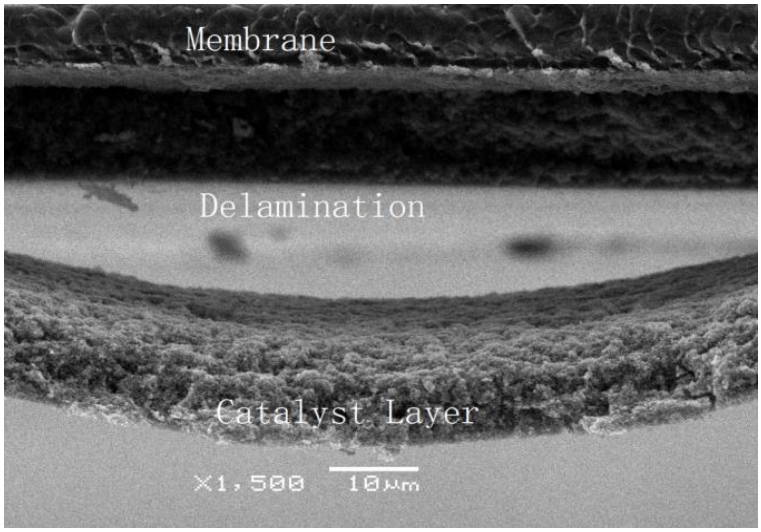

Figure 5-8 Delamination in a new CCM at 1500* magnification

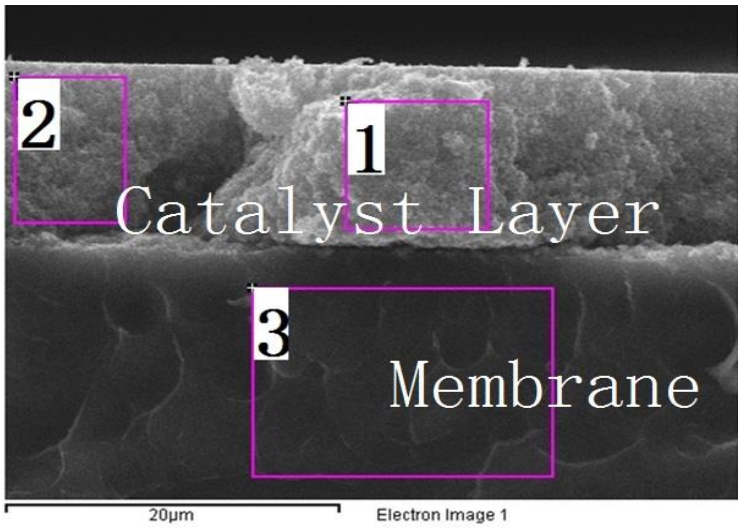

Figure 5-9 Associated EDS test spots on the catalyst layer and the membrane

Test #3 was at the membrane region, while tests #1 and #2 were at the catalyst layer regions. As illustrated in Table 5-1 , the catalyst layer mainly contained carbon, fluorine and platinum although the element compositions at different regions of the catalyst layer were slightly different. Compared with region #2, the Pt composition at region #1 was relatively lower (#2: 34.37%; #1: 30.8%). The Nafion membrane was composed of carbon, fluorine, oxygen and sulphur. The concentration of fluorine was the highest among the four elements.

Table 5-1 EDS results on the catalyst layer and the membrane

spectrum	C	error	O	error	F	error	S	error	Pt	error	Total
1	45.87	8.08%	---	---	23.33	6.63%	---	---	30.80	6.78%	100%
2	48.10	10.09%	---	---	17.52	7.99%	---	---	34.37	8.99%	100%
3	30.68	7.63%	2.77	8.20%	63.11	6.18%	3.44	1.31%	---	---	100%

A GDL, as a highly porous material, consists of numerous carbon fibres, which connect with each other in a random manner to form a thin layer. Hence, it has a unique structure. Such a structure becomes more complicated when the GDL is coated with PTFE. Figure 5-10 and Figure 5-11 illustrates the carbon fibre in two kinds of GDLs, a raw GDL without PTFE treatment and a PTFE-coated GDL. Each carbon fibre can be clearly observed in a raw GDL without PTFE coating. Average diameters of these fibres were about 10 μm. The networks of pores were formed by the irregular connections between different carbon fibres. On the other hand, in a PTFE-coated GDL, carbon fibres were wrapped with coatings. As shown in Figure 5-11, the coating looks like debris accumulated on the fibre surface. Due to the coating, the overall diameters of these fibres were larger than those in a raw GDL; therefore, the PTFE-coated GDL had a smaller pore volume compared with the raw GDL. It has been proposed that the in-plane and through-plane mass transfer resistances are dependent on the microstructure of the GDL. Therefore, this reduced pore volume in a PTFE-treated GDL might introduce a larger resistance in mass transfer.

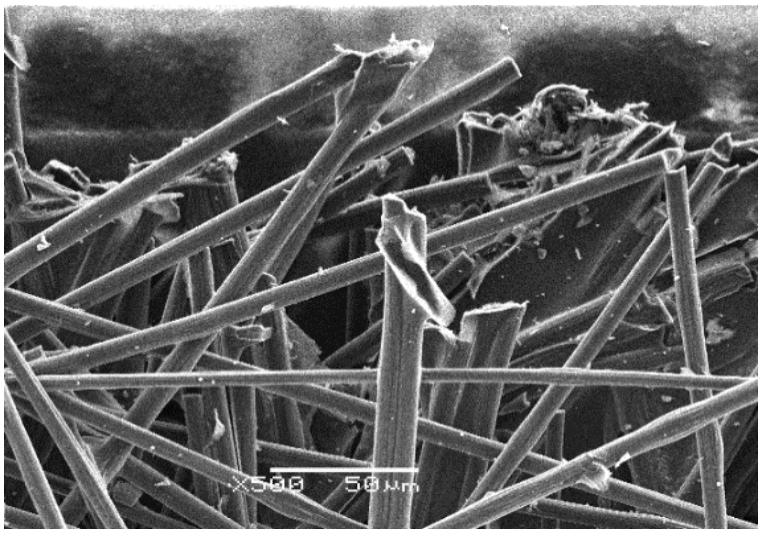

Figure 5-10 Carbon fibres in a new GDL without PTFE coating at 500* magnification

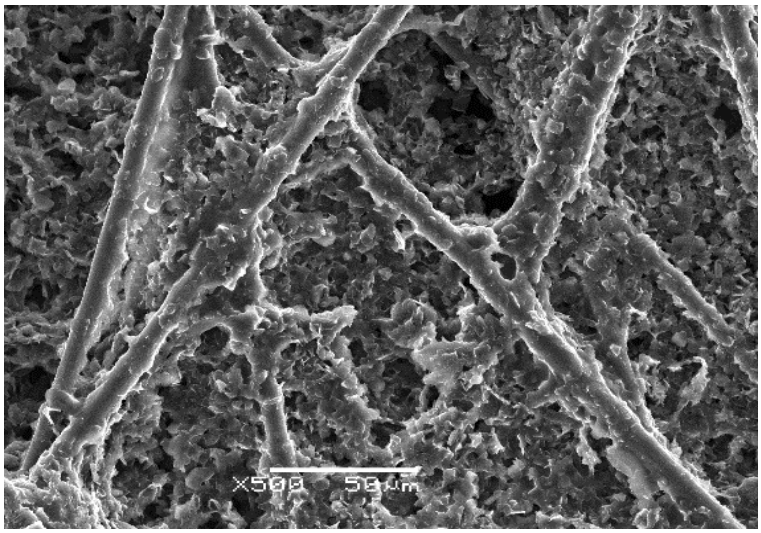

Figure 5-11 Carbon fibres in a new PTFE-treated GDL at 500* magnification

The morphology of a new PTFE-treated GDL is presented in Figure 5-12. Many pinholes and cracks appeared on the roughened PTFE-coated surface. These pinholes and cracks mainly came from inappropriate storage and usage methods because the PTFE coating is very fragile; even small frictions can make the PTFE flake off from the surface. Figure 5-13 provides a more detailed morphology of the pinhole, which was corresponding to the one in Figure 5-12 marked in a red circle. These pinholes offered a suitable space for water produced during the cell reaction. In general, excess water should be removed from the flow channel in order to prevent water flooding. However, the water could stay in

these pinholes. In this case, if the pinhole is full of water, it prevents reactant gases transferring into the reaction sites in the catalyst layer. Consequently, the reaction rate decreases. The cross section of the PTFE-treated GDL is presented in Figure 5-14. The GDL was divided into two layers, the PTFE-coating layer and the carbon fibre layer with depths of approximately 50 μm and 150 μm respectively. The pore size in the PTFE-coating layer was much smaller than that in the fibre layer. Thus, the PTFE-coating layer is usually placed, facing towards to the catalyst layer for the water management.

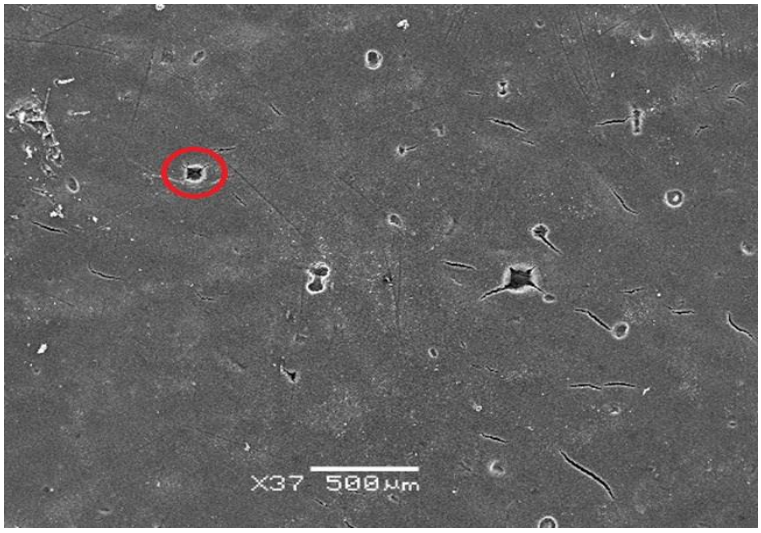

Figure 5-12 Face view of a PTFE-coated GDL at 37* magnification

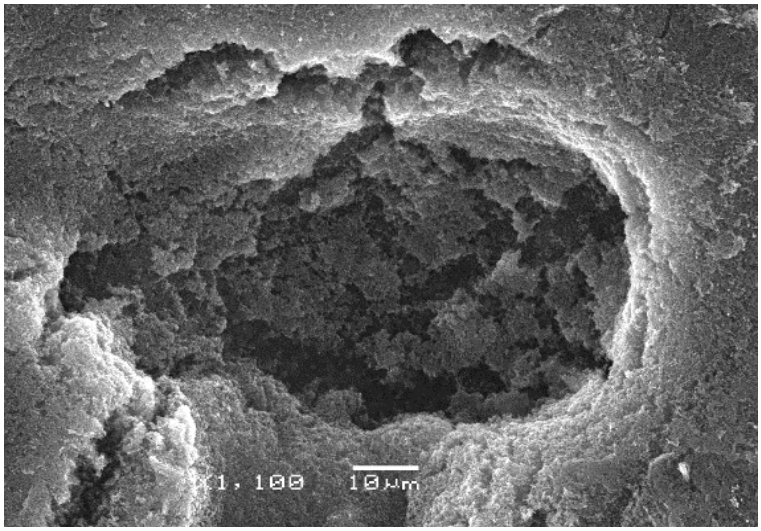

Figure 5-13 A pinhole in a PTFE-coated GDL at 1100* magnification

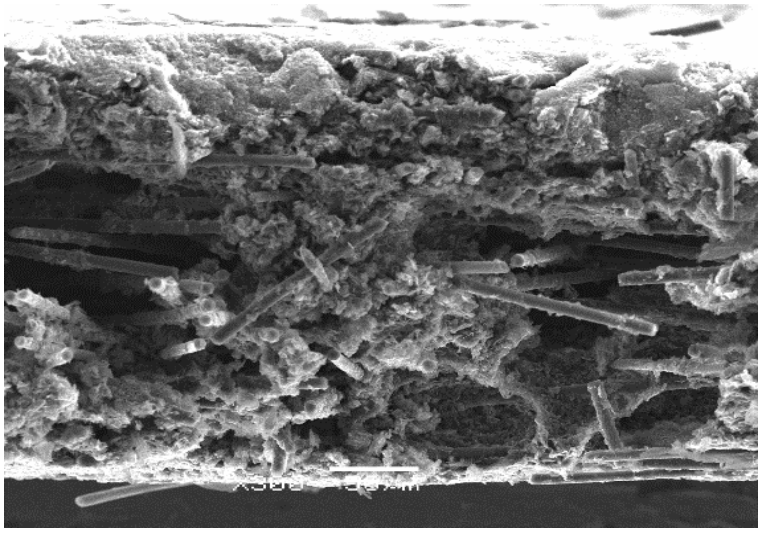

Figure 5-14 A cross sectional view of a new PTFE-coated GDL at 500* magnification

5.3. Microstructural Changes of CCMs and GDLs after Cell Operations

The above section discussed many structural defects in new CCMs and GDLs. These defects can affect the cell performance in two aspects. First, they can lead to an initial low cell performance. In addition, some small defects in new CCMs and GDLs can develop into large ones during a regular cell operation and start-up/shut-down processes, causing a further cell performance reduction. This section mainly focuses on the structural changes of used CCMs and GDLs.

Figure 5-15 presents the cross section of a used MEA. Five layers tightly connected with each other, including two catalyst layers, two GDLs and one Nafion membrane. However, the thickness of the entire MEA varied as opposed to the initial uniform thickness. Clamping forces and hygro-thermal stresses gave rise to this thickness variation. Clamping forces caused the reduction in the thickness of the MEA under the land. On the other hand, the thickness of the MEA under the channel had little changes. During cell operations, hygro-thermal expansions also added more loads on the membrane because of a fixed space between the anode and cathode flow channel plates,

making the membrane undergo permanent deformations, called plastic deformations. Figure 7-4 explains the difference between lands and channels. As a result, these permanent deformations corresponded to the structure of the flow channel plate.

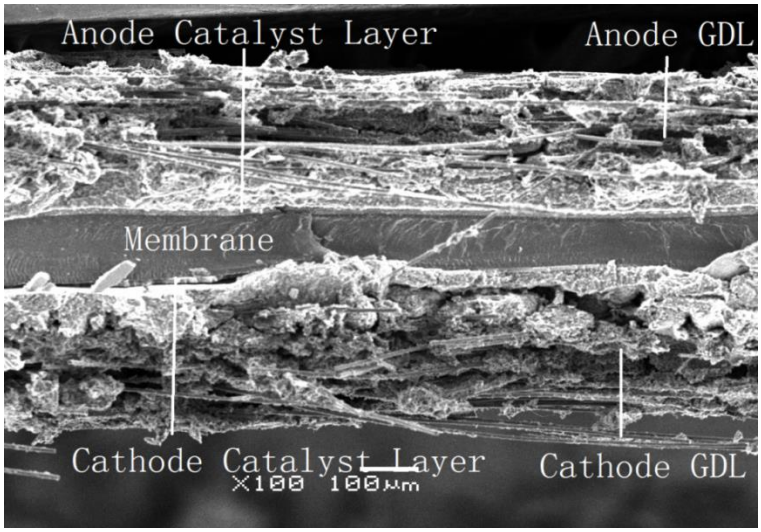

Figure 5-15 A cross sectional view of a used MEA at 100* magnification

This five-layer structure is significant for the performance of PEM fuel cells because a close connection between GDLs and CCMs not only reduces the electronic resistance, but also provides a transport path to the reaction site. Additionally, this close connection helps the water management. Therefore, it is important to discuss this structure in detail. The GDL rested on top of the catalyst layer. The PTFE was coated on only one-side of the GDL. This coated side was facing towards the catalyst layer. As illustrated in Figure 5-16, the pore size of the PTFE coating was larger than that of the catalyst layer. Water was produced in catalyst layers during reactions. Then, it tended to flow into large pores in the PTFE layers. Because of PTFE's hydrophobic characteristic, excess water can easily be removed out of the GDL to the flow channel, from where it can be delivered out the cell stack by the reactant gas flow. Therefore, this pore size difference between catalyst layers and PTFE coatings, and the arrangement of layers helped to relieve the water flooding.

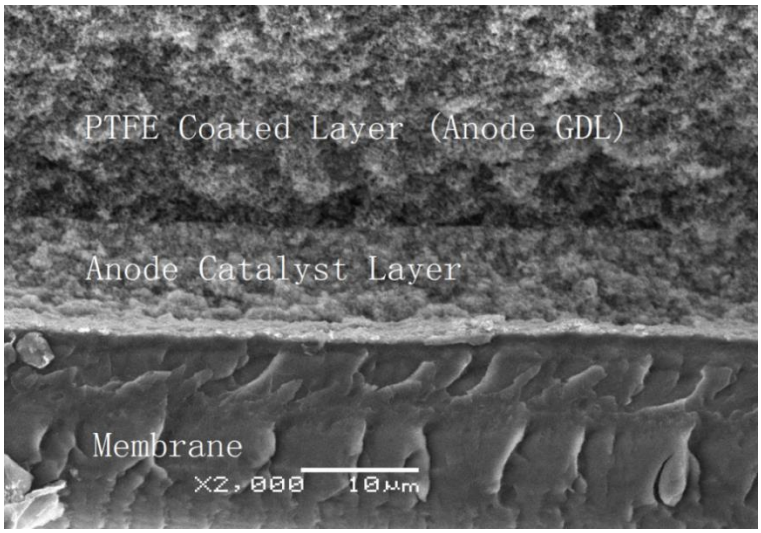

Figure 5-16 Pore size differences between catalyst layers and PTFE coating at 2000* magnification

Although the GDL connected with the catalyst layer in most test samples, some catalyst-GDL delamination and catalyst-membrane delamination still existed in test samples, as presented in Figure 5-17 and Figure 5-18. Unlike the delamination found in new CCMs, unevenly distributed stresses, including clamping stresses and hygro-thermal stresses, could be the main reason for the delamination in used CCMs. In the used CCMs, the length of the separation between the catalyst layer and the membrane was about 1 μm, which was much smaller than that found in new CCMs. This separated catalyst layer still maintained a fairly uniform thickness. However, the delamination found in new CCMs deformed into a bow shape. The reason behind this deformation variation was the difference between the fabrication conditions and cell operating conditions. The fabrication condition for CCMs is usually maintained at a certain level of temperature and relative humidity. This condition remains constant to prevent the shrinkage or expansion of the membrane. Delamination occurs mainly because of inappropriate working temperatures, relative humidity, spray approaches, and unnecessary bending.

However, in an operating fuel cell, the operating temperatures and relative humidity change all the time, which brings changes in thermal-hygro stresses. Also, as mentioned earlier, the water content in the membrane is changing during cell operations. This water content variation can cause different levels of expansions in a membrane, which can

reduce the adhesion between the catalyst layer and the membrane. Once delamination occurs, the reaction rate at the separation region is lower than its surroundings, leading to a non-uniform temperature distribution, and consequently, a non-uniform distribution of water content in the membrane.

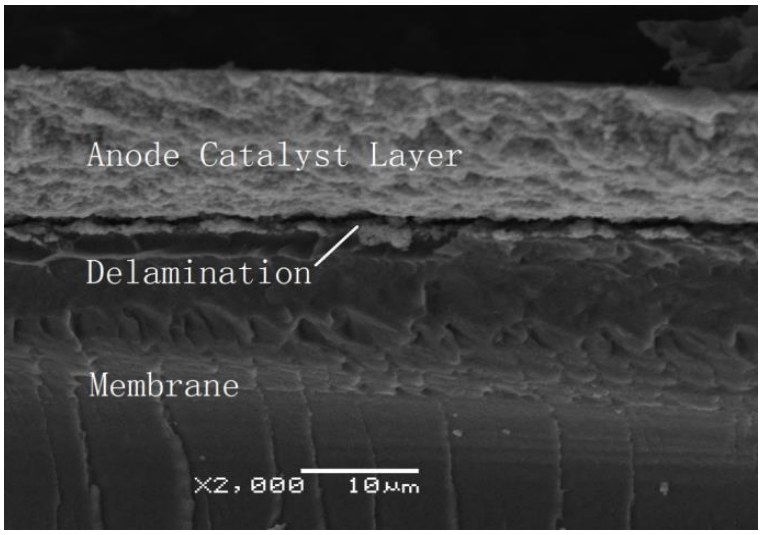

Figure 5-17 Delamination in a used CCM at 2000* magnification

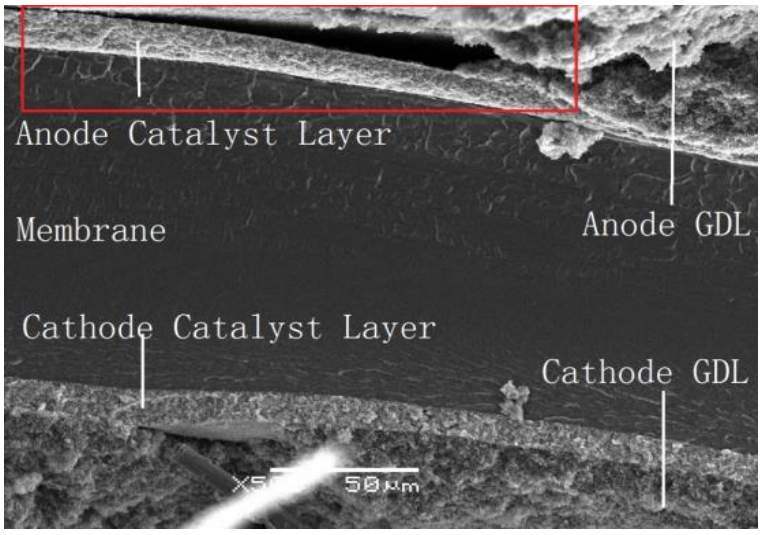

Figure 5-18 Delamination between a GDL and a CCM at 2000* magnification

Figure 5-19 shows the cross section of a used CCM, which witnessed the thickness variation in catalyst layers and membranes. In order to compare the thickness of used and

new catalyst layers and membranes, corresponding measurement relied on *Plot Digitizer* software with an accuracy ±0.24μm. This software is a Java program. It can digitize values off a scanned image. Figure 5-4 and Figure 5-19 provide high resolution images; therefore, they were the selection of these measurements. Eleven evenly distributed locations along the length of the catalyst layer and the membrane provided the measurement spot. Equation 5-1 determined the relative variation of the thickness with the aim of characterizing the thickness uniformity.

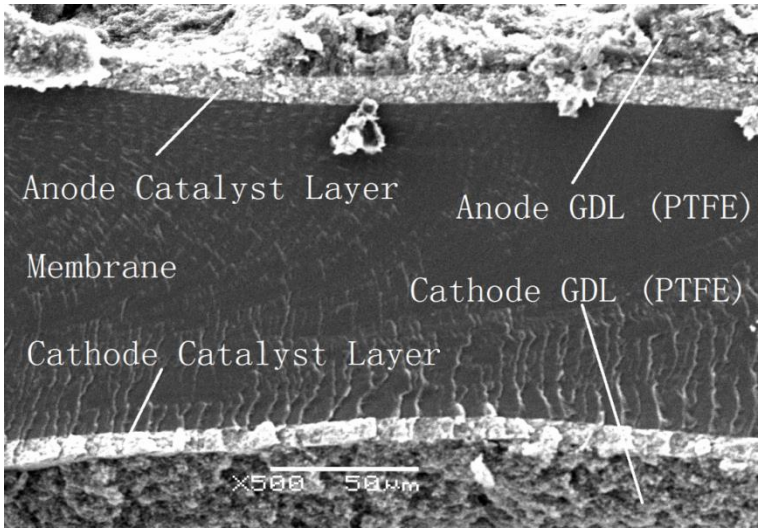

Figure 5-19 Thickness variations of a used CCM

$$relative\ variation = \frac{|individual\ thickness - average\ thickness|}{average\ thickness}$$

Equation 5-1

As illustrated in Figure 5-20, the membrane thickness of a new CCM was fairly uniform. The average thickness was approximately 137.66 μm and the relative variation was from 0.37% to 1.69%. However, the used CCM witnessed a pronounced difference in the thickness. The average thickness reduced to 120.74 μm, and the relative variation was from 1.40% to 8.62%. Mechanical impact might be the main reason for the thinning process in the thickness. Meanwhile, the spatial variation in the deformation (thickness variation) might result from the structure of the flow channel plate, as shown in Figure 3-2 and the uneven temperature and humidity distributions. The membrane thickness is directly linked with the ionic resistance. Therefore, thickness variations result in a non-

uniformed reaction rate, which would in turn strengthen the uneven distribution of temperature and humidity. Consequently, this uneven distribution further contributes to the thickness variation. Understandably, when the thickness of the membrane reduces to a certain level, it may be weaken easily with compressions.

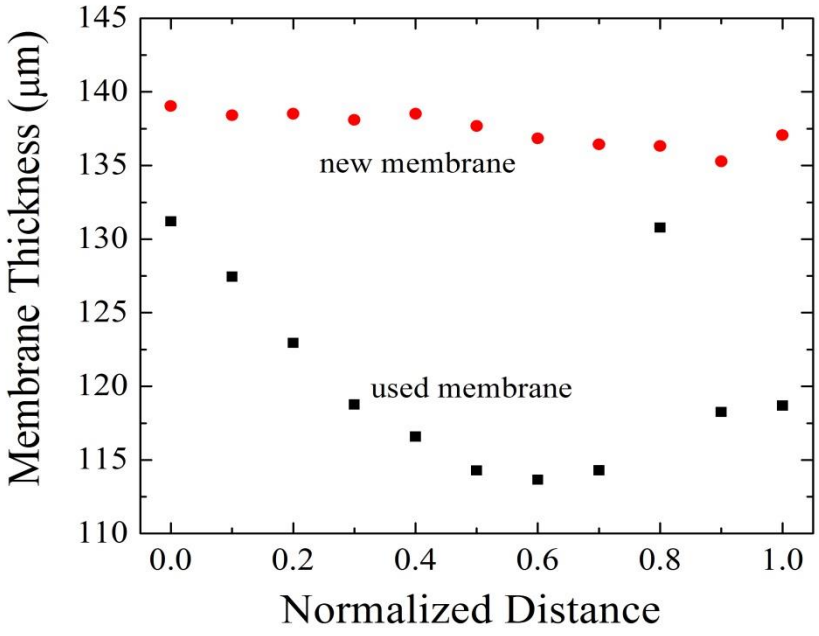

Figure 5-20 Thickness variation of new and used membranes

Figure 5-21 and Figure 5-4 represent the change of catalyst layer thickness. The thicknesses of these two catalyst layers in a new CCM were almost the same. The average of the anode catalyst layer was 10.33 μm, whereas the cathode catalyst layer was 10.17 μm. The relative variation of the cathode catalyst layer ranged from 0.41% to 2.40%, whereas the anode catalyst layer was in the range of 0.01-2.15%. On the other hand, 250-hour testing witnessed a reduction in catalyst layer thickness. The average thickness for the used cathode catalyst layer was 9.04 μm while it was 10.12 μm for the used anode catalyst layer. Additionally, the relative variations were 0.66-18.33% and 0.17-4.41% for the cathode and anode catalyst layers respectively. Again, mechanical stresses could be one factor for this thickness reduction. In addition, Pt migration from the catalyst layer into the membrane was another reason for the changing thickness. The

catalyst layer thickness reduction can bring some microstructure defects, for examples, pinholes. The thinnest thickness region of the membrane existed at location 0.6. Pinhole formations are more like to occur at locations with a high catalyst layer thickness and a low membrane thickness, since the reaction rate is high and more heat is generated. Therefore, hot spot are likely to form at this location which can lead to pinholes.

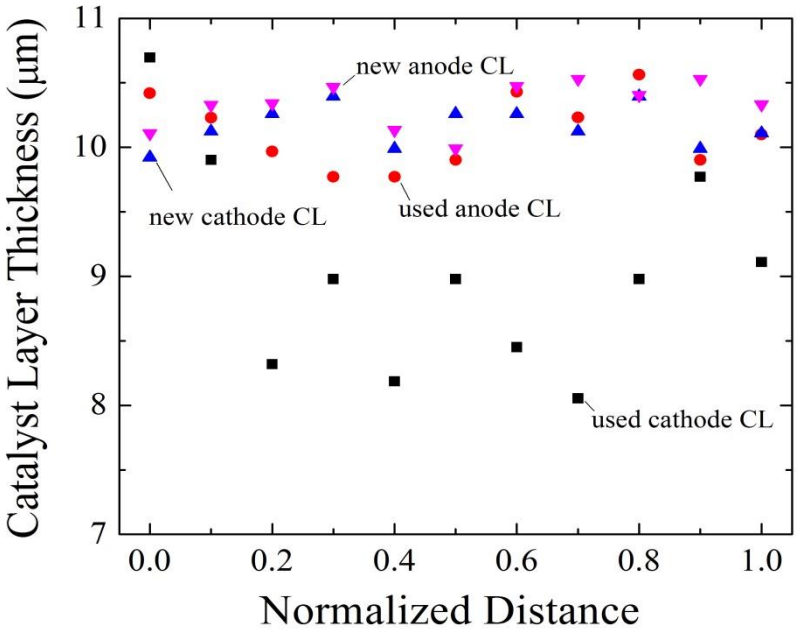

Figure 5-21 Thickness variation of new and used catalyst layers

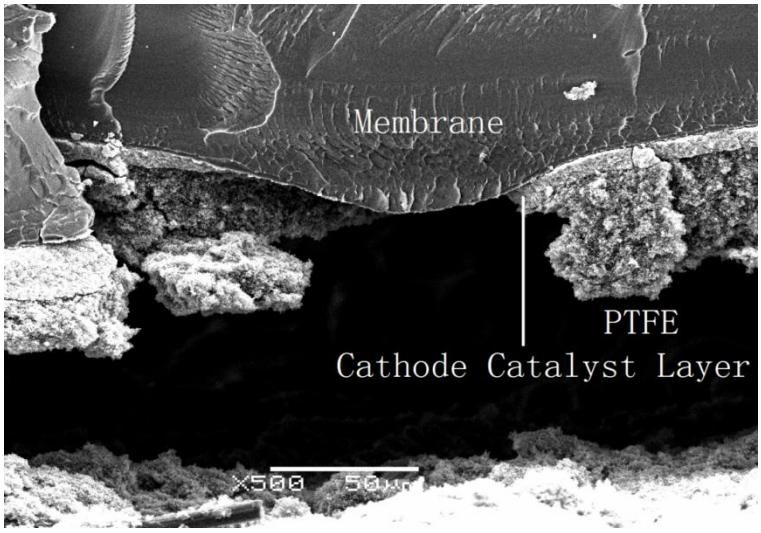

Figure 5-22 The bending of a Nafion membrane and catalyst loss at 500 * magnification

Figure 5-22 shows the deformation and the catalyst loss of a used CCM. As mentioned before, inappropriate mechanical stresses and the structure of the flow channel pattern caused the bending of a CCM. If the mechanical stress is larger than the yield strength of the Nafion membrane, the membrane undergoes a plastic deformation or permanent deformation. As illustrated in Figure 5-22, the Nafion membrane deformed into a bow shape. Also, the catalyst layer, which was originally attached to the Nafion membrane, flaked off. The catalyst layer, a very fragile composite material, needs to be coated on a substrate so that it can maintain a certain shape. In addition, it is less flexible than the Nafion membrane because it only contains around 30% Nafion. Large mechanical stresses resulted in the deformation of a membrane, which brought some cracks in the catalyst layer since it was less flexible. When the fuel cell was under operation, the thermal-hygro stresses further expanded these cracks in catalyst layers. Also, a membrane tended to undergo further deformation during cell operations. All these factors eventually caused the catalyst layer to flake away from the membrane.

Meanwhile, the catalyst loss can further negatively affect cell performance. The reaction rate at one catalyst-loss region is much lower than the surrounding areas. This non-uniform reaction rate along the catalyst layer surface can lead to non-uniform temperature and relative humidity distributions, consequently causing uneven stress distributions. Further, the catalyst loss creates a gap between the membrane and the GDL, which is a suitable space for water flooding. The cracks and gaps leave space for the water which contains dissolved contaminants. These contaminants might finally get into the pores of the catalyst layer and the GDL. The can block the transportation path and deteriorate the cell performance.

Figure 5-23 shows the surface of a used Nafion membrane. Many small cracks and agglomerates existed on the surface. The widths of these cracks were about 0.01μm whereas the length varied. These cracks did not break the Nafion membrane. However, they broke the continuity of the membrane, and therefore would definitely increase the proton resistance. These small cracks might be a suitable place for water flooding, thus contamination dissolved in the water can flow in. Most agglomerates randomly distributed on the membrane surface. In particular, these agglomerates might be the

contaminants from the catalyst layer. The sizes of them were different. However, many bigger agglomerates accumulated on the cracks path, as presented in Figure 5-24.

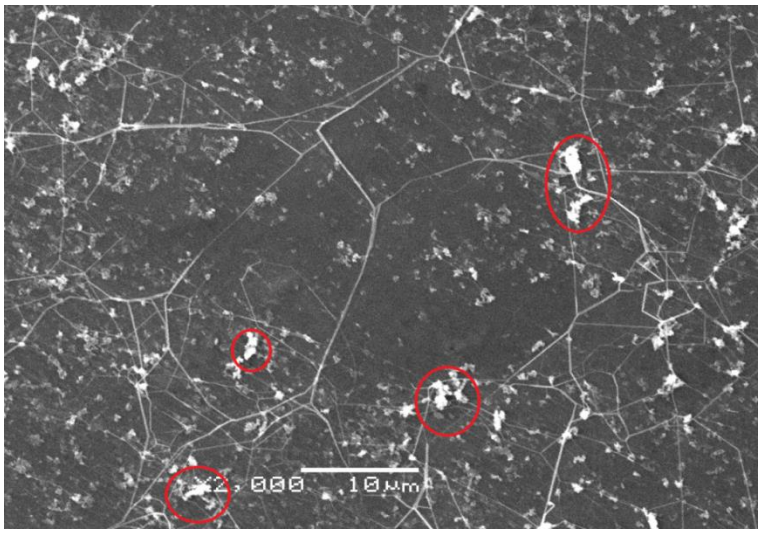

Figure 5-23 Surface cracks on a used membrane at 2000* magnification

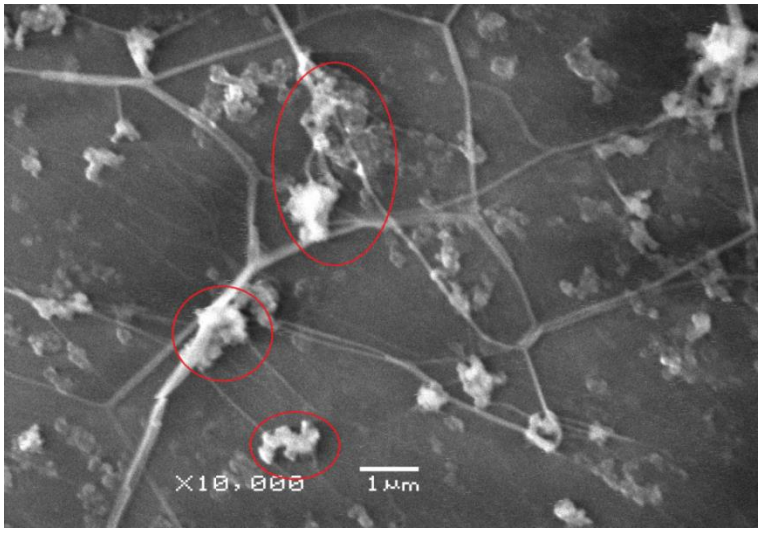

Figure 5-24 Agglomerates on a used membrane at 10000* magnification

5.4. Summary

SEM tests detailed the initial microstructures and their changes in an MEA before and after durability testing. In the testing of new MEAs, structural defects, such as delamination, pinholes, and cracks, occasionally appeared. Further observation of these

new MEAs showed that, initially, the thicknesses of the catalyst layers and Nafion membranes were quite uniform. During the 250 hours of accelerated testing, cell performance underwent a noticeable decay. More structural defects occurred in these used MEAs. Interestingly, catalyst layers and Nafion membranes experienced pronounced changes in the thickness. This thickness variation could result in a series of changes in the fuel cell, leading to a further cell performance reduction. The possibility that large stresses, including clamping forces and hygro-thermal stresses were the reason behind these structural changes necessitated the following study of stress conditions in the MEA of PEM fuel cells.

Chapter 6

Mechanical Properties of Cell Components

The previous chapter suggests that the stress condition of MEAs was the reason behind the microstructural changes. Currently, due to the technique limitation in measuring stresses, numerical modelling is the most promising method to probe the stress condition in MEAs. A reliable structure model involves appropriate constitutive relations. Therefore, the preparation of a comprehensive structure model requires knowing the mechanical properties of different components in a typical PEM fuel cell, which guides the selection of constitutive relations in the modelling. However, to date, only a few studies focus on the mechanical properties of GDLs and catalyst layers. Therefore, as a preparation for the structure model, this chapter mainly concentrates on studying the compressive behaviour of GDLs and catalyst layers using a micro-compression tester and the nanoindentation technique, respectively.

6.1. Mechanical Properties of Gas Diffusion Layers

6.1.1. Quasi-Static Compressive Behaviour

6.1.1.1. A Typical GDL Compressive Stress-Strain Curve (loading and unloading)

Figure 6-1 shows a typical GDL compressive behaviour after one cycle loading and unloading. First, it is clear that the compressive stress-strain relations of a loading and unloading curve were not linear, in contrast with most mechanical behaviour of GDLs used in the modeling. Hence, a common deformation analysis for PEM fuel cells using Hook's law might not be appropriate. Second, the compressive stress-strain curve contained three regions: an initial region (compression stresses were quite small, 0-0.25 MPa), a middle region (compression stresses were between 0.25-2 MPa) and a final region (compression stresses were larger than 2 MPa). This phenomenon can be explained through the microstructural changes of GDLs under compressions.

GDLs have highly porous structures, made up of numerous carbon fibres that connect with each other in a random manner. Although in reality all the carbon fibres are connected throughout, for the ease of understanding, it is assumed that the GDL is composed of many alternating layers. One set of layers consists of densely packed randomly connected fibres. The second set of layers is also connected with these random fibres but these layers are less dense.

Due to GDLs' special structure, GDLs behaved differently when compression stresses changed. When compression stresses were comparatively very small (in the initial region) they did not destroy the layer structure. Instead, compression stresses made the less-dense layer more condensed without breaking the carbon fibres inside the layers. This structure can return to its original shape once the compression stresses were released. Because the GDL behaved elastically to small compression stresses, the stress-strain curve was linear at this compression range. Compared with the GDLs' behaviour in the initial stage, increased compressive stresses in the middle region, as shown in Figure 6-1, continuously compressed the less-dense layer and made the less-dense layers more condensed, which led to carbon fibre breakages among the denser layers themselves as well as carbon fibre slippages among the less-dense layers. These microstructural changes were non-reversible; thereby GDLs behaved inelastically. As the compressive stresses continued to

increase, the less-dense layers experienced significant reductions, leading to the layer deposition. As a result, the whole GDL was much more and evenly condensed, as presented in Figure 6-2. The stress-strain relation became elastically and linear again due to this condensed structure.

GDLs' compressive loading curve and unloading curve were different. As shown in Figure 6-1, the unloading curve did not follow the same path as the loading curve although the compressive stress was released in the same way where it was applied. Similar to the loading stress-strain curve, the unloading stress-strain curve was divided into three regions. The first unloading curve was a linear region; however its Young's modulus was larger than that of its corresponding loading curve. At the first unloading region, the GDL was initially compressed under large compressive stresses. The whole GDL was very condensed. When the compressive stresses were gradually released, some of the compressed structures tended to turn back to their original shape. However, due to the previous permanent structure changed, the GDLs still had a non-linear stress-strain curve region, which was larger than that of the loading curve, indicating that more carbon fibre breakages and slippages occurred during this period.

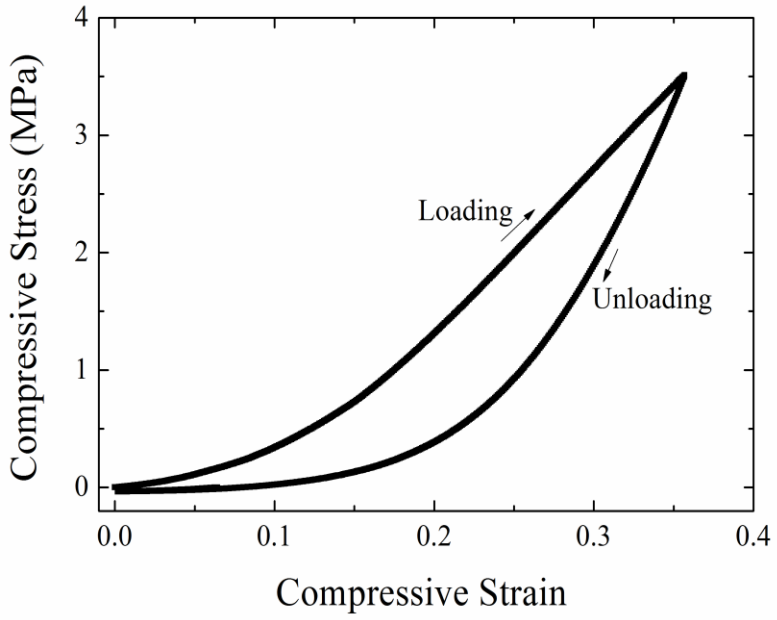

Figure 6-1 The compressive behaviour of a raw GDL (sprectracarb carbon paper) under one cycle of loading and unloading (five-sample stack, temperature 25^{o}C, RH 30%)

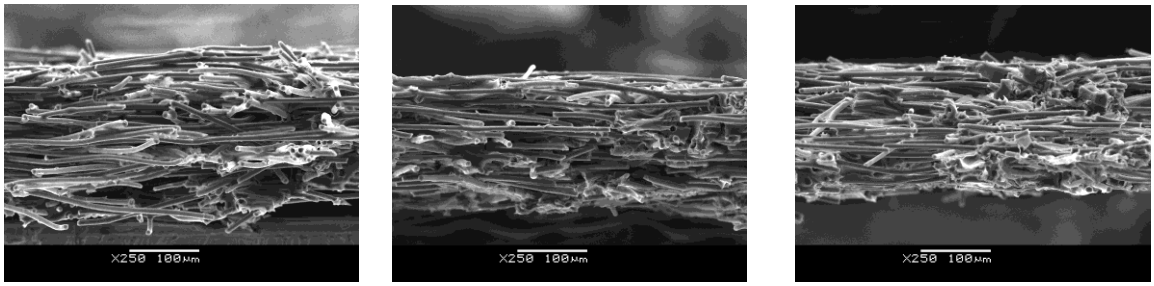

(a) Uncompressed GDL (b) Compressed GDL (2.7MPa) (C) Compressed GDL (6 MPa)

Figure 6-2 The microstructure of a raw GDL (temperature 25^{o}C, RH 30%)

6.1.1.2. The Effect of Stack Sizes

It is considerably challenging to carry out high-precise compressive tests on GDLs, because of its micro-thickness. In general, testing a several sample stack helps to reduce experimental errors. However, the effect of stack sizes on compressive behaviour of GDLs still remains unclear. So far, to the best knowledge of the author, there are few studies regarding this issue. Most of the available literature does not even mention how many GDLs were used in a stack in the experiments. Therefore, in order to clarify the stack size impact, the study of GDL compressive behaviour involved stacks with different numbers of GDLs (1~10).

As illustrated in Figure 6-3, the stress-strain curve of a one-sample stack was different from a two-sample stack, and both of them indicate differences from large stacks. Under the same compressive stresses, these two stacks had higher compressive strains than others, meaning that they were more compressible. With the increase in stack sizes, the compressive behaviours tended to become less different. This phenomenon can be explained from two perspectives. From the perspective of the elastic strain energy, thinner stack are more conducive for the energy transformation from the test rod to the tested stack, so that the stack can store more strain energy, which expresses itself as a more compressible behaviour. From the perspective of microstructural changes, the compression stress triggers the microstructural changes of GDLs. However, GDLs tend to deform to a structure that helps it to resist the impact of compressions. The thicker sample has more complicated microstructures, compared to a thinner sample, suggesting that it has a better capability to resist compressions. Therefore, the thinner samples are

more compressible. This compression process was recorded by an OM testing, as presented in Figure 6-4. More microstructural changes of GDLs (i.e. carbon fibre breakage) occurred with the increase in deformations.

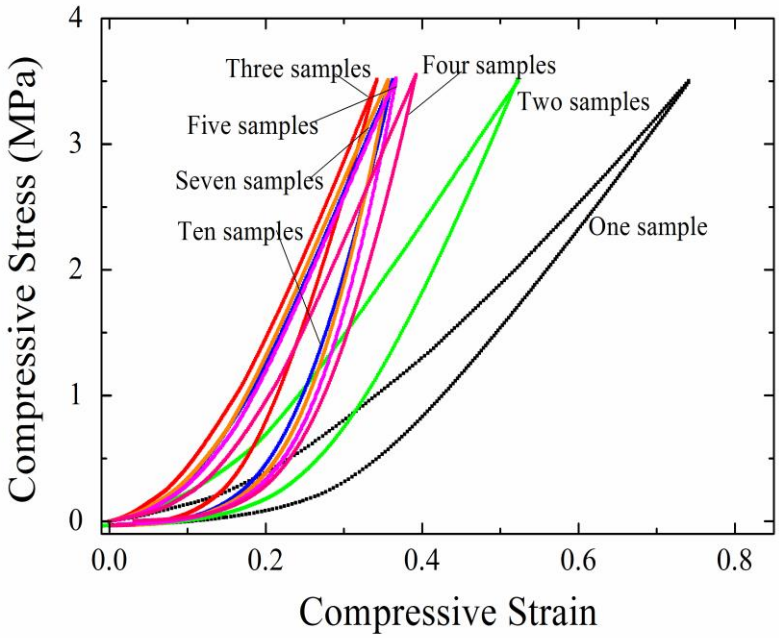

Figure 6-3 The compressive behaviour of raw GDLs with different stack sizes (SpectraCarb 2050A-0850 carbon paper, 1-10 samples, temperature 25°C, RH 30%)

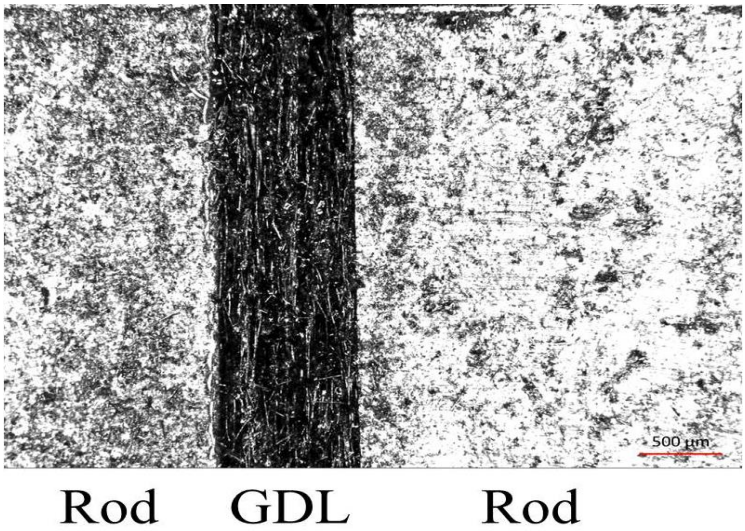

Figure 6-4 A five-stack raw GDL under compressions (temperature 25°C, RH 30%)

Figure 6-3 indicates that the compressive behaviours of GDLs actually changed with the numbers of GDLs. However, so far the literature of the measurement regarding GDLs compressive properties normally did not mention clearly the stack sizes, which might put into question the reliability of the data. Besides, the structure modeling of PEM fuel cells requires the GDL mechanical properties. In real PEM fuel cells two pieces of GDLs, sandwiched with a CCM, are normally used as the component of an MEA. This might trigger another problem: what stack sizes are the best to represent the real GDLs compressive properties in an MEA? Therefore, in order to obtain more convincing and meaningful results, the measurement of GDLs' compressive behaviour should consider the effect of the stack size of GDLs.

Many studies used either piecewise linear expressions or exponential correlations to describe the compressive behaviour of GDLs. However, none of them paid attention to the unloading curve, which is important in mechanical modelling. For the ease of modelling, the loading and unloading compressive behaviours are described using 4th polynomial curves, as shown in Table 6-1.

Table 6-1 4th order polynomial correlations for loading/unloading curves

Stack size	Type	Correlation
One-sample stack	loading	$y = 0.01575 + 0.1823x + 9.745x^2 - 5.988x^3 + 1.445x^4$
	unloading	$y = -0.01413 - 0.05827x - 2.2228x^2 + 27.90x^3 - 21.96x^4$
Two-sample stack	loading	$y = 0.02329 + 0.4193x + 15.00x^2 + 5.226x^3 - 21.47x^4$
	unloading	$y = -0.03743 + 1.204x - 17.18x^2 + 100.2x^3 - 89.68x^4$
Five-sample stack	loading	$y = 0.008661 + 0.7545x + 18.36x^2 + 92.03x^3 - 203.9x^4$
	unloading	$y = -0.06414 + 2.10531x - 26.35x^2 + 135.3x^3 + 3.491x^4$

As indicated in Figure 6-5, due to the measurement uncertainty, the compressive behaviour of GDLs with different stack sizes can mainly be divided into three categories: a one-sample stack, a two-sample stack and a five-to-ten-sample stack. As previous mentioned, a large stack size helps to reduce the experimental errors. Also, the general shapes of their curves are similar. Therefore, a five-sample stack was mainly used for the following test. The loading curve contains sufficient information to describe the

compressive behaviour of GDLs. The following sections only concentrated on studying the effects of temperatures, relative humidity, and the amounts of PTFE coatings on the compressive behaviour.

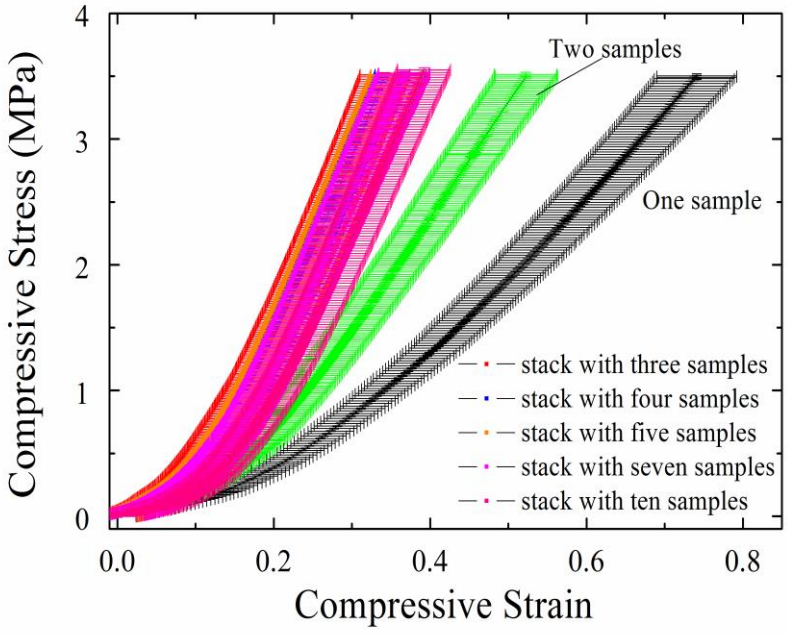

Figure 6-5 The typical raw GDL compressive stress-strain loading curve with error bars (SpectraCarb 2050A-0850 carbon paper, temperature 25°C, RH 30%)

6.1.1.3. The Effect of Operating Temperatures

A PEM fuel cell is typically working at operating temperatures of around 65°C to 85°C; therefore, the compressive behaviour of GDLs during these temperature ranges is worth being investigated. However, studies in the literature regarding the GDL's compressive properties have mainly focused on compression tests at room temperature (about 25°C). In order to clarify operating temperature effects, the compressive stress-strain curves of GDLs were probed at different temperatures. Tests relied on a five-stack raw GDL (SpectraCarb 2050A-0850, carbon paper) at four various temperatures (25°C, 45°C, 65°C, and 85°C) with a constant relative humidity 30%. As illustrated in Figure 6-6, these four curves overlapped and the differences between them were statistically insignificant. Although small variations can be seen among these curves, they lied within the range of measurement uncertainties. These results indicated that the compressive behaviour of

GDLs did not change appreciably within the fuel cell operating temperature range; thus the effect of operating temperatures on GDLs' compressive properties was negligible. As mentioned, the compressive behaviour of GDLs mainly depended on the microstructure changes. Because carbon fibres have a high temperature tolerance and a very low thermal expansion, the increased testing temperature did not change the microstructure status of GDLs and carbon fibre properties in an appreciable way, compared to those at room conditions. Therefore, the compressive behaviour remained unchanged.

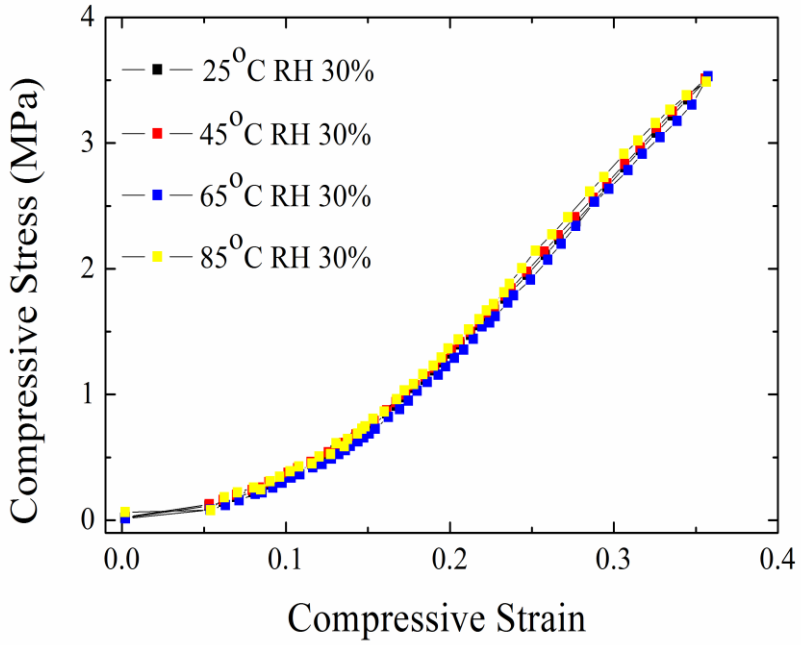

Figure 6-6 The compressive behaviour of raw GDLs with different temperatures (SpectraCarb 2050A-0850 carbon paper, a five-sample stack, temperature 25°C, RH 30%)

6.1.1.4. The Effect of Relative Humidity

Since the proton conductivity of a Nafion membrane is directly correlated with its hydration level, the humidification of a membrane is usually essential. Therefore, PEM fuel cells operate at a humidified condition (normally above 80%). A GDL is a composite material, consisting of carbon fibres and resin which is used as a binder to connect the carbon fibres into a certain shape. The most common type of resin used in GDLs is phenolic resin. Studies indicate that this resin becomes weaker as its moisture content increase [88]. Hence, it is possible that the compressive behaviour of GDLs at a high

humidified condition is different from that at a dry condition. However, very few studies have been performed to characterize the compressible properties of GDLs at a highly humidified condition.

In order to clarify the relative humidity effects, the GDLs were tested at the same temperature of 85^{o}C with two different relative humidity (30% or 85%). As shown in Figure 6-7, the initial linear region of compressive stress-strain curve at different humidified conditions did not show any significant differences, compared with that for the dry sample. It needs to be mentioned that due to the measurement uncertainty, the compressive behaviours of dry and humidified GDLs at the initial region were similar enough to be considered as the same, although it is possible that they might have slight differences. However, for the non-linear region, the compressive behaviours of the humidified GDLs became more compressible than the dry samples; whereas for the final linear region, the Young's modulus of GDLs became similar. A moist environment can soften the resin and make it easier for the carbon fibres to dislocate and slip. However, when the compression stresses were very small, they did not destroy the layer structure in spite of the softened resin, which was the reason why at the initial region, the compressive properties of dry and humidified samples were quite the same. When the compressive stresses started to increase to a point where the carbon fibre breakage and slippage can occur, the compressive stress-strain curves moved into the non-linear region. Because of the softened resin, the humidified GDL became more compressible than the dry GDL sample at this region. As the compressive stresses continued to increase, the whole GDL became more condensed, meaning that the microstructure of the GDL became stable. At this stage, the softened resin did not have an appreciable impact on the microstructure changes; hence the compressive strain changed at approximately the same rate as that of the dry sample.

6.1.1.5. The Effect of Hydrophobic Coatings

GDLs are often treated with hydrophobic binders (PTFE) for the water management. This treatment results in the microstructural changes, as illustrated in Figure 5-14. Compared with a raw GDL without PTFE, the PTFE coating not only wraps the carbon fibre and fills out some pores, but also acts as a binding agent, which leads to a different

compressive behaviour from a raw GDL. However, there is no in-depth investigation regarding the microstructural changes caused by the PTFE coatings and their corresponding compressive behaviours. The following tests measured Toray-type carbon papers (TGP-H-120) with different amounts of PTFE loadings.

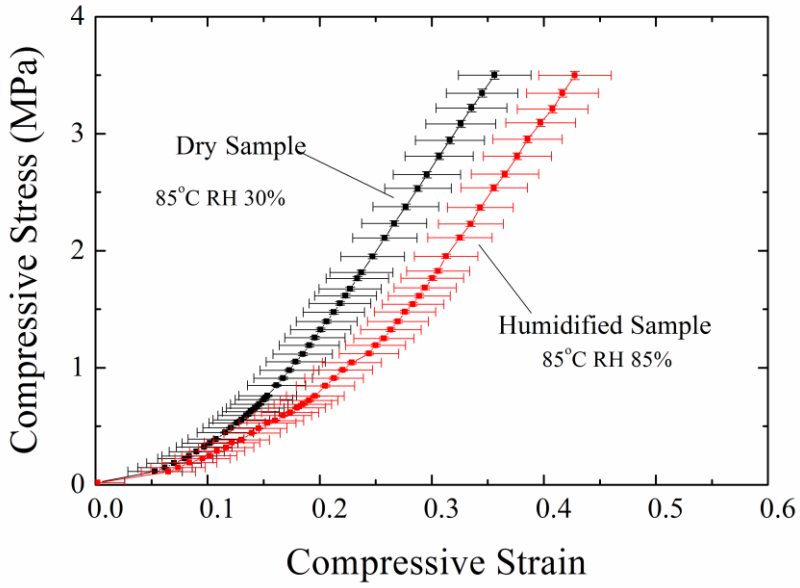

Figure 6-7 The compressive behaviour of GDLs under different relative humidity (SpectraCarb 2050A-0850 carbon paper, a five-sample stack, temperature 85°C)

Since the compressive behaviours of GDLs are significantly affected by their microstructures, PTFE's effects on GDLs' microstructures need to be investigated first in order to have a comprehensive understanding of its impact on compressive properties of GDLs. Figure 6-8 and Figure 6-9 show the integral and differential distributions of pore volume as a function of pore radius for uncompressed GDLs with different amounts of PTFE loadings. Table 6-2 provides the volumetric porosity of GDLs with different amounts of PTFE loadings. Because the PTFE wrapped the carbon fibres, the pore volume decreased with the amount of PTFE loadings. The radii of the pores in tested sample were mainly between 10 to 20 μm. The most common pore radius was 15 μm. In addition, in spite of its effect in reducing the overall pore volume, PTFE coatings did not exert appreciable effects on the maximum pore size and size distribution of GDLs.

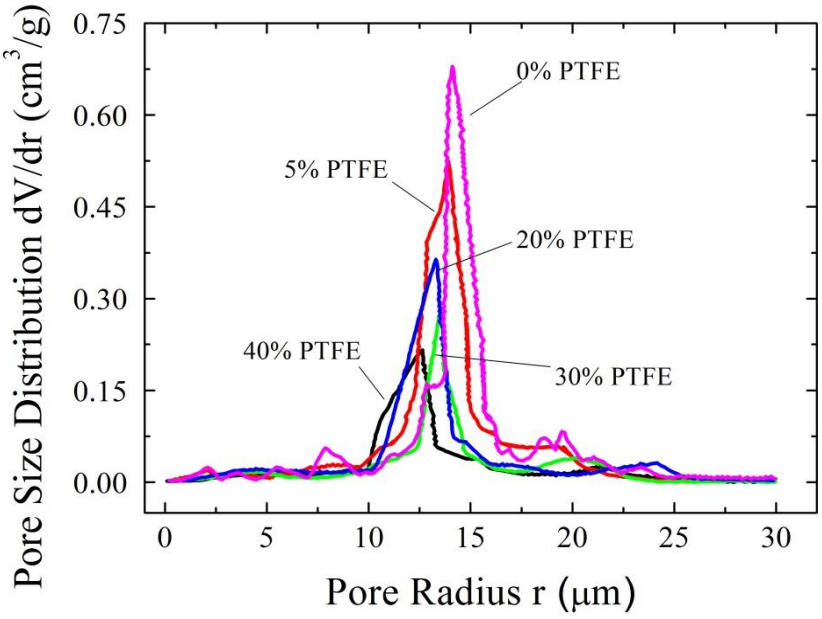

Figure 6-8 The uncompressed integral distribution of pore volume as a function of logarithmic pore radius for Toray carbon paper (TGP-H-120) GDLs with 0-40% PTFE treatments

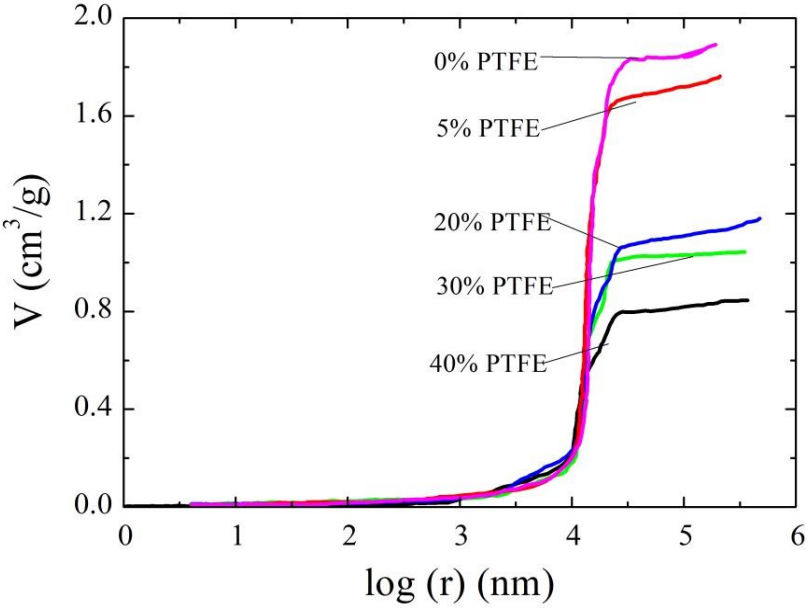

Figure 6-9 The uncompressed differential distribution of pore volume as a function of pore radius for Toray carbon paper (TGP-H-120) GDLs with 0-40% PTFE treatments

Table 6-2 The volumetric porosity of GDLs with different amounts of PTFE loadings

PTFE loading	0%	5%	10%	20%	30%	40%
Porosity	0.7818	0.7303	0.7204	0.6987	0.6560	0.6281
Uncertainty	±0.0040	±0.0039	±0.0038	±0.0037	±0.0036	±0.0035

Figure 6-10 illustrates the stress-strain curves of Toray carbon paper GDLs with different PTFE loadings (0%, 5%, 10%, 20%, 30% and 40%). Similarly to that of the SpectraCarb carbon paper, the compressive behaviour of a PTFE-coated GDL can also be divided into three regions. However, it varied with the amount of PTFE loadings. In the initial region, all the stress-strain curves overlapped, indicating that the amount of PTFE loading actually did not show any appreciable effects on the GDLs' compressible behaviour when the compressive stresses were smaller than 1.5 MPa. The initial small compressive stresses made the less-dense layers more condensed. Because of PTFE coatings, the number of less-dense layers became increasingly smaller. However, since the initial compressive stress was so small, it only condensed the less-dense layers in a reversible way, which would not affect the original compressive behaviour in an appreciable way.

However, the compressive behaviours changed when the compressive stresses move into the middle region. As shown in Figure 6-10, raw GDLs (Toray 0% PTFE) behaved differently from GDLs with PTFE coatings. Raw GDLs (Toray 0% PTFE) were more compressible, whereas GDLs with different amounts of PTFE coatings still acted in a similar way. Because compressive stress at this range resulted in the carbon fibre breakage and slippage, a raw GDL (Toray 0% PTFE) behaved non-linearly. On the other hand, the added PTFE coating worked as a binder and strengthened the GDL structure, thereby reducing the carbon fibre breakages and slippages. This might be the reason why it is less compressible. As the compressive stresses moved into the third region, they made the whole GDL more evenly condensed. In this case, the presence of PTFE actually wrapped the carbon fibres and reduced the pore volume. Because of the lay depositions, at this region the measured compressive behaviour was the combination of the GDL carbon fibres and the different levels of PTFE coatings, which was why all the stress-strain curves were different from each other. However, for a common PEM fuel cell

operating clamping force (0.4-1.2MPa), the compressive behaviour of GDLs with different PTFE coatings was quite the same.

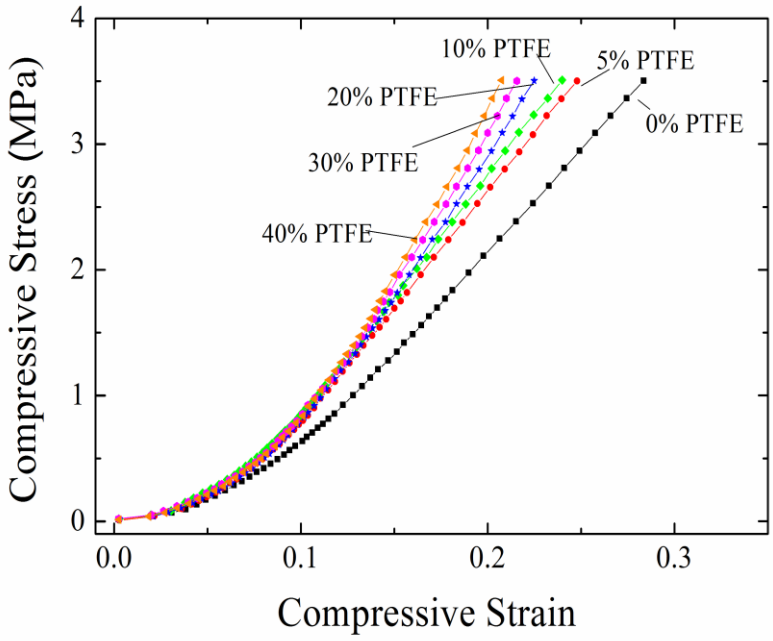

Figure 6-10 The Compressive behaviour of GDLs with different PTFE loadings (a five-sample stack, temperature 25°C, RH 30%)

6.1.2. Cyclic Compressive Behaviour

In an operating fuel cell, the MEA suffers a combination of clamping forces and thermal-hygro stresses. The clamping force is constant once the fuel cell is assembled. However, due to the cyclic changes of the operating conditions (shut-down/start-up processes), the thermal-hygro stresses will change during the operation, indicating that the cyclic compressive nature of GDLs is worth being studied. However, so far studies regarding the cyclic compressive behaviour of GDLs are only limited to a few cycles; whereas the real durability target for a fuel cell to be used in vehicles is approximately 30,000 shut-down/start-up cycles.

6.1.2.1. Five Cycles of Loading and Unloading

Figure 6-11 shows the stress-strain behaviour of GDLs after five loading-unloading cycles. Unlike the first cycle, the loading and unloading curves tended to become similar with the increase of the cycles, which resulted from the reductions in less-dense layers. After the first compression, the GDL experienced a reduction in less-dense layers. The whole GDL became more condensed. However, some less-dense layers still existed, which would experience continuously condensed processes after the subsequent cycles. Figure 6-11 shows that the compressive strain under the same compressive stress increased after five cycles. Such an increase reduced by about 60% after five cycles, as illustrated in Figure 6-12.

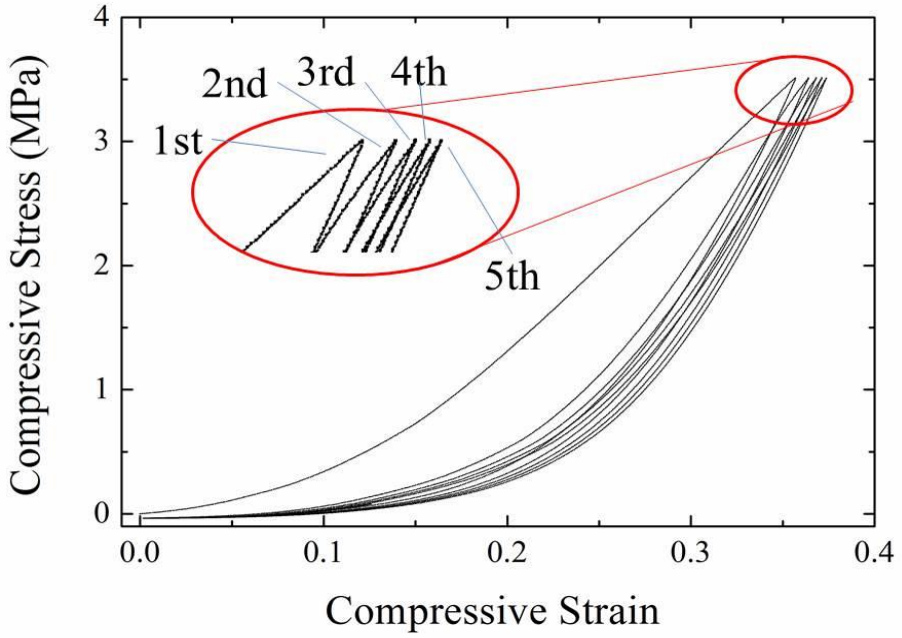

Figure 6-11 The compressive behaviour of a raw GDL (SpectraCarb) under five loading and unloading cycles (a five-sample stack, temperature 25°C, RH 30%)

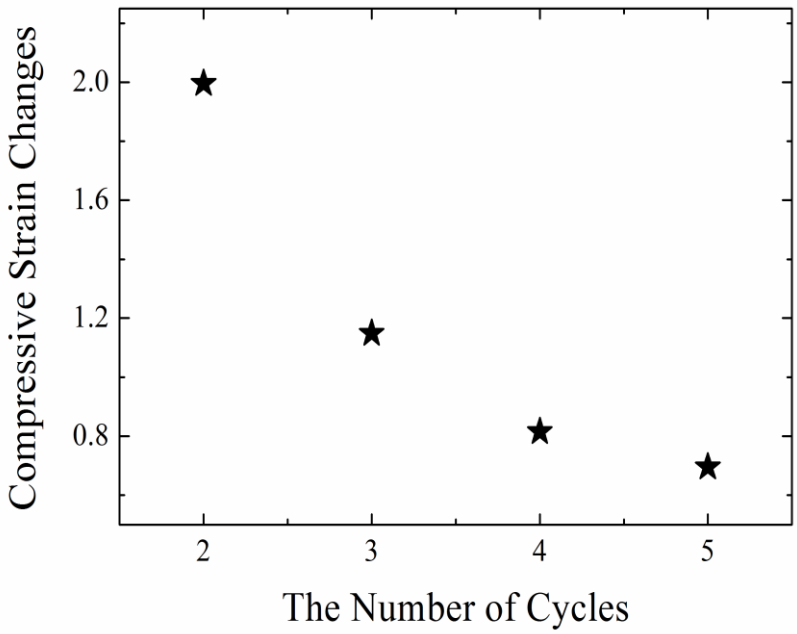

Figure 6-12 The compressive strain changes under the maximum compressive stress during five cycles (a raw SpectraCarb GDL, a five-sample stack, temperature 25°C, RH 30%)

6.1.2.2. Effect of Cyclic Loading

In order to simulate the cyclic loading (the start-up/shut-down processes), GDLs were compressed under the range from 1-2 MPa. The assembled forces were assumed to be 1 MPa, whereas the cyclic loadings resulting from the thermal-hygro stresses were between 0-1 MPa. The GDL was first compressed to 2 MPa. Then, the compression was gradually reduced to 1 MPa. This cycle repeated for about 2000 times. As shown in Figure 6-13, the compressive strain measured at 2 MPa was plotted as a function of cycle number.

After a few cycles, the compressive strains of both PTFE-coated GDLs and raw GDLs experienced an appreciable increase even under the same compressive stress. After about 1500 cycles, the compressive strains of both kinds of GDLs reached a relatively stable state. In addition, a few sudden increases can be noticed on these two curves. This phenomenon was still linked with the less-dense layers. Similar to what occurs after 10 cycles, as depicted in Figure 6-12, the less-dense layers continues to be condensed to a certain point under a certain compressive stress. However, due to the cyclic load, the GDLs experienced fatigue issue, consequently causing further carbon fibre breakage and

slippage, as shown in Figure 6-14. These further damages resulted in new less-dense layers, thereby further increasing the compressive strain. After about 1500 cycles, carbon fibres dislocated and became condensed. Then, there was little room for the new-born less condensed layers; hence the stress-strain curve became stable. Moreover, because a GDL was basically a random porous material, even two GDL samples from the same batch would not behave exactly the same. Therefore, these sudden jump increases randomly occurred. Table 6-3 shows the volumetric porosity of GDLs after 2000 cycles. Due to the carbon fibre breakage and slippage, the porosity of raw and coated GDLs decreased. Although the reduction was only 6%, it is possible that these changes would lead to significant changes in other properties of GDLs, such as thermal and electrical resistances.

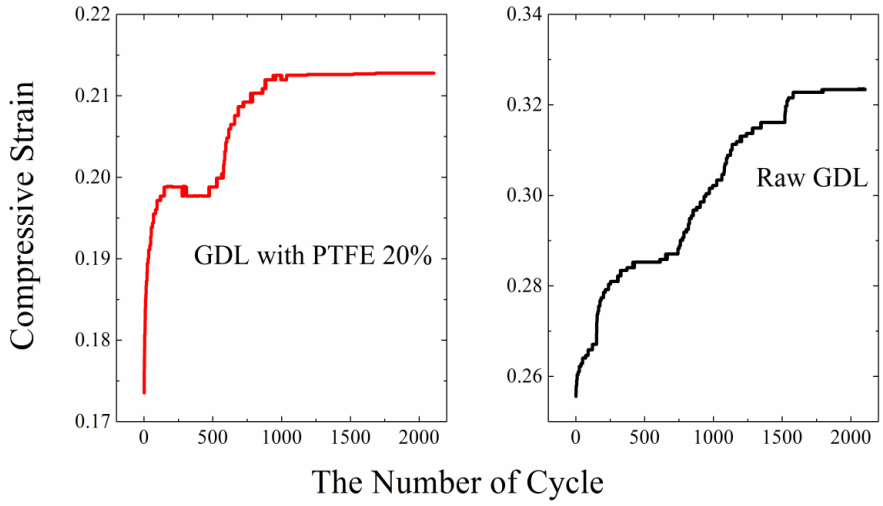

Figure 6-13 The compressive behaviour of a raw GDL after 2000 cycles (a five-sample stack temperature 25°C, RH 30%)

Table 6-3 The volumetric porosity of GDLs after 2000 cycles

PTFE loading	Uncompressed volumetric porosity	Volumetric porosity after 2000 cycles	Relative changes, %	Uncertainty, %
0%	0.7818	0.7702	1.48	0.51
20%	0.6987	0.6560	6.11	0.53

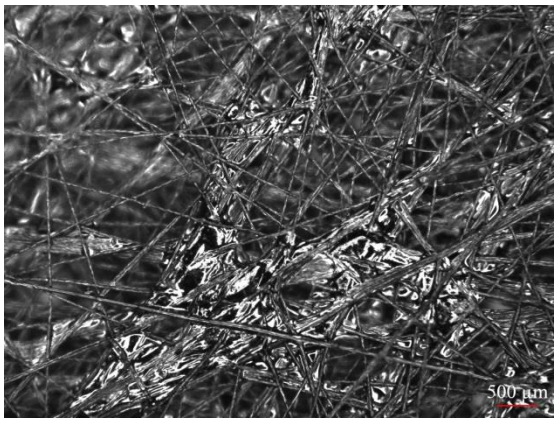

(a) Uncompressed raw GDL-I

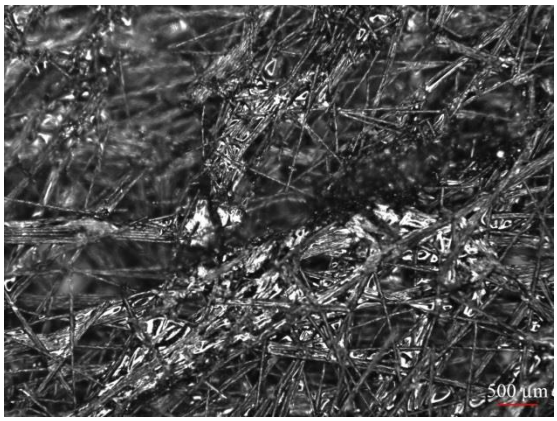

(b) Compressed raw GDL-I after 2000 cycles

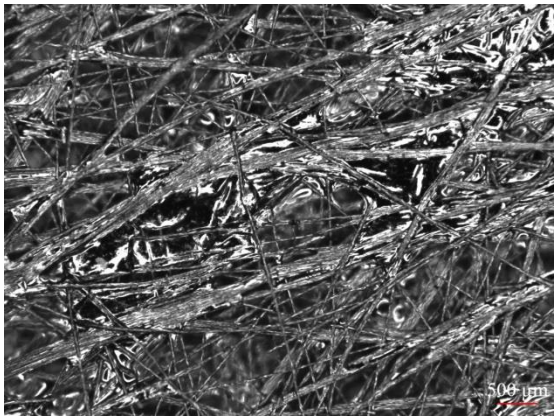

(c) Uncompressed raw GDL-II

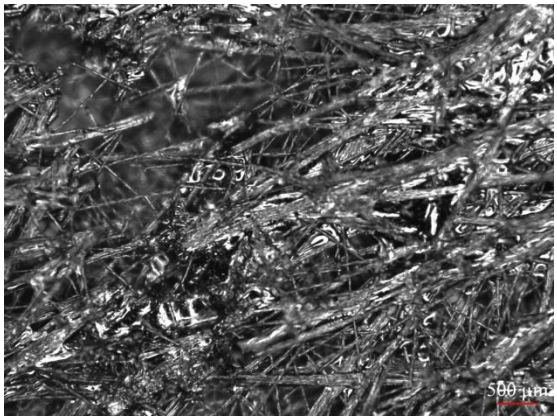

(d) Compressed raw GDL-II after 2000 cycles

Figure 6-14 The microstructural changes of a raw GDL after 2000 cycles

6.2. Mechanical Properties of Catalyst Layers

All the cell structure modelling done, so far, ignored the catalyst layers in the modelling and considered the catalyst layer and the gas diffusion layer as one single layer because of the unknown mechanical properties of catalyst layers. Catalyst layers' mechanical properties, including Young's modulus, can be obtained from the nanoindentation technique, using the relations mentioned in Chapter 3.

Figure 6-15 illustrates the indentation curves for the catalyst layer in terms of load and displacement. It included one loading and unloading curves. The loading and

displacement relation was linear. The unloading curve determines the Young's modulus, as shown in Figure 6-16 and Figure 6-17. The Young's modulus of catalyst layers varied with different locations, depths and applied forces. According to Table 5-1, the distributions of pores, Pt particles and carbon supports were not uniform. Therefore, during the process of the indentation, the Berkovich indenter could encounter pores, aggregated Pt particles or carbon particles, which affected the Young's modules values. Here, we took the Young's modules of catalyst layer as the average 450 MPa.

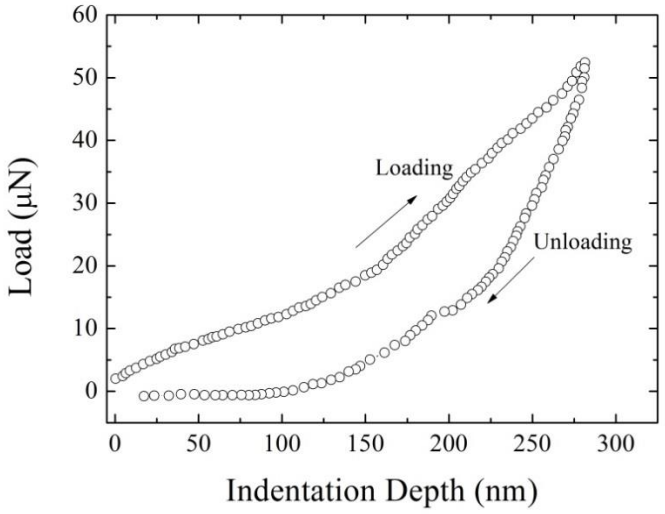

Figure 6-15 Nanoindentation results for catalyst layers in terms of load and indentation depth

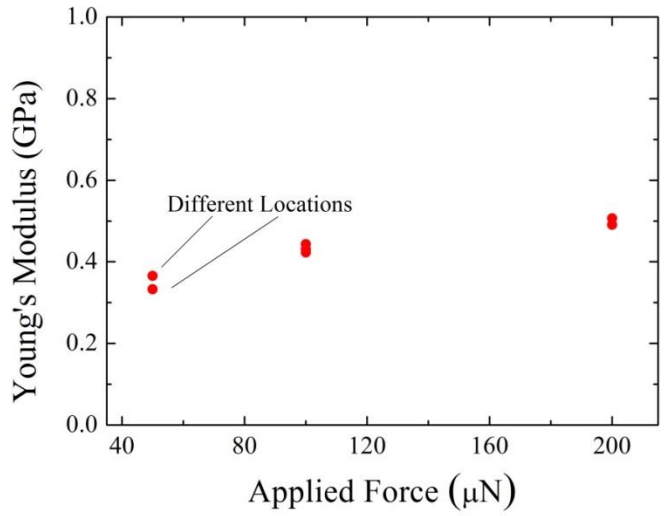

Figure 6-16 Young's modulus of catalyst layers under various applied forces

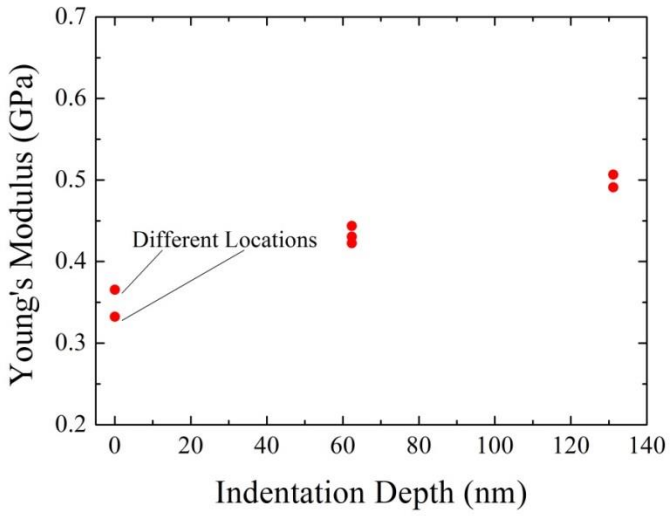

Figure 6-17 Young's modulus of catalyst layers with various indentation depths

6.3. Summary

The structure model of a PEM fuel cell strongly depends on the compressive behaviour of GDLs and catalyst layers. In an operating fuel cell, a GDL suffers from not only the clamping force and thermal-hygro stresses but also cyclic changes of these stresses; therefore, the importance of GDLs' compressive behaviours under common operating conditions and cyclic loadings cannot be ignored. This chapter focuses on the effects of stack sizes, operating temperatures, relative humidity, the amount of PTFE coatings, and cyclic loadings on the compressive properties of GDLs. The results indicated that microstructure changes made GDLs' compressive behaviours disobey Hook's law. Therefore, mechanical modelling in previous research, where a GDL was assumed to have elastic properties, might not be appropriate. Previous research did not consider the impact of stack size; however, it did affect the measurements. The funding showed that, in general, GDLs with various amounts of PTFE coatings behaved differently, yet, during the common operating compression range, their properties were almost the same.

Various conditions created somewhat different effects on GDLs' compressive behaviour. The results showed that the common PEM fuel cell operating temperature did not change the mechanical properties of GDLs in an appreciable way, whereas the relative humidity

could soften the GDL binder, making the GDL more compressible. However, during a common operating compression range, such a softening effect was not significant. Moreover, cyclic loading further varied the GDL's microstructure, and changed its original porosity and corresponding mechanical properties.

Compared to GDLs, it is even more challenging to measure catalyst layers' mechanical properties because of its structure; however, the nanoindentation technique made this measurement possible. The catalyst layer had an elastic mechanical behaviour with a Young's modulus that changed with the applied force and the indentation depth. This occurred because pores and Pt/C agglomerates did not distribute uniformly.

The above obtained mechanical properties are very important because they guided the selection of various constitutive relations for cell components in a structure model. The following structure model included GDLs, catalyst layers and Nafion membranes. Based on the experimental data, a hyperelastic model, Blatz-Ko model, simulated GDLs' nonlinear compressive behaviours. In addition, an elastic model simulated catalyst layers' mechanical behaviour. Meanwhile this model also considered its thermal and hygro-expansion under various cell operating conditions.

Chapter 7

Mechanical Behaviour of MEAs

Chapter 5 suggests that microstructural changes of MEAs occur mainly because of inappropriate stresses, including hygro-thermal stresses and clamping forces. This suspicion necessitated the study of the stress and deformation of MEAs. This chapter presents three conditions to clarify the effects of clamping forces, cell temperatures, and relative humidity on the stress and deformation of an MEA. A temperature of 25^{o}C and a relative humidity of 30% defined the initial temperature and relative humidity conditions, namely the zero stress-state.

- **Condition 1**: Impose clamping forces with a constant cell temperature of 75^{o}C and a relative humidity of 100%. Clamping force was applied by linearly increasing the clamping pressure from 0.2 MPa to 0.8 MPa.
- **Condition 2**: Increase cell temperature with a fixed clamping force of 0.4 MPa and a relative humidity of 100%. All the cell components had the same temperature. The temperature of the entire fuel cell assembly was linearly increased from 25 ^{o}C to 75^{o}C, while maintaining a relative humidity of 100%.

- **Condition 3**: Increase the relative humidity with a fixed clamping force of 0.4 MPa and a cell temperature of 75°C. Only the catalyst layers and Nafion membranes were assumed to react to relative humidity which increased from 30% to 100%.

7.1. The Effect of Clamping Force

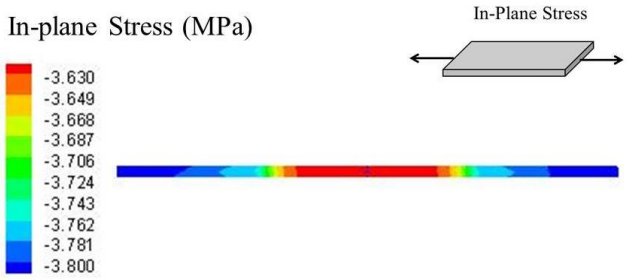

Figure 7-1 The in-plane stress distribution of the Nafion membrane with a clamping force of 0.8 MPa, a temperature of 75°C and a relative humidity of 100%

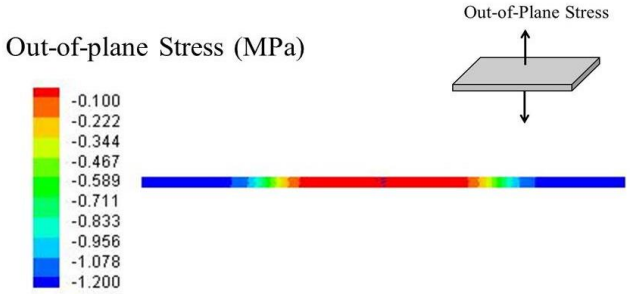

Figure 7-2 The out-of-plane stress distribution of the Nafion membrane with a clamping force of 0.8 MPa, a temperature of 75°C and a relative humidity of 100%

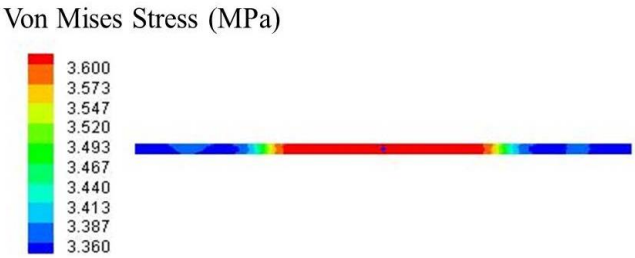

Figure 7-3 The Von Mises stress distribution of the Nafion membrane with a clamping force of 0.8 MPa, a temperature of 75°C and a relative humidity of 100%

A proper clamping force is a significant factor for cell performance. It should be large enough so that the contact resistance between each cell component reaches a reasonable

level, thereby improving cell performance. However, an inappropriately large clamping force can also result in structural defects in an MEA, causing a cell performance reduction. Figure 7-1, Figure 7-2, and Figure 7-3 illustrate the three different stress distributions on the Nafion membrane with a temperature of 75^{o}C, a relative humidity of 100%, and a clamping force of 0.8 MPa. For in-plane and out-of-plane stresses, the stress under the channel was always smaller than that under the land. However, the Von Mises stress distribution showed an opposite condition. The Von Mises under the channel was greater than that under the land.

The Von Mises stress is not really a stress, but a number determining whether the stress combination at a given point will cause plastic deformation. A structure model involved a complex three-dimensional system of stresses, indicating that at any point within a body there are stresses acting in different directions. The direction and magnitude of stresses changes from point to point. The Von Mises stress relies on a formula for combining these three stresses into an equivalent stress, which is then compared to the yield stress of the material, as shown in Equation 4-16.

During a common operating condition, a Nafion membrane had different deformations at various locations. The membrane under the channel tended to bulge, whereas the one under the land experienced thickness reductions. This deformation difference could give rise to several structure defects, such as catalyst loss and cracks, especially at the transition region between the land and the channel. Meanwhile, deformation induced the in-plane stress. The membrane under the land, suffering the out-of-plane stress, resisted the bulge of the membrane under the channel, which was why it had a greater in-plane stress. In addition, since the in-plane stress was much larger than the out-of-plane stress, the Von Mises stress largely depended on it, as presented in Equation 4-16. Therefore, in the following, we will mainly focus on studying the effects of different operating conditions on the in-plane stress.

In order to study the effect of clamping forces on the in-plane stress, it is better to concentrate on two different locations, as shown in Figure 7-4, because these two locations experienced two different deformations. One location is under the centre of the land, whereas the other is under the centre of the channel. Figure 7-4 illustrates the stress

conditions at these two locations on the Nafion membrane surface. The in-plane stress continued to increase overall with the clamping force. However, the in-plane stress under the land was larger than that under the channel. Understandably, the raised clamping force strengthened the bulge effect of the Nafion membrane under the channel. Meanwhile, the Nafion membrane under the land resisted this effect. As a result, the in-plane stress on the Nafion membrane under the land was always larger than that under the channel. Moreover, the in-plane stress under the land had a higher increase rate as the clamping force increase.

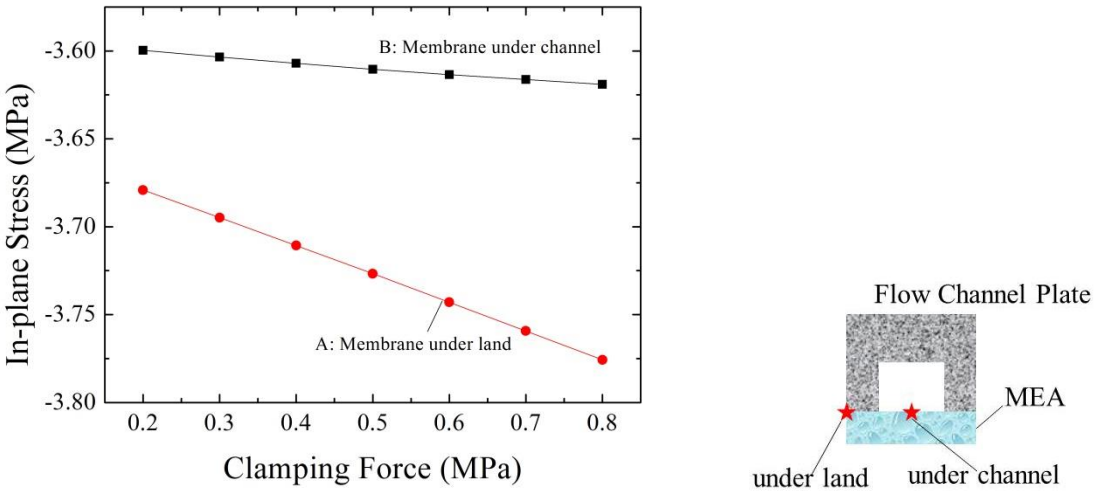

Figure 7-4 The in-plane stresses at two locations on the Nafion membrane's surface with a temperature of 75°C and a relative humidity of 100%

As illustrated in Figure 7-5, the Von Mises stresses on the Nafion membrane under the channel and under the land varied. For the Nafion membrane under the land, the Von Mises stress decreased with a raised clamping force. This is because the enhanced clamping force strengthened both the in-plane and the out-of-plane stresses. Based on Equation 4-16, the subtraction of in-plane and the out-of-plane stresses could lead to the reduction in the Von Mises stress. On the other hand, the Von Mises stress for the Nafion membrane under the channel behaved differently. Because of a low increase rate of the in-plane stress under the channel with the levelled clamping force, the Von Mises stress on the Nafion membrane under the channel increased. This difference meant that the Nafion membrane under the channel was more likely to have greater plastic deformations with raised clamping forces at a range from 0.2 MPa to 0.8 MPa, whereas the membrane

under the land had a less possibility to suffer large plastic deformations under larger clamping force at this range.

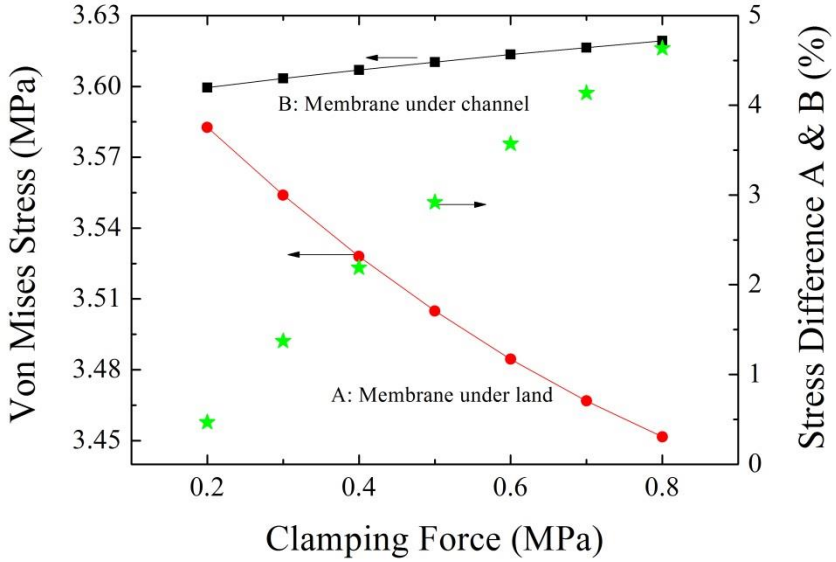

Figure 7-5 The Von Mises stress at two locations on the Nafion membrane's surface with a temperature of 75°C and a relative humidity of 100%

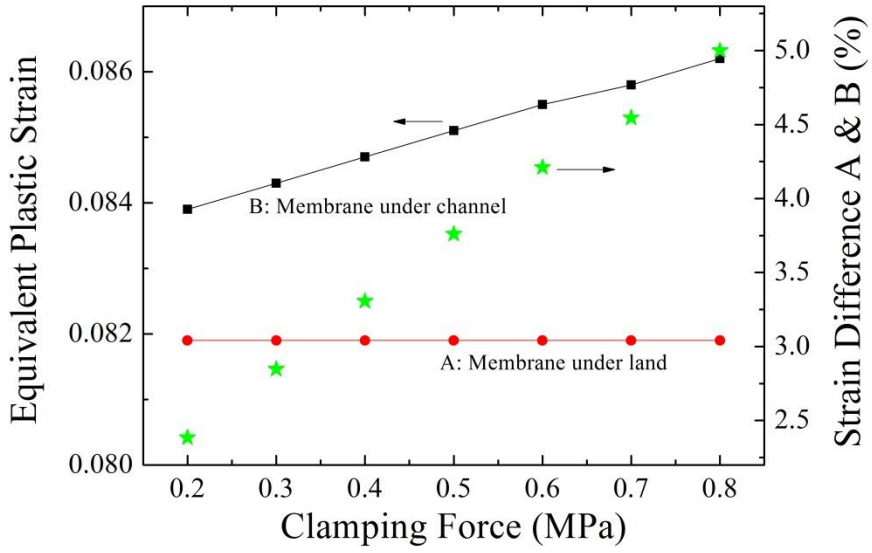

Figure 7-6 The equivalent plastic strains at two locations on the Nafion membrane's surface with a temperature of 75°C and a relative humidity of 100%

A corresponding phenomenon also occurred in Figure 7-6, which reflects the equivalent plastic strain on the Nafion membrane. Equivalent plastic strain gives a measure of the

amount of permanent strain in an engineering body. Equation 4-24 shows its formula, which was calculated from the component plastic strain. The equivalent plastic strain under the land remained constant with the increase in clamping forces, because of the decreased Von Mises stress on the membrane under the land. However, it increased for the Nafion membrane under the channel. During operations, the Nafion membrane under the channel bulged and the Nafion membrane under the land thinned. Plastic strains meant that some membrane parts of this bulge and thickness reduction cannot return to its original shape after unloading, namely the shut-down process. However, the permanent strain on the Nafion membrane also had impacts on catalyst layers which were coated on the membrane. These layers were less flexible than the membrane. Nafion membranes' unrecoverable deformations could easily cause the catalyst flake off the Nafion membrane, as shown in Figure 5-22. Another interesting phenomenon is that merely increasing the clamping force had an insignificant effect on the enhancement of plastic strain. The results shows that when the clamping force was 0.8 MPa, which was four times larger than the original clamping force, 0.2 MPa, the plastic strain under the channel only rose less than 3%.

7.2. The Effect of Operating Temperature

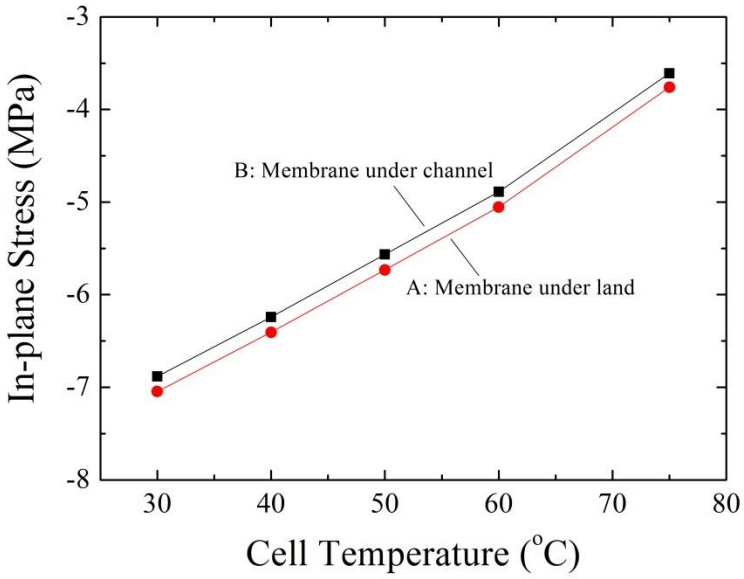

Figure 7-7 The in-plane stress at two locations on the Nafion membrane's surface with a clamping force of 0.4 MPa and a relative humidity of 100%

To date, more researchers suggest that the optimal working temperature for a PEM fuel cell is around 70°C-75°C. For the start-up process, a cell temperature can increase from 30°C to 75°C. Within this temperature range, the overall in-plane stress decreased, as presented in Figure 7-7. The temperature increase motivated the thermal expansion and a corresponding increase in the swelling expansion, which, in theory, enhances the in-plane stress. Nevertheless, the raised temperature also softened the Nafion membrane, thereby relieving the in-plane stress. As a result, the combination of these two factors led to the in-plane stress reduction. Therefore, the temperature has a major role in relieving the in-plane stress.

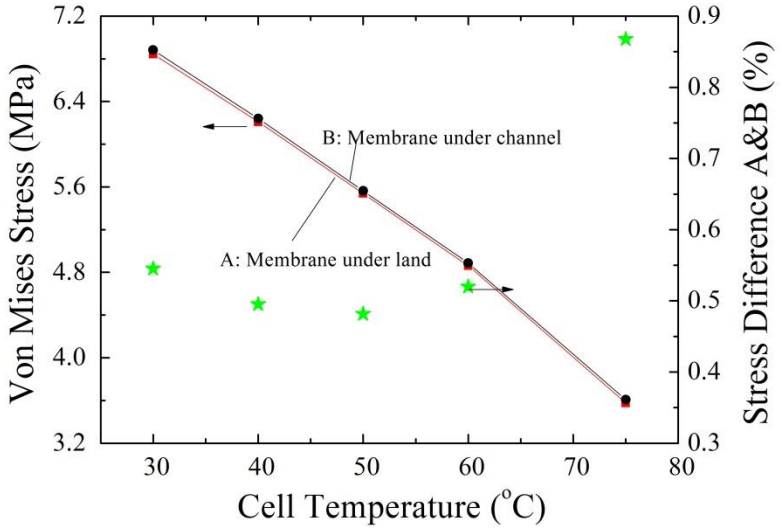

Figure 7-8 The Von Mises stress at two locations on the Nafion membrane's surface with a clamping force of 0.4 MPa and a relative humidity of 100%

According to Figure 7-8, the Von Mises stresses decreased with the cell temperature enhancement. However, it was always larger than the yield stress because high temperatures not only softened the Nafion material, but also lowered membrane's yield stress. In addition, the Von Mises stress distribution was quite uniform on the Nafion membrane, meaning that the entire MEA had plastic deformation. The difference for membrane under the land and under the channel was less than 1% because the in-plane stress was insensitive to enhanced cell temperatures, as shown in Figure 7-7. A corresponding distribution also existed in the equivalent plastic strain. In addition,

compared to the effect of clamping force, raised temperatures caused a 50% greater increase in the equivalent plastic strain, as presented in Figure 7-9.

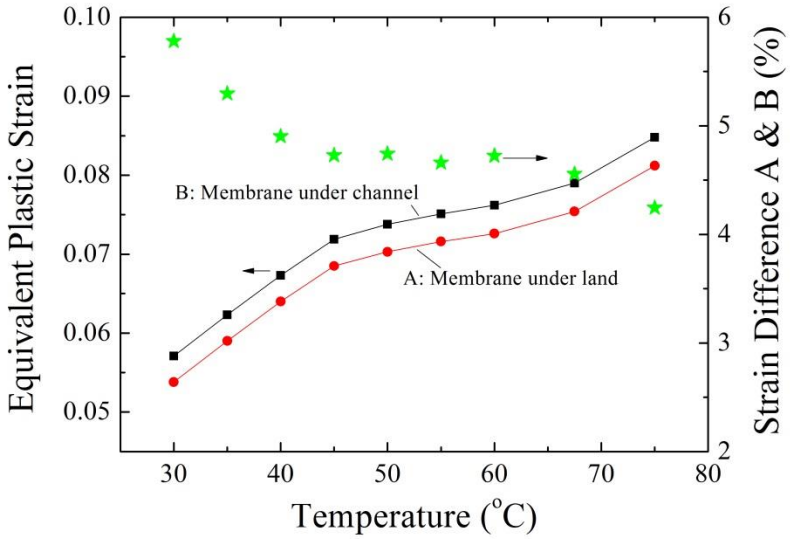

Figure 7-9 The equivalent plastic strain at two locations on the Nafion membrane's surface with a clamping force of 0.4 MPa and a relative humidity of 100%

7.3. The Effect of Relative Humidity

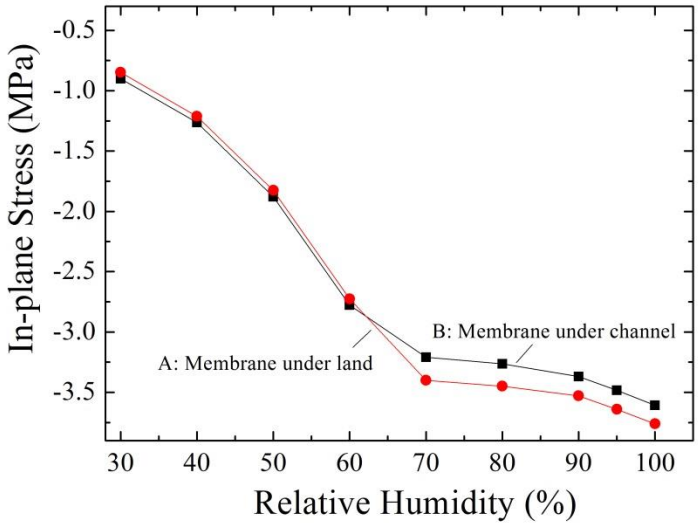

Figure 7-10 The in-plane stress at two locations on the Nafion membrane's surface with a clamping force of 0.4 MPa and a temperature of 75°C

A high relative humidity helps Nafion membranes and catalyst layers to maintain a certain level of hydration, while inducing significant swelling. Figure 7-10 shows the in-plane stress condition of the Nafion membrane with an increasing relative humidity. During this process the overall in-plane stress increased about 300%. Similar to a high cell temperature, a high relative humidity also has a softening-effect. However, compared to the effect of cell temperatures on expansions, the expansion resulting from increased relative humidity was much more appreciable than that from the increased temperature. Hence, the increase in relative humidity was attributed to the rise in the in-plane stress, although a high relative humidity could soften the Nafion membrane, which, in turn, explained the increase in the Von Mises stress, as illustrated in Figure 7-11. The Von Mises stress had a more than four times enhancement, which corresponds to the significant increase in the in-plane stress. In addition, the difference in the Von Mises stress at different locations became smaller as the relative humidity rise.

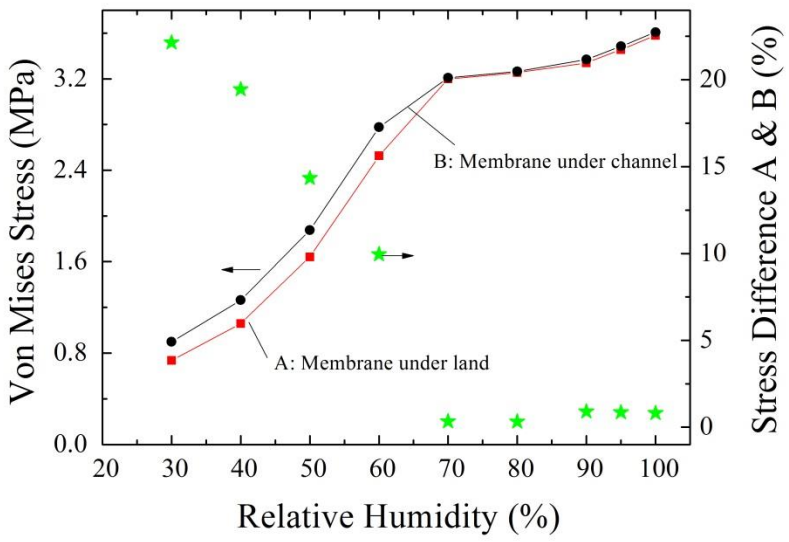

Figure 7-11 The Von Mises stress at two locations on the Nafion membrane's surface with a clamping force of 0.4 MPa and a temperature of 75^{o}C

When the cell was working at 75^{o}C with a clamping force of 0.4 MPa, the relative humidity determined whether the membrane had plastic deformation, as shown in Figure 7-12. A plastic strain occurred when the relative humidity was higher than about 65%, which indicated that relative humidity, compared with the clamping force and the cell

temperature, was the most significant factor determining if the Nafion membrane suffers plastic deformations. Since a PEM fuel cell generally works with a relative humidity of 90%-100%. The Nafion membrane inevitably suffers plastic deformations.

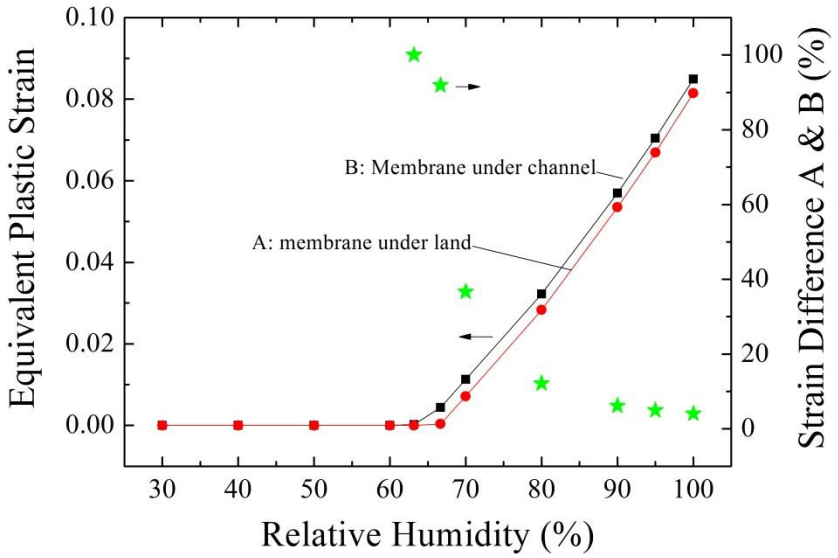

Figure 7-12 The equivalent plastic strain at two locations on the Nafion membrane's surface with a clamping force of 0.4MPa and a temperature of 75°C

7.4. One Fuel Cell Duty Cycle

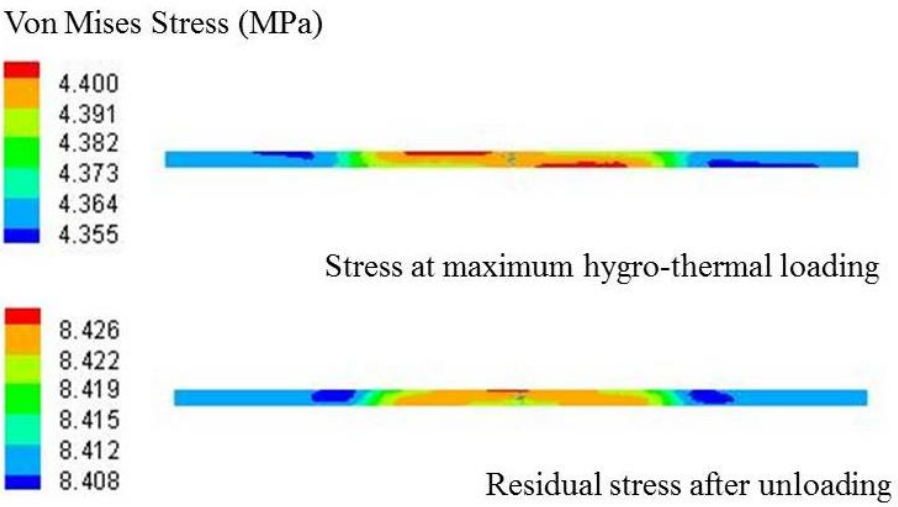

Figure 7-13 The evolution of Von Mises stress after one fuel cell duty cycle

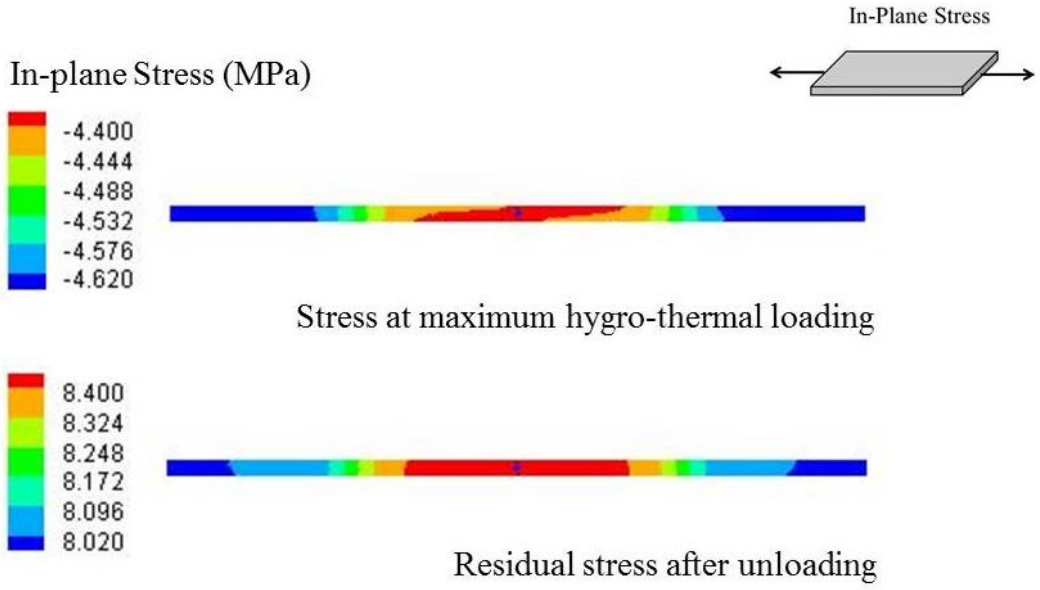

Figure 7-14 The evolution of in-plane stress after one fuel cell duty cycle

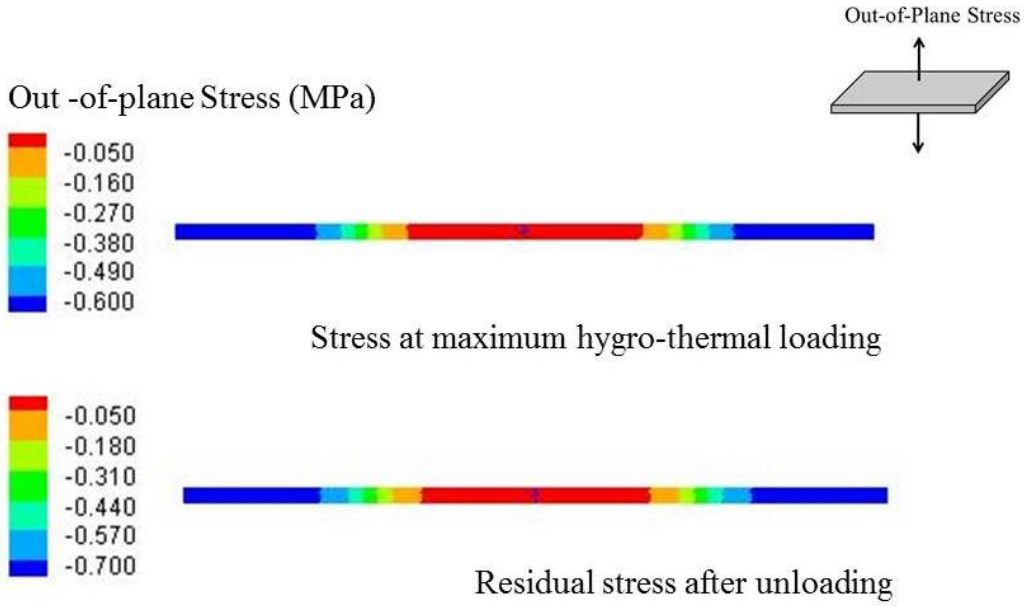

Figure 7-15 The evolution of out-of-plane stress after one fuel cell duty cycle

The study of the stress condition during start-up and shut-down processes counted on a fuel cell duty cycle simulation. The clamping force remained constant as 0.4 MPa during this duty cycle, whereas the cell temperature and relative humidity increased from 25^{o}C to 70^{o}C and 30% to 90%, respectively, during the loading process and returned to the initial condition after unloading. The evolution of the stresses throughout a fuel cell duty

cycle enabled the study of stress distributions at the maximum loading and after unloading. As presented in Figure 7-13, at the maximum load, the Nafion membrane was in overall yielding condition. Figure 7-13 also illustrates the residual Von Mises Stress. If plastic deformation did not occur during loading, the stress condition would return to the initial condition after unloading. Otherwise, the stress condition would change, which is called the residual stress. As shown in Figure 7-13, the residual Von Mises stress was larger than the stress at the maximum loading condition, meaning that the Nafion membrane experienced further yielding during the fuel cell shut-down process.

A similar phenomenon also occurred in the in-plane stress and the out-of-plane stress distributions, as presented in Figure 7-14 and Figure 7-15. The shrinkage of the Nafion membrane contributed to a redistribution of the internal forces and stresses. As a result, tensile in-plane stresses were achieved upon unloading. However, the out-of-plane stress was smaller than the in-plane stress. Because of the constant clamping stress, its change was not significant.

These results meant that both the start-up and shut-down processes contributed to the plastic deformation of a Nafion membrane. In addition, Figure 7-14 and Figure 7-15 indicates that the stress effect changed in one fuel cell duty cycle. For instance, the initial compressive in-plane stress shifted to the tensile in-plane stress after unloading, which could intensify the microstructure changes. For example, cyclic compression and pull could impair the attachment between the catalyst layer and the Nafion membrane, causing delamination.

7.5. Effect of Cyclic Loading in Temperatures and Relative Humidity

A PEM fuel cell used in a vehicle has to undergo numerous start-up and shut-down processes. Hence, its stress and strain condition under cyclic loadings is worth studying. Fifty cycles of fuel cell start-up and shut-down processes were simulated. The clamping force remained at 0.4 MPa during the cycles. The cell temperature and relative humidity, on the other hand, increased from 25^{o}C to 70^{o}C and 30% to 90%, respectively, during the loading process and returned to the initial condition after unloading. Figure 7-16 provides

the equivalent plastic strain conditions of the Nafion membrane under cyclic changes of temperatures and relative humidity. The equivalent plastic strain first experienced an initial cyclic change. During the process to reach the maximum loading, the equivalent plastic strain always increased. However, during the unloading process, it decreased. After about 25 cycles, the equivalent plastic strain tended to become stable. This stability occurred because during the loading, levelled stresses disentangled the chains, making them more ordered and aligned. This outcome can be understood by looking at the idea of crystallinity. With greater alignment, crystallinity was induced in the Nafion membrane. Crystallinity, the solid part of the plastic strain, increased with the stress enhancement. However, there was a limit point. After this certain level of stress, crystallinity cannot increase any more. At this point, the Nafion membrane is more solid. In this case, when stress continued to increase, the plastic strain decreased. In the meantime, the difference in plastic strains, between the Nafion membrane under the land and the channel, decreased during these cycles.

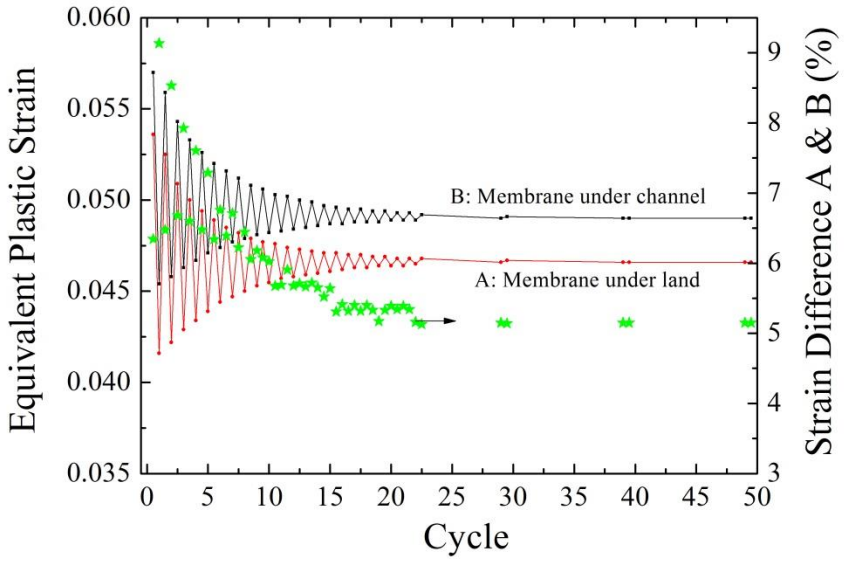

Figure 7-16 The equivalent plastic strain of the Nafion membrane with a constant clamping force under cyclic changes of temperatures and relative humidity

A corresponding phenomenon also existed in the evolutions of the Von Mises stresses. Figure 7-17 shows the Von Mises stress on the Nafion membrane when the fuel cell underwent a start-up process and worked at a temperature of 70^{o}C and a relative humidity

of 90%. The Von Mises stress continuously increased for the first 10 cycles with a decrease in the increase rate. Then, it became stable. A similar phenomenon can also be found in Figure 7-18, where the fuel cell experienced a shut-down process and return to a room condition with a temperature of 25^{o}C and a relative humidity of 30%. The residual stress after shut-down process was much larger than the stress at the maximum loading condition, thus validating the initial cyclic changes in the equivalent plastic strain.

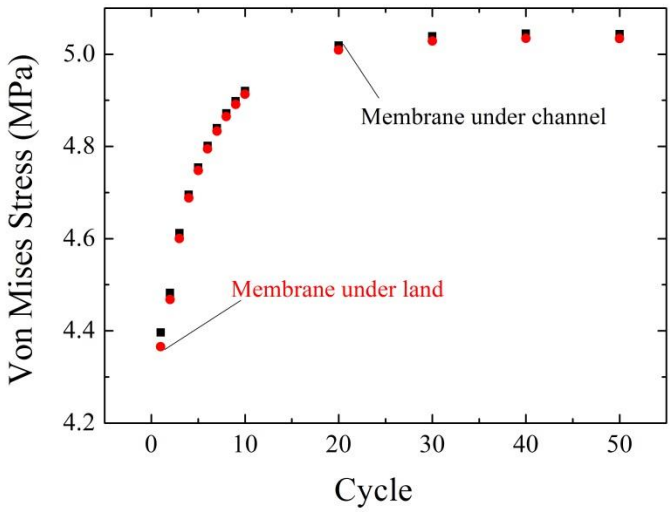

Figure 7-17 The Von Mises of the Nafion membrane with a constant clamping force of 0.4 MPa at a maximum loading under cyclic changes of temperatures and relative humidity

Figure 7-19 indicates the thinning of the Nafion membrane under the land. Such a phenomenon is related to crystallinity. A more ordered and aligned disentangled chains resulted in a more intense structure, which meant a decreased thickness. In addition, this thinning mainly occurred during the first 20 cycles. After that, the thinning of Nafion membrane under the land for each cycle becomes increasingly smaller. The Nafion membrane is used to block electrons and reactant gases. It should have a strong mechanical stability. However, the thinning could deteriorate its mechanical stability. Due to the computational limitation, the effect of only 50 cycles was studied. The reduction of Nafion membrane under the land was only about 0.6%. However, it is very likely that with the increase of cycles, the thinning might be great enough to cause structural defects, such as pineholes. In addition, the thinning of the Nafion membrane

under the land meant the bulge of the membrane under the channel became more noticeable, which can cause delamination between the catalyst layer and the membrane. Also, this difference in thickness variations between membrane under the channel and land can lead to significant structural changes, especially at the transition region of the membrane between the land and the channel.

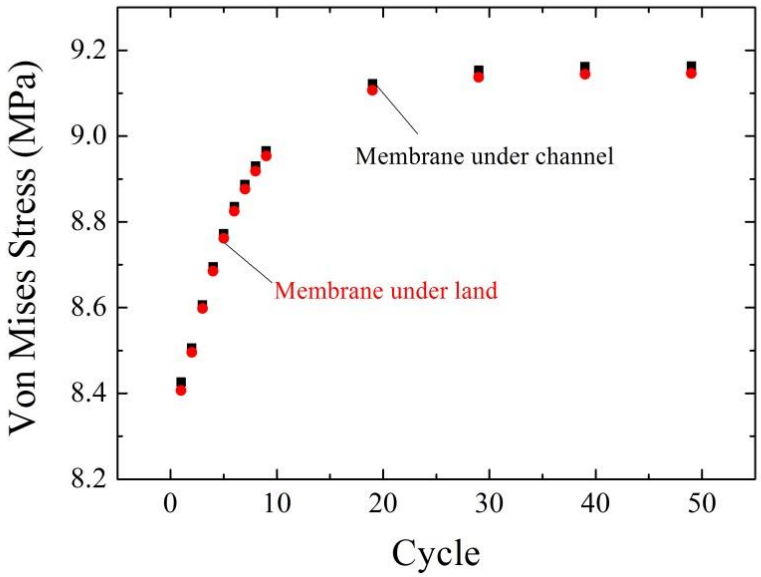

Figure 7-18 The residual Von Mises of the Nafion membrane with a constant clamping force of 0.4 MPa after unloading under cyclic changes of temperatures and relative humidity

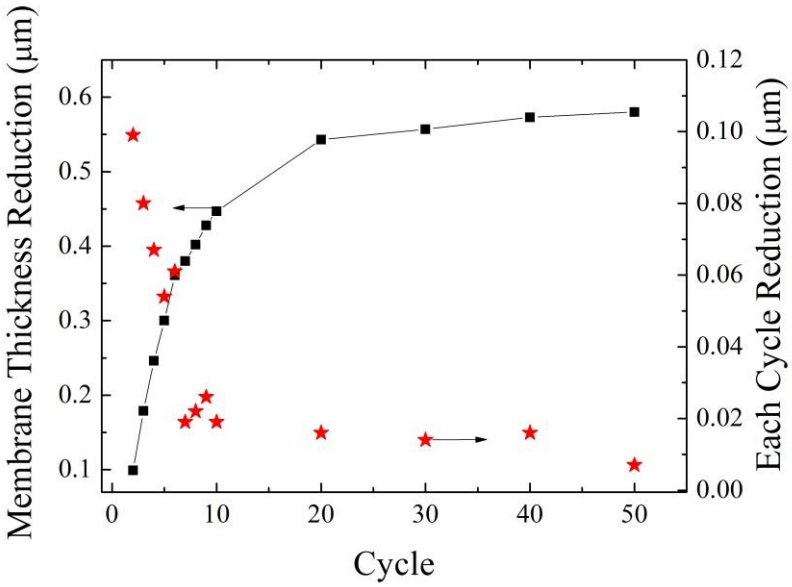

Figure 7-19 Nafion membrane thinning process

7.6. Summary

The structure model characterized the stress and deformation of an MEA during common and cyclic operating conditions. A variety of constitutive models simulated different materials in cells. In particular, a rate-dependent isotropic plasticity model with temperature- and humidity-dependent material properties modeled the viscoplasticity of the Nafion membrane. In addition, a hyperelasticity material model simulated GDLs' different loading and unloading compressive behaviours. Moreover, a traditional elastic model determined the linear mechanical behaviour of catalyst layers and graphite flow channel plates. Corresponding experiments validated the reliability of various constitutive models. The simulation results were in agreement with the experimental results.

The results verified the suspicion in the previous chapter that large stresses resulted in the microstructure defects in an MEA. For example, a large clamping force made the Nafion membrane under the channel undergo plastic deformations, although it enabled an improvement in electron conductivity. Consequently, under a common cell temperature and relative humidity, it is not recommended to apply large clamping forces. In addition, a thermal loading sequence caused a further deformation in the membrane, in spite of its assistance in upgrading the reaction rate. Similarly, a significant increase in Von Mises stress in the Nafion membrane was attributed with the growth of relative humidity. It was the determining factor of whether a Nafion membrane had plastic deformation. The results noted that these three operating conditions can have a number of advantages when applied at an appropriate scale. However, when they are inappropriately large, microstructure defects might occur. Therefore, their selections should consider both the cell performance and the durability.

During a regular fuel cell duty cycle, the expansion of the Nafion membrane brought a compressive in-plane stress during loading, whereas the shrinkage of the Nafion membrane resulted in a tensile in-plane stress upon unloading. In addition, the residual Von Mises stress was much larger than the stress at the maximum loading condition, giving rise to the crystallinity, and its associated thinning. This thinning was a possible reason for several structure defects.

The structure model quantified the MEA's deformations during common operations. These deformations were associated with the porosity, permeability, and intrinsic electronic conductivity of catalyst layers and GDLs. Moreover, the channel size and interfacial electronic conductivity also varied with the deformation. The following chapter concentrates on studying the effect of these deformations on cell performance.

Chapter 8

Cell Performance with Deformed MEAs

Chapter 7 presents that the structure model quantified the deformations of a single PEM fuel cell channel under various operating conditions. This deformation was associated with the transport parameters of GDLs and catalyst layers, in turn affecting cell performance. In this chapter, the structure-performance coupled model, described in Chapter 4, helped to study the impact of the early stage degradation, caused by various operating conditions, assembly methods, and flow channel designs, and the late stage degradation on cell performance. In this structure-performance coupled model, the deformed cell structure worked as the physical model for the cell performance modelling. It also determined associated transport properties in catalyst layers and GDLs.

8.1. Early Stage Degradation

8.1.1. The Effect of Clamping Force

A clamping force, one of the most significant working conditions for PEM fuel cell performance, prevents leaking and ensures reasonable electronic resistances between different components in a cell. The clamping force is also associated with the deformation of various components in an MEA, which results in the change of transport parameters, including porosity, permeability, and diffusivity. Figure 8-1 presents the porosity distribution of GDLs under different assembly forces. According to Figure 8-1, a GDL's thickness reduction contributes to the porosity decrease, affecting its associated permeability and diffusivity.

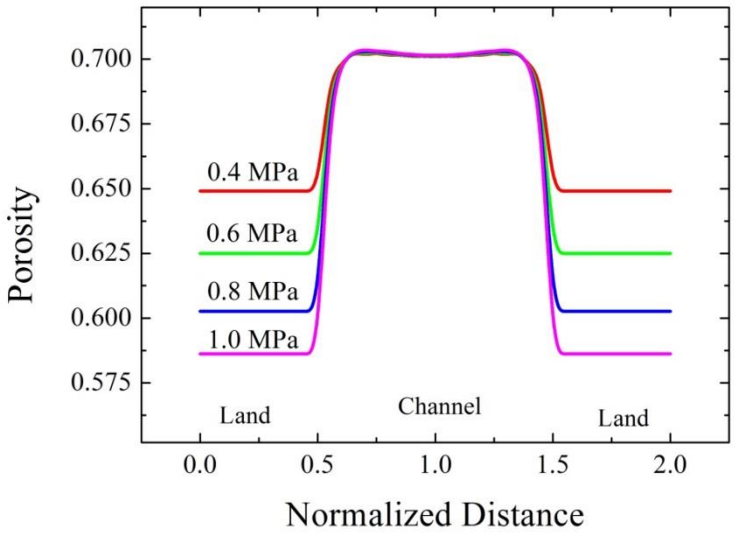

Figure 8-1 The porosity distribution of GDLs under various clamping pressures with a temperature of 75°C and a relative humidity of 100%

As shown in Figure 8-1, the porosity of GDLs under the land declined significantly, whereas the one under the flow channel had minimal changes. For example, the GDL under the land experienced a 16% reduction in porosity under a clamping force of 1.0 MPa. As a result, its overall permeability, which can be determined using Equation 4-84, could decline by as much as one or two orders of magnitude within this clamping force range. On the other hand, clamping forces have a negligible impact on the transport properties of catalyst layers. Although a catalyst layer has a porous structure, unlike the GDL which is a very compressible material, its Young's modulus is 450 MPa, indicating that under a common clamping forces range, its deformation due to clamping forces is

negligible. Therefore, its changes to transport properties are mainly related with operating conditions, such as cell temperatures and relative humidity, which will be discussed in the following sections.

Figure 8-2 illustrates the *I-V* curves of a PEM fuel cell with various clamping forces. The increase in the clamping force improved the cell performance. During the low current density range, where current density was smaller than 0.5 A/cm^2, such an improvement was not significant. However, this improvement became more appreciable when the current density was greater than 0.6 A/cm^2. As presented in Figure 8-3, the current density increased about 7% as the levelled clamping force increased from 0.4 MPa to 1.0 MPa when the cell voltage maintained at 0.7 V. This is a very interesting phenomenon because, in theory, a large clamping force brings reductions in the porosity of a GDL, which consequently should result in impaired gas transport phenomena. Nevertheless, in fact, a large clamping force not only increased the contact surface between the GDL and the gas mixture, but also improved the GDL's intrinsic and interfacial electron conductivity. As a result, it led to the performance growth.

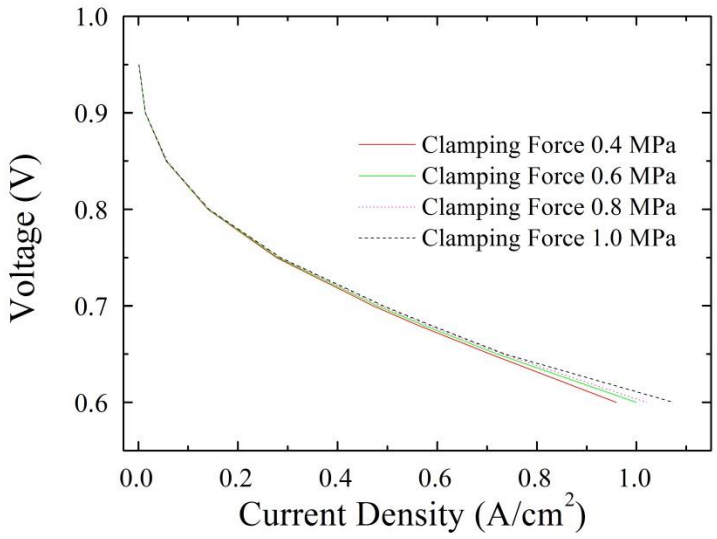

Figure 8-2 Cell performance under various clamping forces with a temperature of 75°C and a relative humidity of 100%

Figure 8-4 shows the H_2 mole fraction distribution in the anode GDL. On one hand, a large clamping force reduced the porosity of the GDL under the land. On the other hand,

under the channel, it also caused the GDL bulge, which increased the contact surface between the GDL and the gas mixture. During the cell operation, hydrogen diffused into the GDL from the GDL surface under the channel. As presented in Figure 8-4, because of this increased contact surface, levelled clamping forces improved the diffusion effect of hydrogen in the anode GDL.

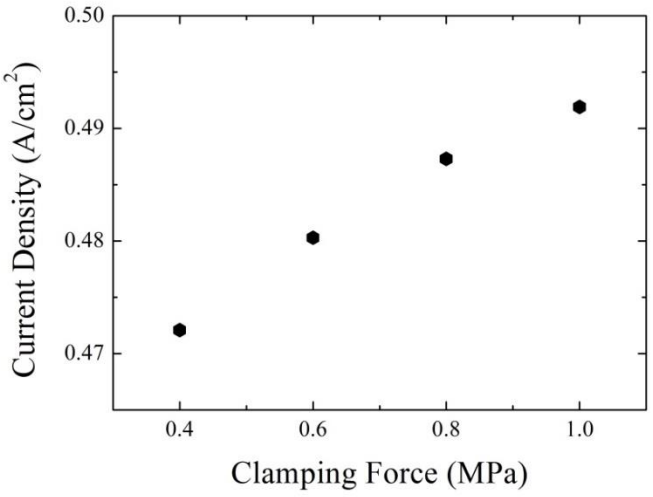

Figure 8-3 Comparison of current density for a fuel cell operating at 0.7V with different clamping forces

The gas transport phenomenon on the cathode side was different from the anode side. An oxygen reduction reaction produced water in the cathode catalyst layer, which needed to be removed from the GDL under the channel. While the water was being removed, oxygen diffused into the GDL from the channel. Because the land blocked the transportation path for the liquid water, the liquid water at this region could not be removed and was much higher than that under the channel. In addition, the enhancement of clamping forces further reduced the overall GDL porosity and intensified liquid water distribution difference, as illustrated in Figure 8-6. Because this accumulated water under the land blocked the transportation path for the oxygen, the oxygen molar fraction in the cathode GDL under the land was lower than that under the channel, as presented in Figure 8-5.

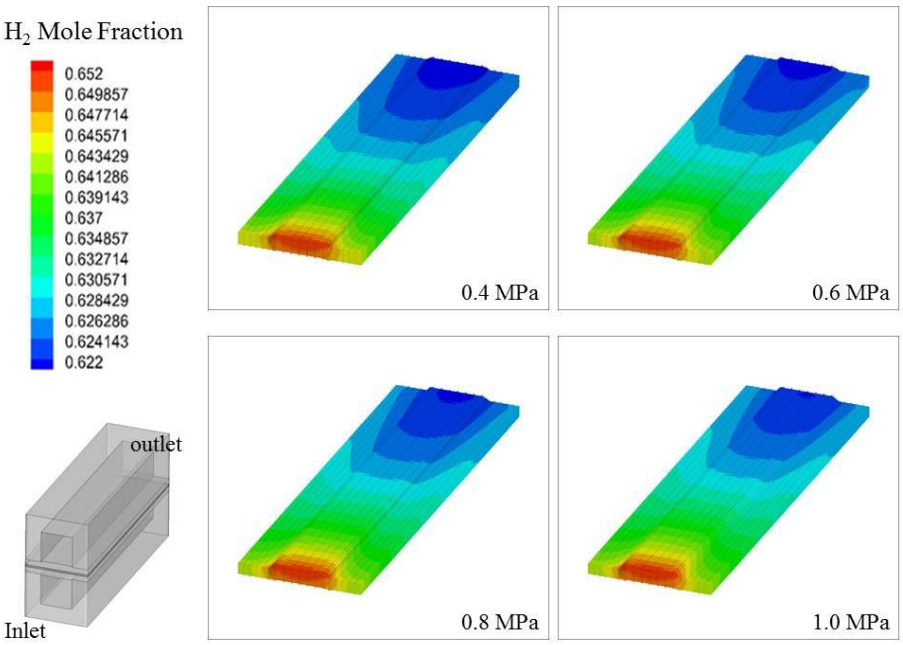

Figure 8-4 Distribution of H_2 mole fraction in the anode GDL with various clamping forces at a temperature of 75°C and a relative humidity of 100%

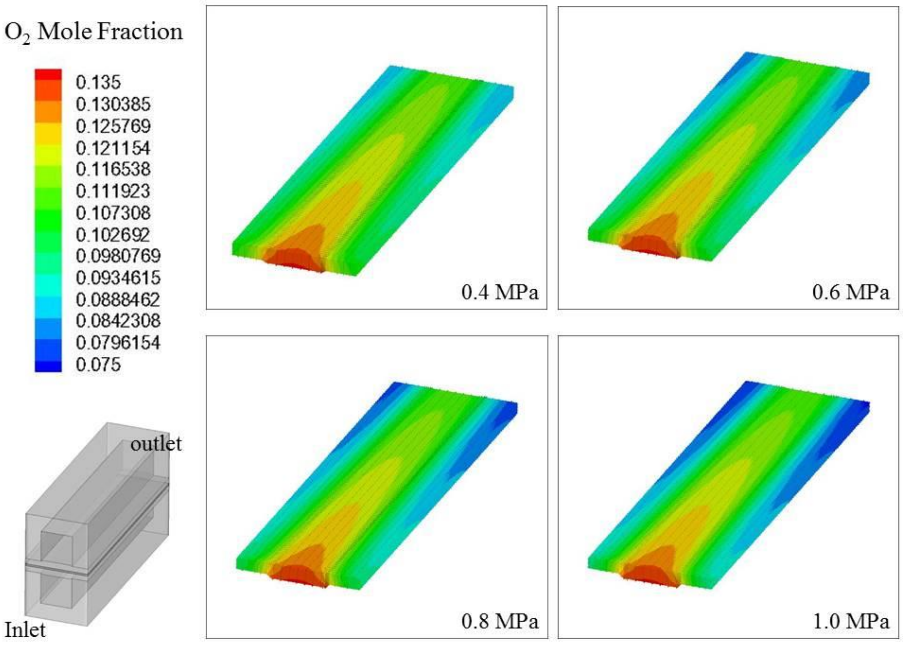

Figure 8-5 The distribution of O_2 mole fraction in the cathode GDL with various clamping forces at a temperature of 75°C and a relative humidity of 100%

Another interesting issue about the cathode side transport phenomenon is the enlarged contact surface between the gas mixture and the GDL under the channel. As shown in

Figure 8-6, bulged GDLs reduced the channel size. Since the mass flow rate was constant, the inlet gas velocity increased, which helped to remove the water out of the GDL more effectively. The combination of an increased gas velocity and contact surface helped to relieve the water management issue for the cathode GDL under the channel. This advantage became more significant when the cell was working at a high current density where water flooding was the main reason for performance decay.

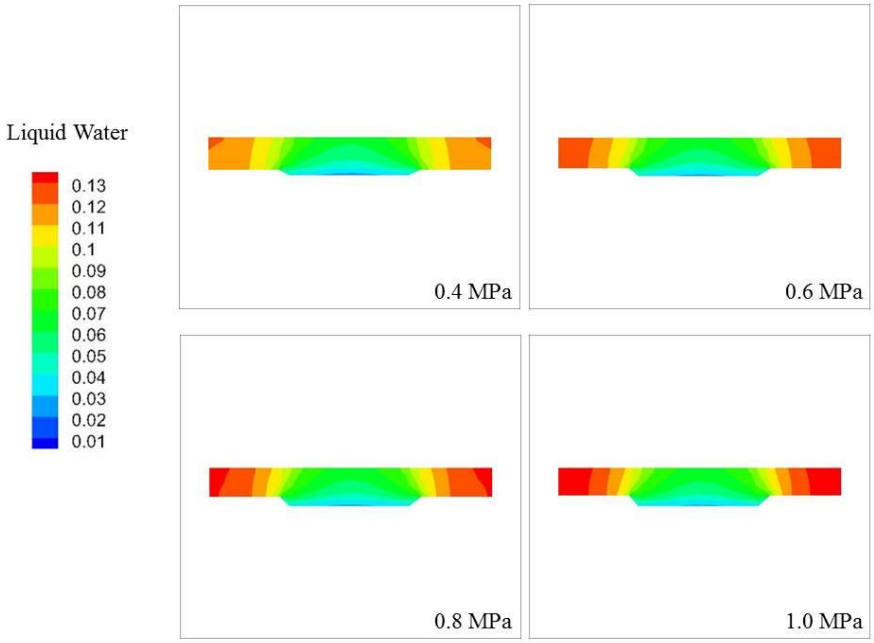

Figure 8-6 The distribution of liquid water volume fraction in the cathode GDL with various clamping forces at a temperature of 75^{o}C and a relative humidity of 100%

Electronic conductivity, another essential property affecting cell performance, includes the contact electronic conductivity between different components and the intrinsic electronic conductivity of the material itself. A GDL with a reduced porosity is also more condensed, which contributed to a reduction in the intrinsic electron resistance. According to Equation 4-70, the intrinsic electron resistance of a GDL decreases by about 17% under the clamping force of 1 MPa. Moreover, a large clamping force relieved the interfacial resistance between the channel plate and the GDL. The combination of these two reduced resistances eventually improved the cell performance.

Although a large clamping force improved cell performance, its selection should consider the associated mechanical impacts. As mentioned in Chapter 7, a large clamping force

resulted in a greater Von Mises stress in the Nafion membrane under the channel, indicating a strengthened plastic deformation of the Nafion membrane. This plastic deformation could lead to structure defects, like delamination, since catalyst layers were attached to the membrane. Therefore, there existed an ideal clamping force which could balance cell performance and durability.

8.1.2. The Effect of Cell Temperature

From the perspective of cell performance, a proper cell temperature enhances the reaction rate while ensuring a certain hydration of a Nafion membrane. On the other hand, from the perspective of MEAs' deformation, cell temperatures cause the thermal- and swelling-expansion of a Nafion membrane and a catalyst layer, which not only results in further deformation of an MEA, but also changes its related transport properties. Figure 8-7 shows the GDL porosity at different cell temperatures. The effect of cell temperatures on the GDL porosity changes was not significant. However, the catalyst layer and the Nafion membrane both tended to expand with a raised cell temperature, breaking the initial stress-strain balance in the MEA. Since the clamping force was constantly at 0.4 MPa and the anode flow channel plate was movable, the expansion of the Nafion membrane and the catalyst layer led to the movement of the anode flow channel plate as opposed to greater deformation of the GDL. Consequently, this movement helped to reach a new stress-strain balance in the MEA, which was the reason why the changes of GDLs' deformations and their corresponding porosities under various temperatures were small.

However, cell temperatures had a significant impact on the catalyst layer's porosity. A catalyst layer contains mainly ionomers and Pt/C agglomerates. The ionomers expanded noticeably with the increase in temperatures and relative humidity. This expansion reduced the porosity and the electron conductivity of catalyst layers. Here, a simplified catalyst layer modelling indicated the reduction in porosity of catalyst layers on both anode and cathode sides at various cell temperatures and a constant relative humidity of 100%.

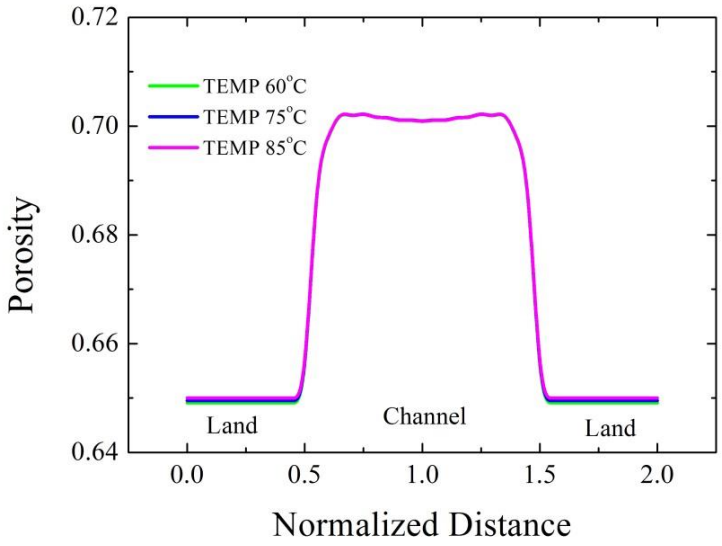

Figure 8-7 The porosity distribution of GDLs under various cell temperatures with a constant clamping force of 0.4 MPa and a relative humidity of 100%

Figure 8-8 illustrates the effect of cell temperatures on cell performance. Compared with cell temperatures of 60°C and 85°C, a PEM fuel cell had a better performance at a temperature of 75°C. In theory, a high cell temperature can increase the reaction and the gas diffusion rate. However, a high temperature also led to a reduction in the porosity of a catalyst layer and its corresponding permeability and diffusivity. Therefore, determining an optimal cell temperature is significant for the performance improvement. Figure 8-9 shows the H_2 mole fraction in the anode catalyst layer at different cell temperatures. Compared with catalyst layers at a cell temperature of 60°C or 85°C, H_2 mole fraction in the anode catalyst layer at a cell temperature of 75°C was the highest. This phenomenon was consistent with the changes in the catalyst layers' porosity and gas diffusion rate. Although the anode catalyst layer had the highest porosity at 60°C, the hydrogen diffusion rate was comparatively low. Consequently, hydrogen gas could not diffuse into the anode catalyst layer as easily as it did at 75°C. The situation became the opposite when the fuel cell worked at 85°C. Hydrogen had a high diffusion rate at 85°C; nevertheless, the porosity of the catalyst layer decreased more than that at 75°C. As a result, the catalyst layer had the lowest H_2 mole fraction at this temperature.

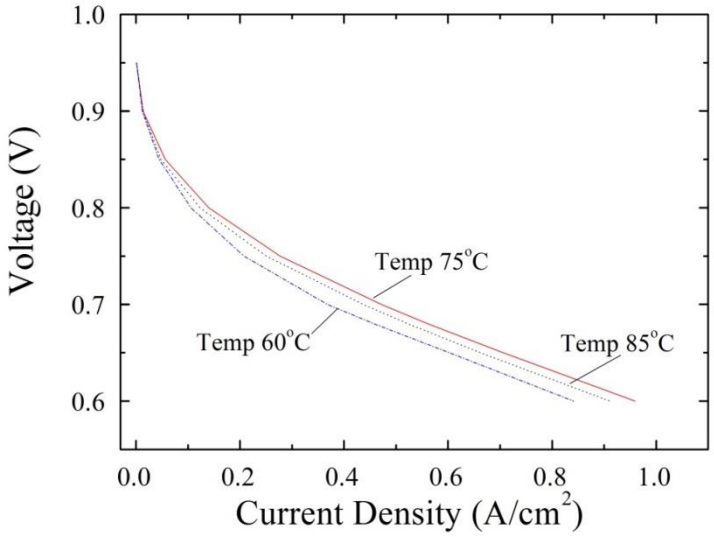

Figure 8-8 Cell performance with various cell temperatures under a clamping force of 0.4 MPa and a relative humidity of 100%

Understanding the gas transport phenomenon on the cathode side requires considerations of both the oxygen mole fraction and the liquid water in the GDL, as shown in Figure 8-10 and Figure 8-11. The reaction rate is associated with the cell temperature. Generally speaking, a high cell temperature ensures a high reaction rate. For the fuel cell working at 60^{o}C, its reaction rate was much lower than that working at 75^{o}C or 85^{o}C, indicating less water production. This low reaction rate explains why the liquid water in the GDL at 60^{o}C was the lowest among the three conditions. Meanwhile, a high cell temperature, 85^{o}C, not only increased the reaction rate, elevating the water production, but also enhanced the water evaporation. As a result, the fuel cell working at 75^{o}C had the highest liquid water in the GDL. Because water blocked the transportation path of the GDL, the oxygen mole fraction in GDLs at this temperature was the lowest.

Aside from the gas transport phenomenon, cell temperatures also affected the electron conductivity of catalyst layers in two ways. On one hand, the porosity reduction caused by levelled temperature improved the catalyst layer conductivity. On the other hand, the increased volume fraction of ionomer degraded the electron conductivity. However, at the same time the enhanced volume fraction of ionomer also improved the proton conductivity. Therefore, these trade off effects explained why merely increasing the cell

temperature is not a wise method for the performance improvement and why an optimum cell temperature exists for a better cell performance.

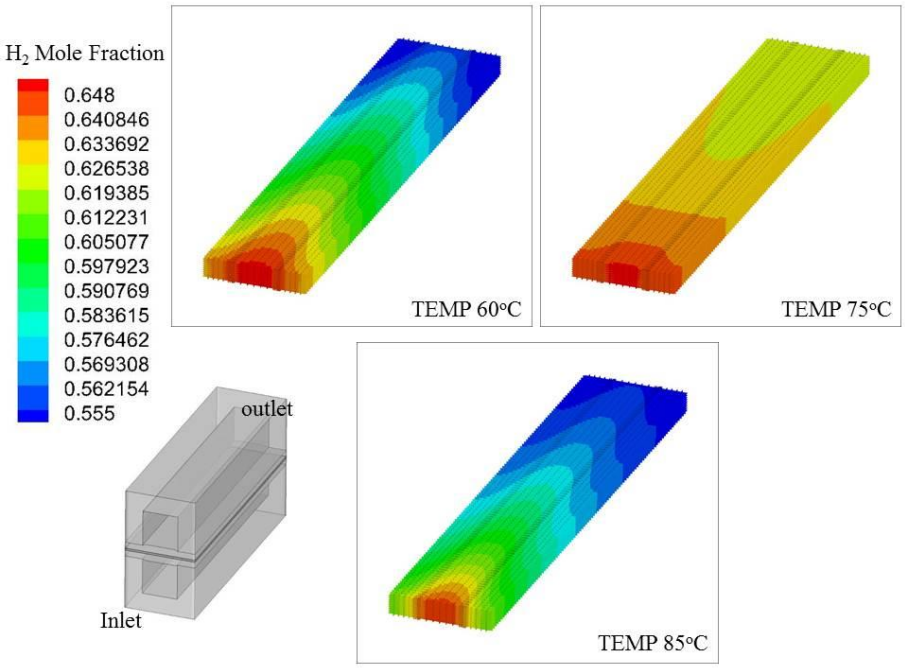

Figure 8-9 The distribution of H_2 mole fraction in the anode catalyst layer with various cell temperatures under a clamping force of 0.4 MPa and a relative humidity of 100%

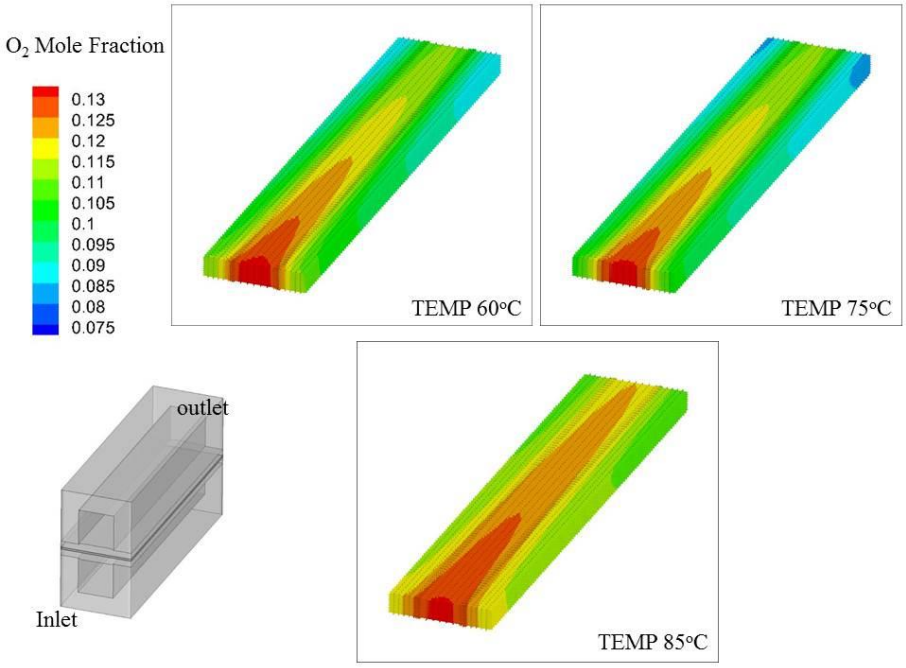

Figure 8-10 The distribution of O_2 mole fraction in the cathode catalyst layer with various cell temperatures under a clamping force of 0.4 MPa and a relative humidity of 100%

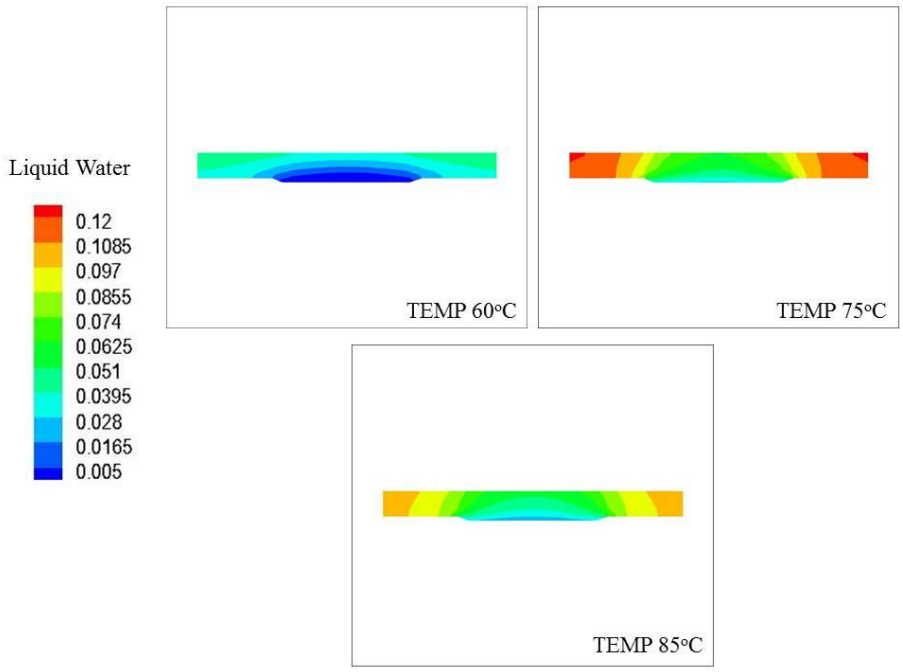

Figure 8-11 The distribution of liquid water volume fraction in the cathode GDL with various cell temperatures under a clamping force of 0.4 MPa and a relative humidity of 100%

8.1.3. The Effect of Inlet Relative Humidity

The proton conductivity of a Nafion membrane relies on its hydration level. In order to keep a certain hydration of a Nafion membrane, the most effective method is to humidify the inlet gas mixture. However, gas humidification gives rise to the swelling expansion of a Nafion membrane and a catalyst layer, which causes further deformations in an MEA and changes its transport properties. Figure 8-12 shows the GDL porosity with different inlet relative humidity. Similar to the effect of cell temperatures, the changes in inlet relative humidity did not impact the GDL porosity in a noticeable way because this modelling involved a constant-clamping-force assembly method. However, the inlet relative humidity contributed to the shifts in the porosity of catalyst layers. The ionomers experienced a significant expansion with the increase in the inlet relative humidity. Here, the corresponding modelling indicated that the catalyst layer experienced a reduction in porosity on both cathode and anode sides with varying inlet relative humidity and a constant cell temperature of 75^{o}C.

Figure 8-13 presents the impact of inlet relative humidity on the cell performance. This fuel cell showed the best performance with an inlet relative humidity of 100%. The

elevation of inlet relative humidity improved the cell performance because hydration enhancement reduced the proton resistance of a Nafion membrane. Nevertheless, such an improvement in the cell performance is not significant, compared with the improvement resulting from the cell temperature, indicating that once the Nafion membrane maintained a certain hydration, a further rise in the inlet relative humidity could not appreciably upgrade the cell performance.

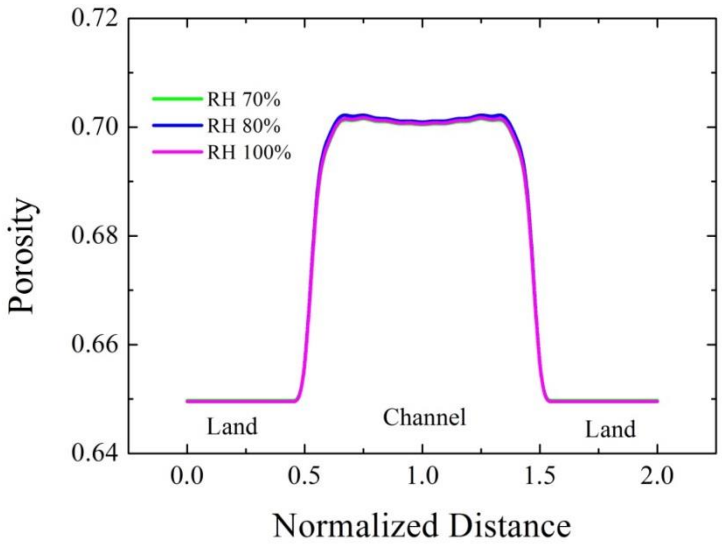

Figure 8-12 The porosity distribution of GDLs under various inlet relative humidity with a constant clamping force of 0.4 MPa and a cell temperature of 75 ^{o}C

An inlet relative humidity affects the gas transport in different components of an MEA in two different ways. A high relative humidity reduces the porosity of the catalyst layers, and lows gas mole fraction. Figure 8-14 and Figure 8-15 illustrate H_2 and O_2 mole fractions in the anode and cathode catalyst layers, respectively. Catalyst layers with a low inlet relative humidity had high H_2 and O_2 mole fractions, meaning that H_2 and O_2 can easily diffuse into catalyst layers at a low inlet relative humidity. Under this operating condition, the porosity of catalyst layers was larger than that with a high inlet relative humidity. In addition, it was more difficult to remove the produced water from a catalyst layer with a low porosity. Therefore, as presented in Figure 8-16, the cathode catalyst layer with an inlet relative humidity of 100% had the highest liquid water volume fraction.

Moreover, a low inlet relative humidity indicated high H_2 and O_2 mole fractions in the mixture gas, which was conducive to the gas diffusion.

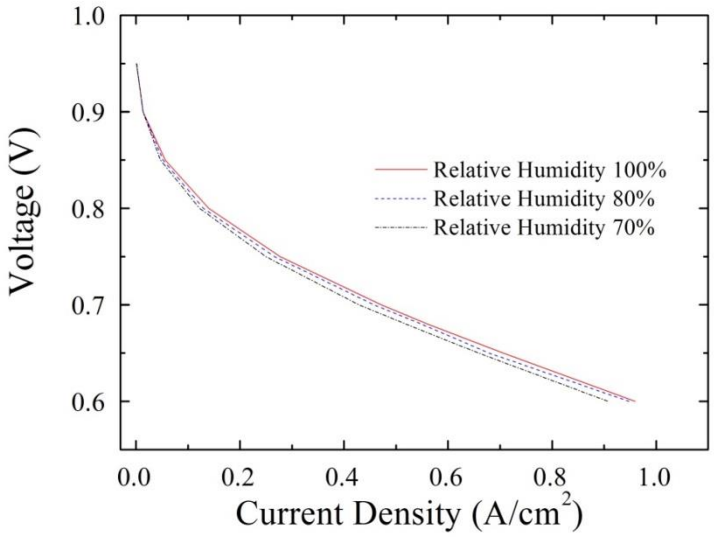

Figure 8-13 Cell performance with various cell relative humidity under a clamping force of 0.4 MPa and a cell temperature of 75 ^oC

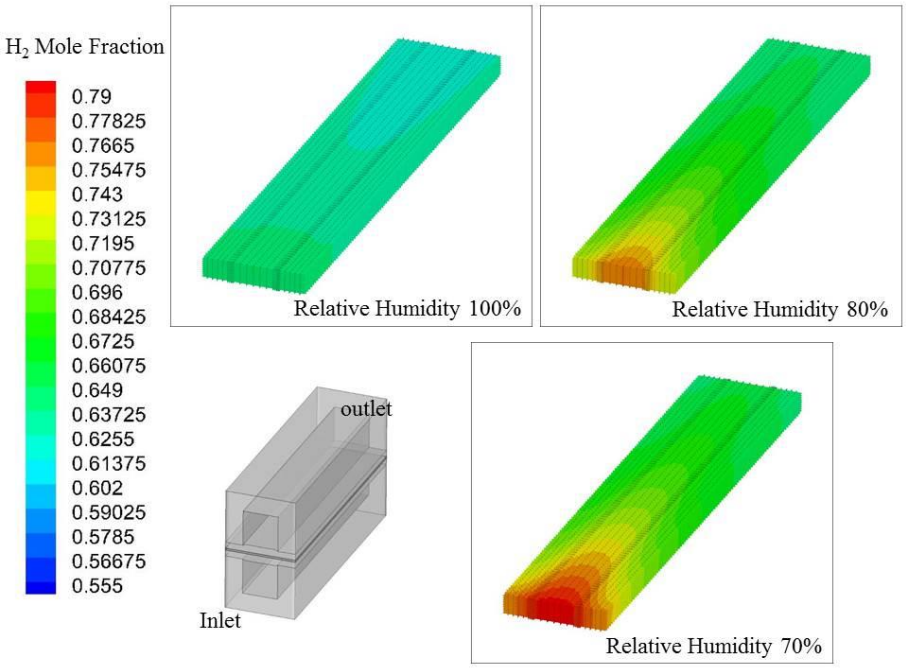

Figure 8-14 The distribution of H_2 mole fraction in the anode catalyst layer with various inlet relative humidity under a clamping force of 0.4 MPa and a cell temperature of 75 ^oC

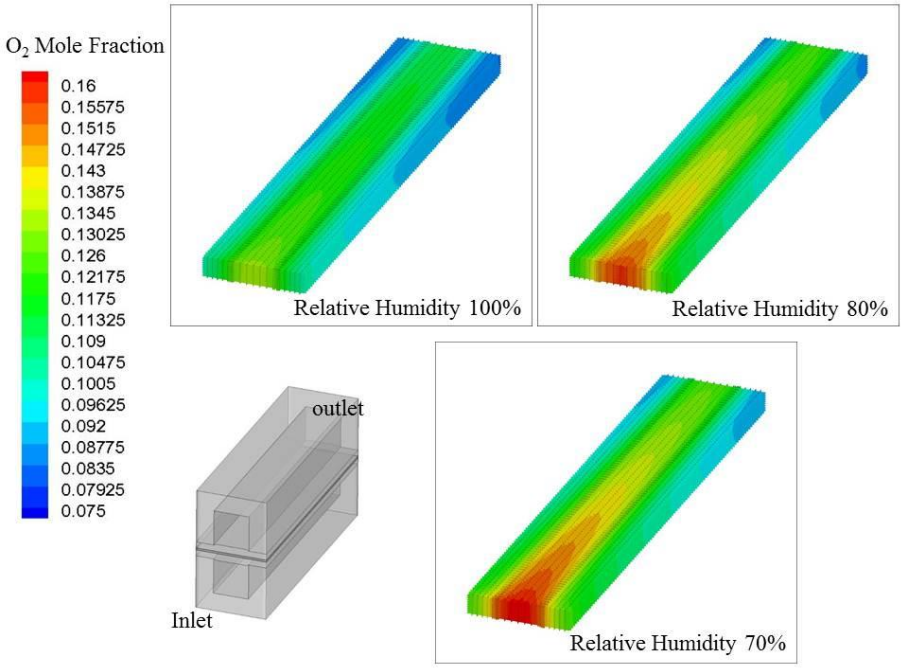

Figure 8-15 The distribution of O_2 mole fraction in the anode catalyst layer with various inlet relative humidity under a clamping force of 0.4 MPa and a cell temperature of 75 ^{o}C

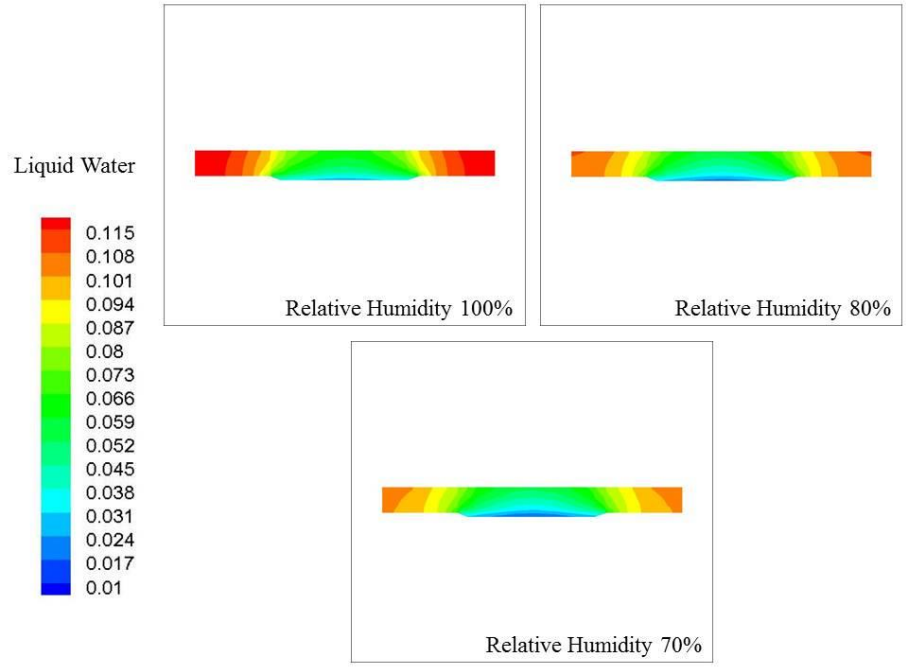

Figure 8-16 The distribution of liquid water in the anode GDL with various inlet relative humidity under a clamping force of 0.4 MPa and a cell temperature of 75 ^{o}C

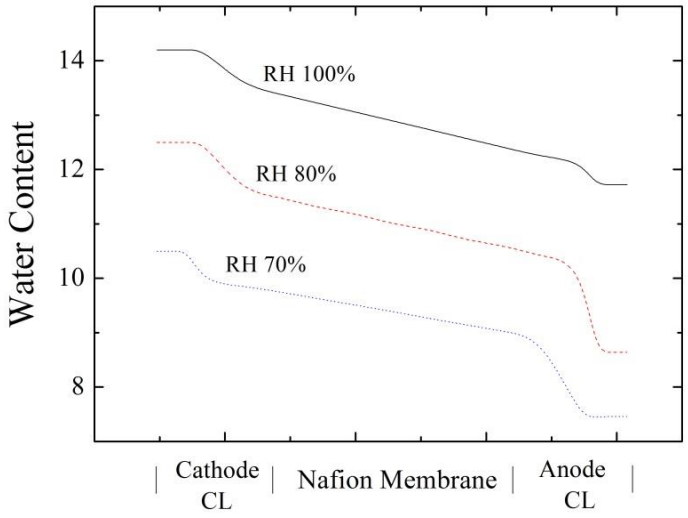

Figure 8-17 The distribution of water content in the membrane and the anode and cathode catalyst layers across the thickness direction under a clamping force of 0.4 MPa and a cell temperature of 75 ^{o}C

Although a high inlet relative humidity impeded the gas diffusion, it helped to maintain a more uniform water content distribution among the anode and cathode catalyst layers and the Nafion membrane. Figure 8-17 shows the distribution of water content in the membrane and the anode and cathode catalyst layers. The catalyst layers and the Nafion membrane working at an inlet relative humidity of 100% had the highest water content. In addition, its distribution was more uniform than that with a low inlet relative humidity. This uniform water content prevented the Nafion membrane from drying at the anode side, while it reduced the proton resistance. As a result, a high inlet relative humidity improved the cell performance.

8.1.4. The Effect of Assembly Methods

Currently, assembling a PEM fuel cell mainly involves two methods: the fixed-clamping-force assembly method and the fixed-displacement assembly method. As shown in Figure 3-8, in the fixed-clamping-force method, a pressurized bladder applies a constant clamping force on endplates. This constant force enables the assembly of a fuel cell stack. In this chapter, all the previous modelling and validation tests relied on this assembly method. On the other hand, the fixed-displacement method is a traditional assembly

method, where bolts and nuts ensure the assembly of a cell where the distance between the two endplates is fixed. During operations, this distance remains unchanged. The major difference between these two approaches is that the flow channel plate is movable in a PEM fuel cell with the fixed-clamping-force assembly method.

During operations, the expansion of a Nafion membrane and a catalyst layer led to the movement of the anode flow channel plate as opposed to greater deformation of an MEA in a cell with the fixed-clamping-force assembly method. However, with the fixed-displacement assembly method, such an expansion resulted in further deformation of an MEA, since the flow channel plates were fixed. In order to compare the effect of these two assembly approaches, we ensured that the displacement of the flow channel plates in a cell using the fixed-displacement method was the same as that in a cell with a constant clamping force of 0.4 MPa at room conditions. The results show that during operations, the overall porosity of the GDL in a fixed-displacement fuel cell was 1.6% smaller than the one in a cell with a constant clamping force.

Figure 8-18 illustrates the cell performance with various assembly approaches. A PEM fuel cell with a fixed displacement had slightly better performance than that with a constant clamping force. The mechanism behind this improvement was similar to the improvement of a cell under increased clamping forces, as shown in Figure 8-3. Because of the bolts and nuts, the thickness of the entire MEA was fixed after assembly. However, operation conditions caused the expansion of the catalyst layer and the Nafion membrane. This expansion resulted in the further thickness reduction of GDLs under the land, giving rise to an increase in the contact surface, and a decrease in the porosity, diffusivity and permeability of the GDL. In addition, this expansion improved the contact conductivity between the GDL and the graphite channel plate.

Although the fixed-displacement method initially offered a slightly better performance, the fixed-clamping-force method was the preferred selection in terms of long term durability. Figure 6-13 and Figure 6-14 indicates the thickness reduction of the GDL after several start-up and shut-down processes. Meanwhile, Figure 7-19 shows the thinning of the Nafion membrane after cyclic loadings. Consequently, it is very likely that the thickness of the MEA would decrease after a large number of shut-down and start-up

processes. This thickness reduction could create a very small space between the GDL and the flow channel plate in fixed displacement fuel cells, meaning that the contact condition between GDLs and lands would not be as good as the initial condition. Therefore, the contact resistance between the land and the GDL could increase significantly after a large number of shut-down and start-up processes in a fuel cell with the fixed-displacement assembly method. This was the major reason for the performance decay. However, a PEM fuel cell with a constant clamping force did not have this issue because the constant pressure ensures consistent contact conductivity between the GDL and the land. Furthermore, a large deformation in an MEA was associated with structure defects, such as delamination and catalyst loss. Therefore, the constant-clamping-force assembly method contributes to the improvement of cell durability.

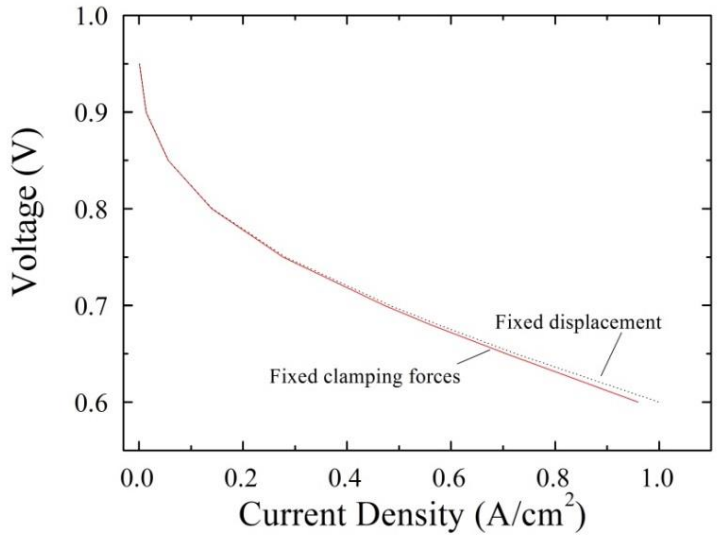

Figure 8-18 Cell performance with different assembly method at a cell temperature of 75°C and a relative humidity of 100 %

8.1.5. The Effect of Channel Designs

The design of the flow channel plate has a significant effect on the deformation of an MEA. Here, we focused on the effect of land size on the cell performance with the constant-clamping force assembly method because this part directly contacts the MEA and consequently contributes to its structure changes. The width of the land size varied from 0.8 to 1.2mm. The active area of the MEA and the clamping force were the same as

in previous modelling. Figure 8-19 shows the porosity distribution of GDLs with different land sizes. Since the clamping force on the flow channel plate was constant, the compressive stress on the GDL changed with the land size. As presented in Figure 8-19, a 0.8-mm land width contributed to the smallest porosity of a GDL under the land. However, a small land size meant that most parts of the GDL were under the channel; therefore, a GDL's overall porosity did not have a significant reduction. Here, the largest difference in overall porosity among GDLs under 0.8-mm, 1.0-mm and 1.2-mm channel lands was about 0.7%.

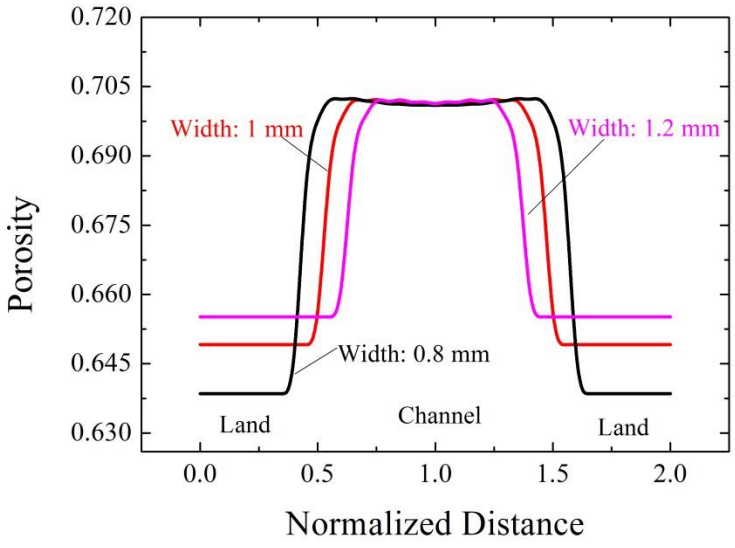

Figure 8-19 The porosity distribution of GDLs with various channel size with a constant clamping force of 0.4 MPa, a cell temperature of 75°C and a relative humidity of 100%

Figure 8-20 shows the cell performance with different channel lands. PEM fuel cells with land widths of 1.0 mm and 0.8 mm were very close, whereas the PEM fuel cell with a land width of 1.2 mm provided a better performance under large current densities. This improvement was associated with the gas transport in the MEA and the electronic conductivity. Figure 8-21 presents the hydrogen mole fraction in the anode GDL with different land widths. The GDL with a 1.2-mm-width land had the largest H_2 mole fraction, compared to GDLs with other two lands. This phenomenon is different from what we thought, because the above discussion indicated that a large contact surface was conducive to the gas diffusion to the GDL.

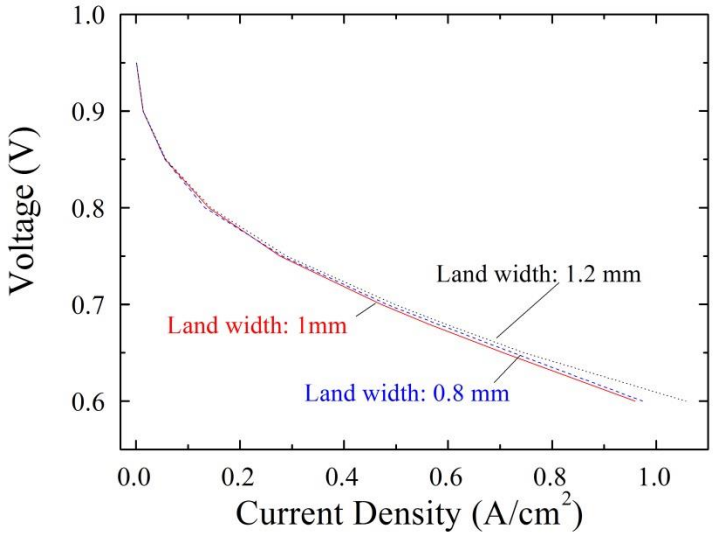

Figure 8-20 Cell performance with different channel land widths at a cell temperature of 75°C, a relative humidity of 100 % and a clamping force of 0.4 MPa

An inlet velocity was the main reason behind this phenomenon. Since the inlet flow rate was constant for each operating condition. The inlet velocity depended on the inlet area. Unlike the previous modelling, the change of inlet channel area was mainly associated with the deformation of GDLs. However, such a deformation was very small compared to the original channel size. The land width had an appreciable impact on the inlet area. When the land width changed from 0.8 mm to 1.2 mm, the inlet areas experienced a 50 % reduction, which significantly increased the inlet velocity. Figure 8-22 illustrates the H_2 mole fraction in the anode channel with different land sizes. The anode channel with a 1.2 mm-width land had the highest H_2 mole fraction. As we know, the driving force for the gas diffusion is the concentration difference. The concentration of H_2 gradually decreased when flowing through the anode channel, indicating a reduction in the driving force. A high inlet velocity meant that hydrogen stayed in the channel for a short time, which ensured a relatively high H_2 concentration. This comparatively high H_2 concentration improved the H_2 diffusion in the anode GDL with a large land width, although its contact surface was small.

On the cathode side, water management was the main issue. A wider land made it more difficult to remove the water out of the GDL, because the part of GDL under the channel

was much smaller. In addition, liquid water stayed in the GDL, blocking the transport path of the O_2, as illustrated in Figure 8-23 and Figure 8-24. The GDL with a land width of 1.2 mm contained more liquid water than other GDLs, in turn contributing to its low O_2 mole fraction. In theory, the GDL with a land width of 0.8 mm should contain less liquid water, due to its enlarged contact surface of GDL under the channel. However, its low inlet velocity impaired its water removable ability. As a result, the GDL with a land width of 1.0 mm had the highest O_2 mole fraction and less liquid water.

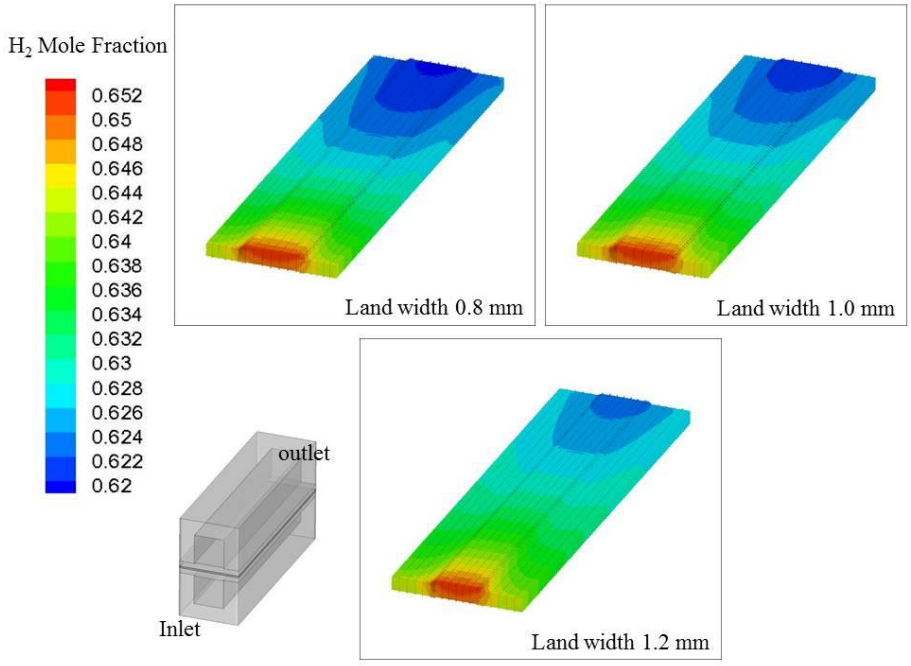

Figure 8-21 The distribution of H_2 mole fraction in the anode catalyst layer with various land widths at a cell temperature of 75°C, a relative humidity of 100 % and a clamping force of 0.4 MPa

Moreover, a land width has a significant effect on the electronic conductivity. A wider land contributes to a reduction of contact resistance between GDLs and flow channel plates, and an enhancement in the intrinsic electronic conductivity of the GDL, which was the main reason why a PEM fuel cell with a 1.2-mm-width land had a better performance. However, a wider land meant that more parts of GDLs are under compression conditions. The result in Chapter 6 showed that GDLs under cyclic loading experienced a further reduction in the thickness and greater carbon fibre breakage. These structural changes could cause a water management issue and deteriorates cell

performance. Therefore, in terms of cell durability, a 1.0 mm-width land is the preferred choice.

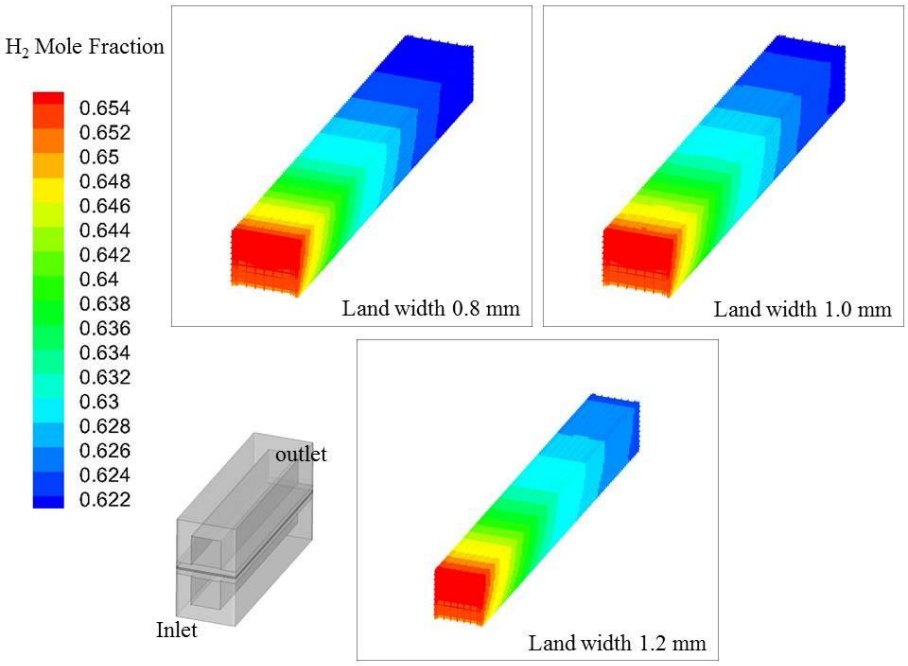

Figure 8-22 The distribution of H_2 mole fraction in the anode channel with various land widths at a cell temperature of 75°C, a relative humidity of 100 % and a clamping force of 0.4 MPa

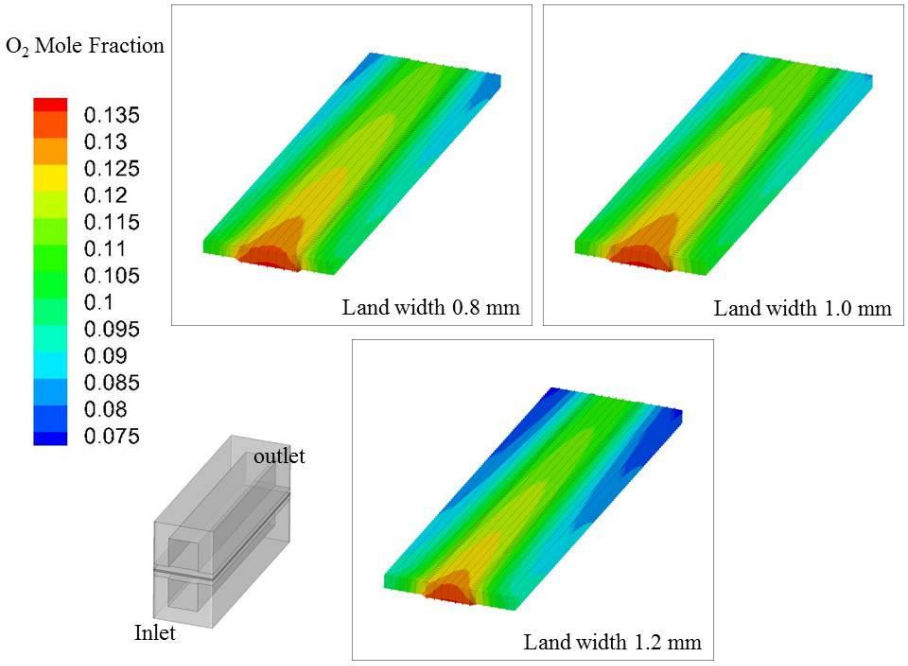

Figure 8-23 The distribution of O_2 mole fraction in the cathode catalyst layer with various land widths at a cell temperature of 75°C, a relative humidity of 100 % and a clamping force of 0.4 MPa

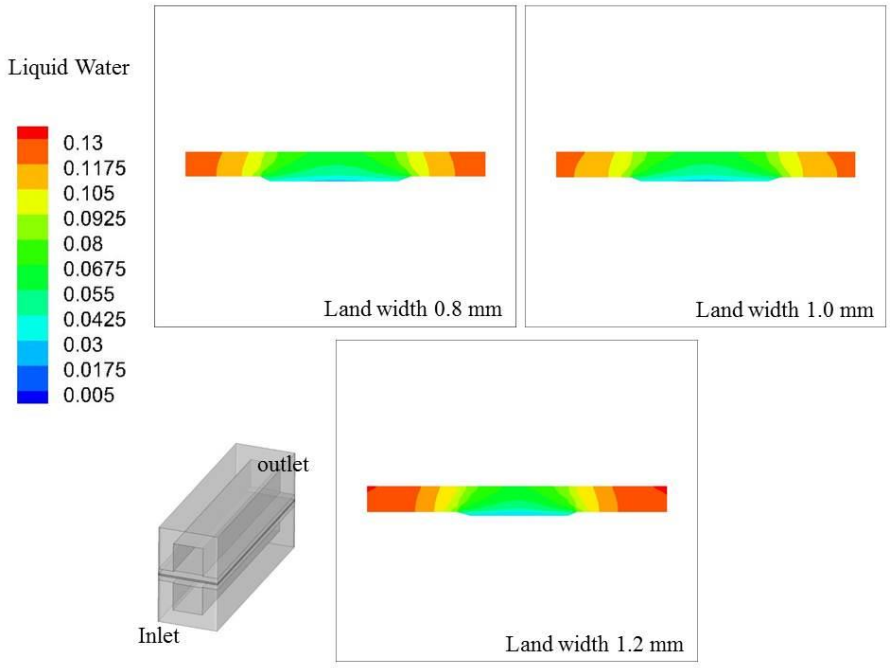

Figure 8-24 The distribution of liquid water in the cathode GDL with various land widths at a cell temperature of 75°C, a relative humidity of 100 % and a clamping force of 0.4 MPa

8.2. Late Stage Degradation

The above section studied the impact of early stage degradation on cell performance. However, as shown in Figure 6-11 and Figure 6-13, GDLs' mechanical properties degrade with cyclic changes in operating conditions. After 2000 cycles, the compressive strain decreases about 7%. This material degradation further affects the cell performance. Figure 8-25 shows the effects of mechanical degradation on cell performance. The performance decreases about 8% after 2000 cycles of start-up and shut-down processes, which results from a decrease in porosities, effective transport parameters and corresponding decay in the transport phenomenon. As mentioned in chapter 1, practical degradation targets require less than 10% loss in the efficiency of the fuel cell system at the end of application. According to the modelling result, the performance reduction has already reached about 8% by merely considering the mechanical degradation. Therefore,

in order to increase the life span of a PEM fuel cell, it is important to find an effective approach to relief the mechanical degradation. For example, a stiffer GDL can relief the reduction in the porosity, in turn, improving cell performance in the long run.

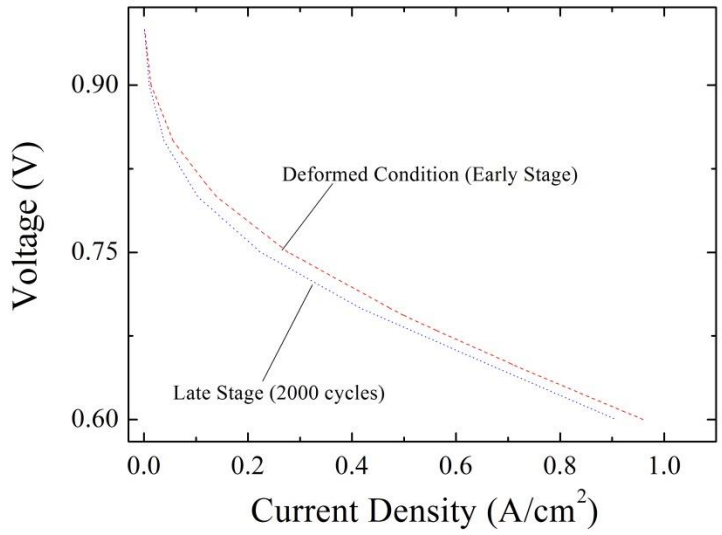

Figure 8-25 Cell performance with early and late stage of degradation at a cell temperature of 75°C, a relative humidity of 100 % and a clamping force of 0.4 MPa

8.3. Summary

A structure-performance coupled model provided a more realistic method to study cell performance under different operating conditions, assembly methods, and land structures. Unlike the modelling in previous studies, this coupled model considered the effect of deformation on the porosity, permeability, and conductivity of different components in an MEA. The results revealed that the effect of deformation on cell performance was complex.

A raised clamping force caused the deformation of GDLs and its associated increases in the conductivity, which promoted cell performance. Meanwhile, such a deformation also increased the contact surface between the gas mixture and the GDL, improving the H_2 diffusion on the anode side. However, a levelled clamping force led to the plastic

deformation in the Nafion membrane, which deteriorated its durability. Therefore, the selection of clamping forces should balance cell performance and durability.

Because cell temperature and relative humidity influenced a number of factors in the cell components, the outcomes had both negative and positive effects on cell performance. A high cell temperature intensified the reaction rate; nevertheless, it also decreased the porosity of catalyst layers, which impeded the reaction gases from transferring to the reaction site. Therefore, there existed an optimal cell temperature. A higher relative humidity ensured the hydration of the Nafion membrane and, in turn, an improvement of cell performance.

Aside from operating conditions, various assembly methods have competing effects on cell performance and durability. Compared to the constant-clamping-force assembly method, the fixed-displacement assembly method offered a slightly better cell performance. However, in terms of durability, the constant-clamping-force assembly method was an ideal selection. Under a constant clamping force, a wider channel land gave rise to the conductivity increase without significantly sacrificing the porosity, thus improving cell performance.

Under 2000 cyclic changes in operating conditions, the cell performance decreases about 8% merely with the mechanical degradation. Therefore, in order to increase the life span of a PEM fuel cell, it is important to find an effective approach to relief the mechanical degradation.

Chapter 9

Conclusions and Future Work

Mechanical degradation is of paramount importance in a proton exchange membrane fuel cell's commercialization because it is associated with not only the durability but also the cell performance. However, studies focusing on the mechanical degradation of MEAs in PEM fuel cells and its impacts on cell performance are very scarce because previous research mainly concentrated on chemical degradation. As we know, the study of mechanical degradation is a broad topic, which could be carried out from many different angles. Hence, this thesis clarified the mechanical degradation mainly through two perspectives. On one hand, it explained the effects of mechanical impact on the deformation of MEAs and its associated durability. On the other hand, it elaborated the impacts of early and late stages of mechanical degradation on cell performance.

This thesis was divided into two parts: the experimental part and the modeling part. In the experimental phase, SEM tests detailed the initial microstructures and their changes in an MEA before and after accelerated durability testing. This testing enabled a structural comparison between new and used MEAs. It also clarified the relationship between cell performance and MEAs' structure changes. The results indicated that structure defects,

such as delamination, catalyst loss, and cracks, resulted in both cell performance and durability decay. The possibility that large stresses, including clamping forces and hygro-thermal stresses, were the reason behind these structural changes, necessitated the study of stress conditions in the MEA of PEM fuel cells.

A comprehensive structure model enabled the study of stress and deformation in an MEA. The preparation of this model required knowing the mechanical properties of different cell components. These properties guided the selection of constitutive relations in the modelling. In previous studies, however, the mechanical properties of GDLs and catalyst layers varied due to different assumptions. For instance, GDLs were assumed to have the same Young's modulus as carbon fibres. A microcompression tester and the nanoindentation technique made it possible to characterize the mechanical properties of GDLs and catalyst layers. The results showed that GDLs' nonlinear compressive behaviour weakened the reliability of the previous mechanical modelling, where a GDL was assumed to have elastic properties. In addition, previous structure modelling did not include a catalyst layer due to the lack of mechanical properties. Yet, the nanoindentation test of catalyst layers revealed its elastic mechanical properties, which made it possible to consider its effects in the structure model.

In the modelling phase, a structure model characterized the stress and deformation of MEAs during common and cyclic operating conditions. This structure model overcame many standing limitations in previous models. For example, instead of using the Young's modulus of carbon fibres, a hyperelasticity material model simulated GDLs' different loading and unloading compressive behaviours. In addition, this structure model included the catalyst layers, which were ignored in all the previous modelling. Furthermore, the rate-independent plasticity model enabled a more accurate simulation of Nafion membranes.

The stress and deformation conditions validated the suspicion that inappropriately large stresses caused thickness variations and their associated structure defects in MEAs. In addition, the results showed that the selection of various operating conditions, including clamping forces, cell temperatures, relative humidity and cyclic loadings, should consider

their impacts on durability because a Nafion membrane experienced permanent deformation under operations, especially for the membrane under the channel.

The structure model indicated the degree and type of MEA deformation during common operations. This deformation changed the porosity, permeability, and intrinsic electronic conductivity of catalyst layers and GDLs. Moreover, the channel size and interfacial electronic conductivity also varied with the deformation. As a result, this deformed MEA enabled a more realistic method to study the cell performance under different operating conditions, assembly methods, and land structures. On one hand, this structure-performance coupled model involved electrochemical reaction kinetics, heat generation and transfer, transport of multi-component gas species, multi-water phases, and electrons and protons, and water phase change processes. It considered the effects of the porosity, permeability, and conductivity on cell performance. On the other hand, it also accounted for the impacts of the cell real-time activity on the cell deformations.

The primary funding revealed that the deformations of MEAs had a complex effect on the transport phenomenon. The bulge of an MEA under the channel increased the contact surface between the gas mixture and the GDL, thus improving the H_2 diffusion on the anode side. However, the thinning of an MEA under the land decreased the porosity of a GDL, thus causing water flooding on the cathode side.

As mentioned above, an MEA's deformation is associated with durability. Since operating conditions, assembly methods and land structures are associated with a number of factors in the cell component, the outcomes had both negative and positive effects on cell performance and durability. Therefore, their selections should balance both cell performance and durability.

Under 2000 cyclic changes in operating conditions, the cell performance decreases about 8% merely with the mechanical degradation. Therefore, in order to increase the life span of a PEM fuel cell, it is important to find an effective approach to relief the mechanical degradation.

The key conclusions are as follows:

- Accelerated durability testing proved that structure defects in MEAs caused cell performance decay. Consequently, reducing the occurrence of structure defects could enable a high cell performance, and, in turn, improve the durability.
- Unrecoverable microstructure changes made GDLs' compressive behaviours disobey Hook's law, which weakened the reliability of previous structure modelling, where a GDL was assumed to have elastic properties.
- Various factors impacted GDL's compressive behaviour measurements. For example, the structure modelling should account for the effects of stack size of a GDL test sample. In addition, the amount of PTFE coating and relative humidity could change the microstructure of GDLs, thereby influencing its mechanical properties. However, during a common operating compression range, such effects are not significant.
- Cyclic loadings further intensified the GDL's microstructure changes, reducing its original porosity and making it more compressible. These changes explained the performance decay in the long term. Decreased porosity and thinning process deteriorated the transport phenomenon and interfacial conductivity. Hence, a stiff GDL might improve the cell durability.
- A catalyst layer is a very stiff material. Its deformation was mainly associated with the deformation of a Nafion membrane, where it served as a coating. Consequently, decreasing the permanent deformation of the Nafion membrane might be an effective way to prevent the structure defects, such as catalyst loss.
- Cyclic compression and pull intensified the plastic deformation in the Nafion membrane, which could impair the attachment between the catalyst layer and the membrane, causing delamination and catalyst loss. Therefore, a strengthened attachment between the catalyst layer and the membrane could improve cell durability.
- A high relative humidity gave rise to a pronounced swelling expansion which was the determining factor for the membrane's permanent deformations. However, it, on the other hand, improved the cell performance. Therefore, a Nafion membrane with a low swelling expansion coefficient could improve cell durability.

- The selection of operating conditions, such as clamping forces, cell temperatures, and relative humidity, should balance both cell performance and durability. A high value of these factors contributed to a high initial cell performance; however, they also led to more structure defects and weakened durability.
- Compared with the constant-clamping-force assembly method, the fixed-displacement assembly method offered a slightly better cell performance. Nevertheless, this method also enabled a reduction in the interfacial conductivity. As a result, the constant-clamping-force assembly method, offering better durability and constant interfacial conductivity, was an ideal selection.
- Under a constant clamping force, a wider channel land gave rise to the increased conductivity without significantly sacrificing the porosity, thus promoting cell performance. Yet, for the sake of durability, a 1.0 mm width land was the preferred choice.
- Under 2000 cyclic changes in operating conditions, the cell performance decreases about 8% merely with the mechanical degradation. Therefore, in order to increase the life span of a PEM fuel cell, it is important to find an effective approach to relief the mechanical degradation.

This research also highlights some areas for future studies:

- The effect of structure defects--- Structure defects occurred during common cell operations and start-up and shut-down processes, as illustrated in Chapter 5, further impairing cell performance. However, the current structure model only considered the deformation of an MEA, without modelling these structure defects.
- The effect of industrial-size (multiple channels)--- This thesis probed the MEA's deformation with only a single PEM fuel cell channel; however, the MEA's deformation under a multi-channel flow plate may be severe and complex.
- The effect of spatial distribution of porosity--- This structure-performance coupled model only considered the overall change in porosity because of the computational resources limitations. However, it is worth studying how porosity

changes at discrete locations in a GDL, known as spatial change. These more precise measurements better reflect the real-time activity of a PEM fuel cell.

Bibliography

[1] Statistia. (2016) Vehicle Sales in China 2008-2016. [Online]. https://www.statista.com/statistics/233743/vehicle-sales-in-china/

[2] J.J Peirce, P.A Vesilind, and R Weiner, *Environmental Pollution and Control*, 4th ed. United Kingdom: Butterworth-Heinemann, 1998.

[3] K Kordesch and G.R Simader, *Fuel Cells and Their Applications*. United States: John Wiley & Sons, 1996.

[4] R.S Wilckens and L Lehnert, *Innovations in Fuel Cell Technologies*. London: United Kingdom, 2010.

[5] G Hoogers, *Fuel Cell Technology Handbook*. Boca Raton, United States: CRC Press, 2002.

[6] X Li, *Principles of Fuel Cells*. United Kingdom: Taylor & Francis, 2005.

[7] S Sieniutycz and J Jezowski, *Energy Optimization in Process Systems and Fuel Cells*. Amsterdam, Netherlands: Elsevier, 2013.

[8] S Srinivasan, *Fuel Cells: From Fundamentals to Applications*. New York, United States: Springer, 2006.

[9] B Viswanathan and M.A Scibioh, *Fuel Cells: Principles and Applications*. United Kingdom: Talyor & Francis, 2007.

[10] J Kurtz, K Wipke, and S Sprik. (2009) NREL Web site. [Online]. http://www.nrel.gov/hydrogen/pdfs/47279.pdf

[11] R Borup and R Mukundan. (2010) Fuel Cell Seminar Web Site. [Online]. http://www.fuelcellseminar.com/media/5107/lrd34-1_borup.pdf

[12] A.B LaConti, M Hamdan, and R.C McDonald, *Handbook of Fuel Cells: Fundamentals Technology and Applications*. United States: Jonh Wiley & Sons Ltd, 2003.

[13] S.J Peighambardoust, S Rowshanzamir, and M Amjadi, "Review of the Proton Exchange Membranes for Fuel Cell Applications," *International Journal of Hydrogen Energy*, vol. 35, pp. 9349-9384, 2010.

[14] F Barbir, *PEM Fuel Cells: Theory and Practice*. Cambridge, United States: Academic Press, 2012.

[15] F.A Bruijn, V.A.T Dam, and G.J.M Janssen, "Review: Durability and Degradation Issues of PEM Fuel Cell Components," *Fuel Cells*, vol. 1, pp. 3-22, 2008.

[16] S.D Knights, K.M Colbow, J St-Pierre, and D.P Wilkinson, "Aging Mechanisms and Lifetime of PEFC and DMFC," *Journal of Power Sources*, vol. 127, pp. 124-134, 2004.

[17] M.F Mathias, R Makharia, H.A Gasteiger, J.J Conley, and T.J Fuller, "Two Fuel Cell Cars in Every Garage," *The Electrochemical Society Interface*, vol. 14, pp. 24-36, 2005.

[18] National Renewable Energy Laboratory, *2008 Fuel Cell Technologies Market Report*. United States: BiblioGov, 2012.

[19] J.A Moss, "Observation of a Polymer Electrolyte Membrane Fuel Cell Degradation Under Dynamic Load Cycling," Worchester Polytechnic Institute, Bachelor Thesis 2009.

[20] J Wu et al., "A Review of PEM Fuel Cell Durability:Degradation Mechanisms and Mitigation Strategies," *Journal of Power Sources*, vol. 184, pp. 104-119, 2008.

[21] C.Z He, S Desai, G Brown, and S Bollepalli, "PEM Fuel Cell Catalysts: Cost, Performance, and Durability," *The Electrochemical Society interface*, pp. 41-44, 2005.

[22] S Kundu, M.W Fowler, L.C Simon, and S Grot, "Morhpological Features (defects) in Fuel Cell Membrane Electrode Assemblies," *Journal of Power Sources*, vol. 2, pp. 650-656, 2006.

[23] S Martemianov, M Gueguen, J.C Grandidier, and D Bograchev, "Mechanical Effects in PEM Fuel Cell: Application to Modeling of Assembly Procedure," *Journal of Applied Fluid Mechanics*, vol. 2, pp. 49-54, 2009.

[24] F.N Buchi and S Srinivasan, "Operating Proton Exchange Membrane Fuel Cells Without External Humidification of the Reactant Gases: Fundamental Aspects,"

Journal of the Electrochemical Society, vol. 144, pp. 2767-2772, 1997.

[25] R Borup et al., "PEM Fuel Cell Durability," DOE Hydrogen Program, Progress Report 2004.

[26] K Jiao, *Experimental and Modelling Studies of Cold Start Process in Proton Exchange Membrane Fuel Cell*. Canada: University of Waterloo, 2011.

[27] V.P McConnell. (2009) composite world Web Site. [Online]. http://www.compositesworld.com/articles/composites-fuel-growth-of-fuel-cell-technology

[28] V Mehta and J.S Cooper, "Review and Analysisi of PEM Fuel Cell Design and Manufacturing," *Journal of Power Sources*, vol. 114, pp. 32-53, 2003.

[29] W Yoon, "Fundamental Study of Mechanical and Chemical Degradation Mechanisms of PEM Fuel Cell Membranes," M.S. Seoul National University, PhD Thesis 2005.

[30] O Barron, "Catalyst-Coated Membranes for Polymer Electrolyte Memebrane Fuel Cells," University of Western Cape, Master Thesis 2010.

[31] H Tang, S Wang, S.P Ping, and M Pan, "A Comparative Study of CCM and Hot-pressed MEAs for PEM Fuel Cells," *Journal of Power Sources*, vol. 170, pp. 140-144, 2007.

[32] B Koraishy, J.P Meyers, and K.L Wood. Manufacturing of Membrane Electrode Assemblies for Fuel Cells. [Online]. http://www.sutd.edu.sg/cmsresource/idc/papers/2009-_Manufacturing_of_membrane_electrode_assemblies_for_fuel_cells.pdf

[33] D.P Wilkinson, J.J Zhang, R Hui, and J Fergus, *Proton Exchange Memebrane Fuel Cells: Materials Properties and Performance*. United States: CRC Press, 2009.

[34] L Dubau, L Castanhyeira, F Maillard, M Chatenet, and O Lottin, *A Review of PEM Fuel Cell Durability: Materials Degradation, Local Heterogeneities of Aging and Possibile Mitigation Strategies*. United States: John Wiley & Sons, 2014.

[35] A Collier, H.J Wang, X.Z Yuan, J.J Zhang, and D.K Wilkinson, "Degradation of Polymer Electrolyte Membranes," *International Journal of Hydrogen Energy*, vol. 31, pp. 1838-1854, 2006.

[36] W Liu, K Ruth, and G Rusch, "Membrane Durability in PEM Fuel Cells," *Journal of New Materials for Electrochemical Systems*, vol. 4, pp. 227-231, 2001.

[37] H Tang, P.K Shen, S.P Jiang, F Wang, and M Pan, "A Degradation Study of Nafion Proton Exchange Membrane of PEM Fuel Cells," *Journal of Power Sources*, vol. 170, pp. 85-92, 2007.

[38] R El-Araby, N.K Attia, G Eldiwani, S Sobhi, and T Mostafa, "Preparation of Sulfonated Monomer for PEM Fuel Cell and Solvent Optimization for Recrystallization," *World Applied Sciences Journal*, vol. 16, pp. 1082-1086, 2012.

[39] Product Information. DuPont Fuel Cells Web Site. [Online]. http://www2.dupont.com/FuelCells/en_US/assets/downloads/dfc101.pdf

[40] S.C Yin et al., "Optical-limiting and Nonlinear Optical Polyacetylenes: Synthesis of Azobenzene-containing Poly(1-alkyne)s with Different spacer and Tail Lengths," *Journal of Polymer Science Part A: Polymer Chemisitry*, vol. 44, pp. 2346-2357, 2006.

[41] J.R Yu, T Mastsuura, Y Yoshikawa, M.N Islam, and M Hori, "Lifetime Behavior of a PEM Fuel Cell with Low Humidification of Feed Stream," *Physical Chemistry Chemical Physics*, vol. 7, pp. 373-378, 2005.

[42] F.N Buchi, M Inaba, and T.J Schmidt, *Polymer Electrolyte Fuel Cell Durability*. Germany: Springer, 2009.

[43] S Escribano, J.F Blachot, J Etheve, A Morin, and R Mosdale, "Characterization of PEMFCs Gas Diffusion Layers Properties," *Journal of Power Sources*, vol. 156, pp. 8-13, 2006.

[44] L Nitta, O Himanen, and M Mikkola, "Thermal Conductivity and Contact Resistance of Compressed Gas Diffusion Layer of PEM Fuel Cell," *Fuel Cells*, vol. 2, pp. 111-119, 2008.

[45] R Yeetsorn, M.W Fowler, and C Tzoganakis. (2011) INTECH Web Site. [Online]. http://www.intechopen.com/books/nanocomposites-with-unique-properties-and-applications-in-medicine-and-industry/a-review-of-thermoplastic-composites-for-bipolar-plate-materials-in-pem-fuel-cells

[46] V Mishra, F Yang, and R Pitchumani, "Measurement and Prediction of Electrical Contact Resistance Between Gas Diffusion Layers and Bipolar Plate for Applications to PEM Fuel Cells," *Journal of Fuel Cell Science and Technology*,

vol. 1, pp. 2-8, 2004.

[47] S Park, J.W Lee, and B.N Popov, "A Review of Gas Diffusion Layer in PEM Fuel Cells: Materials and Designs," *International Journal of Hydrogen Energy* , vol. 37, pp. 5850-5865, 2012.

[48] Z.H Wang, C.Y Wang, and K.S Chen, "Two Phase Flow and Transport in the Air Cathode of Proton Exchange Membrane Fuel Cells," *Journal of Power Sources*, vol. 94, pp. 40-50, 2001.

[49] J St-Pierre and N Jia, "Successful Demonstration of Ballard PEMFCS for Space Shuttle Applications," *Journal of New Materials for Electrochemical systems*, vol. 5, pp. 263-271, 2002.

[50] M Schulze, N Wagner, T Kaz, and K.A Friedrich, "Combined Electrochemical and Surface Analysis Investigation of Degradation Processes in Polymer Electrolyte Membrane Fuel Cells," *Electrochimica Acta*, vol. 52, pp. 2328-2336, 2007.

[51] L You and H Liu, "A Two-phase Flow and Transport Model for the Cathode of PEM Fuel Cells," *International Journal of Heat and Mass Transfer*, vol. 45, pp. 2277-2287, 2002.

[52] C Lee and W Merida, "Gas Diffusion Layer Durability under Steady-state and Freezing Conditions," *Journal of Power Sources*, vol. 164, pp. 141-153, 2007.

[53] Y Wang, C.Y Wang, and K Chen, "Elucidating Differences between Carbon Paper and Carbon Cloth in Polymer electrolyte Fuel Cells," *Electrochimica Acta*, vol. 52, pp. 3965-3975, 2007.

[54] H Liu, D Xia, and J Zhang, "Platinum-based Alloy Catalysts for PEM Fuel Cells," *PEM Fuel Cell Electrocatalysts and Catalyst Layers*, pp. 631-654, 2008.

[55] A Wieckowski, *Fuel Cell Catalysis: A Surface Science Approach*. New York, United States: John Wiley & Sons, 2009.

[56] J.J Zhang, *PEM Fuel Cell Electrocatalysts and Catalyst Layers: Fundamentals and Applications*. Germany: Springer, 2008.

[57] M.M Mench, E.C Kumbur, and T.N Veziroglu, *Polymer Electrolyte Fuel Cell Degradation*. United States: Academic Press, 2011.

[58] X Cheng et al., "A Review of PEM Hydrogen Fuel Cell Contamination: Impacts,

Mechanisms and Mitigation," *Journal of Power Sources*, vol. 165, pp. 739-756, 2007.

[59] R Borup et al., "PEM Fuel Cell Catalyst Layer Structure Degradation During Carbon Corrosion," *ECS Transactions*, vol. 58, pp. 945-952, 2013.

[60] N Dandekar, "Electrochemical Characterization and Aging in PEM Fuel Cells," Worcester Polytechnic Institute, Bachelor Thesis 2012.

[61] N Parikh, "Local Degradation of Structural, Mechanical, Electrical and Chemical Properties of Membrane Electrode Assembly in Polymer Electrolyte Fuel Cell," Michigan Technological University, Master Thesis 2011.

[62] L Carrette, K.A Friedrich, and U Stimming, "Fuel Cells: Principles, Types, Fuels and Applications," *A European Journal of Chemical Physics and Physical Chemistry*, vol. 1, pp. 162-193, 2000.

[63] F N Buchi, B Gupta, O Haas, and G G Scherer, "Study of Radiation-Grafted FEP-G-polystyrene Membranes as Polymer Electrolytes in Fuel Cells," *Electrochimica Acta*, vol. 40, pp. 345-353, 1995.

[64] H Wang and G A Capuano, "Behavior of Raipore Radiation-Grafted Polymer Membranes in H 2/O 2 Fuel Cells," *Journal of the Electrochemical Society*, vol. 145, pp. 780-784, 1998.

[65] X Cheng et al., "A Review of PEM hydrogen fuel cell contamination: Impacts, mechanisms, and mitigation," *Journal of Power Source*, vol. 165, pp. 739-756, 2007.

[66] C Yang, S Srinivasan, A B Bocarsly, and S Tulyani, "A Comparison of Physical Properties and Fuel Cell Performance of Nafion and Zirconium Phosphate/Nafion Composite Membranes," *Journal of Membrane Science*, vol. 237, pp. 145-161, 2004.

[67] C Ma, L Zhang, S Mukerjee, D Ofer, and B Nair, "An Investigation of Proton Conduction in Select PEM's and Reaction Layer Interfaces-Designed for Elevated Temperature Operation," *Journal of Membrane Science*, vol. 219, pp. 123-136, 2003.

[68] J Surowiec and R Bogoczek, "Studies on the Thermal Stability of the Perfluorinated Cation-Exchange Membrane Nafion-417," *Journal of Thermal*

analysis and Calorinetry, vol. 33, pp. 1097-1102, 1988.

[69] K Broka and P Ekdunge, "Modelling the PEM Fuel Cell Cathode," *Journal of Applied Electrochemistry*, vol. 27, pp. 281-289, 1997.

[70] D.A Blom, J.R Dunlap, T.A Nolan, and L.F Allard, "Preparation of Cross-sectional Samples of PEMFC by ultramicrotomy for TEM," *Journal of the Electrochemical Society*, vol. 150, pp. 414-418, 2003.

[71] R.A Silva, T Hashimoto, G.E Thompson, and C.M Rangel, "MEA Degradation in PEM Fuel Cell: a Joint SEM and TEM Study," in *4th International Seminar Advances in Hydrogen Energy Technologies: Opportunities and Challenges in a Hydrogen Economy*, 2011.

[72] J Park, L Wang, S.G Advani, and A.K Prasad, "Durability Analysis of Nafion/Hydrophilic Pretreated PTFE Membranes for PEMFCs," *Journal of the Electrochemical Society*, vol. 159, pp. 864-870, 2012.

[73] H Tian and O Savadogo, "Silicotungstic acid Nafion Composite Membrane for Proton-exchange Membrane Fuel Cell Operation at High Temperature," *Journal of New Materials for Electrochemical Systems*, vol. 9, pp. 61-71, 2006.

[74] R Schneider, "Scanning Electron Microscopy Studies of Nafion Deformation into Silicon Microtrenches for Fuel Cell Applications," Princeton University, Bachelor Thesis 2008.

[75] H.S Park, Y.H Cho, C.R Jung, J.H Jang, and Y.E Sung, "Performance Enhancement of PEMFC through Temperature Control in Catalyst Layer Fabrication," *Electrochimica Acta*, vol. 53, pp. 763-767, 2007.

[76] J.B Russell, "Investigation of the Effect of Catalyst Layer Composition on the Performance of PEM Fuel Cells," Virginia Polytechnic Institute and State University, Master Thesis 2013.

[77] F.Y Zhang et al., "Quantitative Characterization of Catalyst Layer Degradation in PEM Fuel Cells by X-ray Photoelectron Spectroscopy," *Electrochimica Acta*, vol. 54, pp. 4025-4030, 2009.

[78] N Hodnik et al., "Severe Accelerated Degradation of PEMFC Platinum Catalyst: A Thin Film IL-SEM Study," *Electrochemistry Communications*, vol. 30, pp. 75-78, 2013.

[79] K.L More, K.S Reeves, D.L Wood, and R.L Borup, "Microstructural Evaluation of Aged PEMFC MEAs," in *107th Annual Meeting of the American Ceramic Society*, 2005.

[80] J Xian, D.L Wood III, K.L More, P Atanassov, and R.L Borup, "Microstructural Changes of Membrane Electrode Assemblies during PEFC Durability Testing at Hight Humidity Conditions," *Journal of the Electrochemical Society*, vol. 152, pp. 1011-1020, 2005.

[81] P.Y Yi, L.F Peng, X.M Lai, and L Ni, "A Numerical Model for Predicting Gas Diffusion Layer Failure in Proton Exchange Membrane Fuel Cells," *Journal of Fuel Cell Science and Technology*, vol. 8, pp. 1-10, 2011.

[82] K.K Poornesh, C.D Cho, G.B Lee, and Y.S Tak, "Gradation of Mechanical Properties in Gas Diffusion Electrode. Part 1: Influence of Naao-scale Heterogeneity in Catalyst Layer on Interfacial Strength Between Catalyst Layer and Membrane," *Journal of Power Sources*, pp. 2709-2717, 2010.

[83] V Radhakrishnan and P Haridoss, "Differences in Structure and Property of Carbon Paper and Carbon Cloth Diffusion Media and Their Impact on Proton Exchange Membrane Fuel Cell Flow Field Design," *Materials and Design*, vol. 32, pp. 861-868, 2011.

[84] I Nitta, T Hottinen, O Himanen, and M Mikkola, "Inhomogeneous Compression of PEMFC Gas Diffusion Layer Part I. Experimental," *Journal of Power sources*, pp. 26-36, 2007.

[85] E Sadeghi, N Djilali, and M Bahrami, "Effective Thermal Conductivity and Thermal Contact Resistance of Gas Diffusion Layers in Proton Exchange Membrane Fuel Cells: Part 1 Effect of Compressive Load," *Journal of Power Sources*, vol. 196, pp. 246-254, 2011.

[86] M.S Ismail, A Hassanpour, D.B Ingham, L Ma, and M Pourkashanian, "On the Compressibility of Gas Diffusion Layers in Proton Exchange Membrane Fuel Cells," *Fuel Cells*, vol. 12, pp. 391-397, 2012.

[87] M.S Ismail, T Damjanovic, D.B Ingham, M Pourkashanian, and A westwood, "Effect of Polytetrafluoroethylene-treatment and Microporous Layer-coating on the Electrical Conductivity of Gas Diffusion Layers Used in Proton Exchange Membrane Fuel Cells," *Journal of Power Sources*, vol. 195, pp. 2700-2708, 2010.

[88] H Sadeghifar, N Djilali, and M Bahrami, "Effect of Polytetrafluoroethylene (PTFE) and Micro-porous Layer (MPL) on Thermal Conductivity of Fuel Cell Gas Diffusion Layers: Modeling and Experiments," *Journal of Power Sources*, vol. 248, pp. 632-641, 2014.

[89] T.J Mason et al., "Effect of Clamping Pressure on Ohmic Resistance and Compression of Gas Diffusion Layers for Polymer Electrolyte Fuel Cells," *Journal of Power Sources*, vol. 219, pp. 52-59, 2012.

[90] M Mathias, J Roth, J Fleming, and W Lehnert, *Handbook of Fuel Cells-Fundamentals*. New York, United States: Wiley, 2003.

[91] Y Kai, Y Kitayama, M Omiya, T Uchiyama, and M Kato, "Crack Formation in Membrane Electrode Assembly Under Static and Cyclic Loadings," *Journal of Fuel Cell Science and Technology*, vol. 10, pp. 1-6, 2013.

[92] Y.P Patil, W.L Jarrett, and K.A Mauritz, "Deterioration of Mechanical Properties: A Cause for Fuel Cell Membrane Failure," *Journal of Membrane Science*, vol. 356, pp. 7-13, 2010.

[93] Y Tang et al., "An Experimental Investigation of Humidity and Temperature Effects on the Mechanical Propeties of Perfluorosulfonic Acid Membrane," *Materials Science and Engineering*, vol. A425, pp. 297-304, 2006.

[94] X.T Wang, Y Song, and B Zhang, "Experimental Study on Clamping Pressure Distribution in PEM Fuel Cells," *Journal of Power Sources*, vol. 179, pp. 305-309, 2008.

[95] S Shahsavari, A Desouza, M Bahrami, and E Kjeang, "Thermal Analysis of Air-Cooled PEM Fuel Cells," *International Journal of Hydrogen Energy*, vol. 37, pp. 18261-18271, 2012.

[96] S.J Lee, C.D Hsu, and C.H Huang, "Analyses of the Fuel Cell Stack Assembly Pressure," *Journal of Power Sources*, vol. 145, pp. 353-361, 2005.

[97] R Montanini, G Squadrito, and G Giacoppo, "Experimental Evaluation of the Clamping Pressure Distribution in A PEM Fuel Cell Using Matrix-Based Piezoresistive Thin-film Sensors," in *XIX IMEKO World Congress*, 2009.

[98] A.R Maher and S.Al Baghdadi, "A CFD Study of Hygro-thermal Stresses Distribution in PEM Fuel Cell during Regular Cell Operation," *Renew Energy*, vol.

34, pp. 674-682, 2009.

[99] A Kusoglu, A.M Karlsson, M.H Santare, S Celghorn, and W.B Johnson, "Mechanical Response of Fuel Cell Membranes Subjected to a Hygro-thermal Cycle," *Journal of Power Sources*, vol. 161, pp. 987-996, 2006.

[100] A Kusoglu, A.M Karlsson, M.H Santare, S Cleghom, and W.B Johnson, "Mechanical Behavior of Fuel Cell Membranes under Humidity Cycles and Effect of Swelling Anisotropy on the Fatigue Stresses," *Journal of Power sources*, vol. 170, pp. 345-358, 2007.

[101] M.F Serincan and U Pasaogullari, "Mechanical Behavior of the Membrane During the PEFC operation," *Journal of Power Sources*, vol. 196, pp. 1303-1308, 2011.

[102] E Firat, P Beckhaus, and A Heinzel, "Finite Element Approach for the Analysis of the Fuel Cell Internal Stress Distribution," in *Proceedings of the COMSOL Conference*, 2011.

[103] D Bograchev, M Gueguen, J.C Grandidier, and S Martemianov, "Stress and Plastic Deformation of MEA in Fuel Cells Stresses Generated During Cell Assembly," *Journal of Power Sources*, vol. 180, pp. 393-401, 2008.

[104] A.R Maher and S Al-Baghdadi, "A CFD study of Hygro-thermal Stresses Distribution in Tubular-shaped ambient air-breathing PEM Micro Fuel Cell During Regular Cell Operation," *International Journal of Energy and Environment*, vol. 1, pp. 183-198, 2010.

[105] Y.M Volfkovich and V.S Bagotzky, "The Method of standard Porosimetry: 1 Principles and Possibilities," *Joural of Power Sources*, vol. 48, pp. 327-338, 1994.

[106] R Feng, C Huang, Z Liu, D Song, and Q Wang, "Microstructure Changes in the Catalyst Layers of PEM Fuel Cells Induced by Load Cycling Part I: Mechanical Model," *Journal of Power Sources*, vol. 175, pp. 699-711, 2008.

[107] H Wu, "Mathematical Modeling of Transient Transport Phenomena in PEM Fuel Cells," University of Waterloo, Waterloo, PhD Thesis 2009.

[108] *FLUENT 6.3 Documentation*., 2006.

[109] W He, J.S Yi, and T.V Nguyen, "Two-phase Flow Model of the Cathode of PEM Fuel Cells Using Interdigitated Flow Fields," *American Institute of Chemical engineers Journal*, vol. 46, pp. 2053-2064, 2000.

[110] Y.B Zhou, *Gas Diffusion Layer Deformation and Its Effect on the Transport Characteristics and Performance of Proton Exchange Membrane Fuel Cells*. China: TianJing University, 2013.

[111] R.B Bird, W.E Stewart, and E.N Lightfoot, *Transport Phenomena*. New York: John Wiley & Sons, 1960.

[112] K Jiao and X Li, "Three-Dimensional Multiphase Modeling of Cold Start Processes in Polymer Electrolyte Membrane Fuel Cell," *Electrochimica Acta*, vol. 54, pp. 6876-6891, 2009.

[113] Q Ye and T.V Nguyen, "Three-Dimensional Simulation of Liquid Water Distribution in a PEMFC with Experimentally Measured Capillary Functions," *Journal of Electrochemical Society*, vol. 154, pp. 1242-1251, 2007.

[114] K.S Udell, "Heat Transfer in Porous Media Considering Phase Change and Capillarity---The Heat Pipe Effect," *International Journal of Heat Mass Transfer*, vol. 28, pp. 485-495, 1985.

[115] F.A.L Dullien, *Porous Media: Fluid Transport and Pore Structure*. United States: Academic Press, 1992.

[116] *Handbook of Chemistry and Physics 88th Editions*. United States: CRC Press, 2007.

[117] A.Z Weber and J Newman, "Modeling Transport in Polymer-Electrolyte Fuel Cells," *Chemical Reviews*, vol. 104, pp. 4679-4726, 2004.

[118] T.E Springer, T.A Zawodzinski, and S Gottesfeld, "Polymer Electrolyte Fuel Cell Model," *Journal of Electrochemical Society*, vol. 148, pp. 1324-1335, 2001.

[119] Y Zhou, G Lin, A.J Shih, and S.J Hu, "Assembly Pressure and Membrane Swelling in PEM Fuel Cells," *Journal of Power Sources*, vol. 192, pp. 544-551, 2009.

[120] M.M Tomadakis and T.J Robertson, "Viscous Permeability of Random Fiber Structures: Comparison of Electrical and Diffusional Estimates with Experimental and Analytical Results," *Journal of Composite Materials*, vol. 39, pp. 163-188, 2005.